

UNCLASSIFIED

AD NUMBER

AD902582

LIMITATION CHANGES

TO:

Approved for public release; distribution is unlimited.

FROM:

Distribution authorized to U.S. Gov't. agencies only; Test and Evaluation; MAR 1972. Other requests shall be referred to Air Force Armament Lab., Eglin AFB, FL 32542.

AUTHORITY

AFATL ltr 8 Jan 1976

THIS PAGE IS UNCLASSIFIED

THIS REPORT HAS BEEN DELIMITED
AND CLEARED FOR PUBLIC RELEASE
UNDER DOD DIRECTIVE 5200.20 AND
NO RESTRICTIONS ARE IMPOSED UPON
ITS USE AND DISCLOSURE,

DISTRIBUTION STATEMENT A

APPROVED FOR PUBLIC RELEASE;
DISTRIBUTION UNLIMITED.

✓
AFATL-TR-72-49

93 (2)

AD902582

**FUNDAMENTAL ASPECTS OF
UNCONFINED EXPLOSIONS**

DEPARTMENT OF AEROSPACE ENGINEERING
THE UNIVERSITY OF MICHIGAN

TECHNICAL REPORT AFATL-TR-72-49

MARCH 1972

DDC
RECEIVED
AUG 29 1972
C

Distribution limited to U. S. Government agencies only;
this report documents test and evaluation; distribution
limitation applied March 1972 . Other requests for
this document must be referred to the Air Force Armament
Laboratory (DLIE), Eglin Air Force Base, Florida 32542.

AIR FORCE ARMAMENT LABORATORY

AIR FORCE SYSTEMS COMMAND • UNITED STATES AIR FORCE

EGLIN AIR FORCE BASE, FLORIDA

AD No. _____
DDC FILE COPY

**Best
Available
Copy**

ACCESSION for	
NTIS	White Section <input type="checkbox"/>
DEC	Buff Section <input checked="" type="checkbox"/>
UNANNOUNCED	<input type="checkbox"/>
JUSTIFICATION	
BY	
DISTRIBUTION/AVAILABILITY CODES	
Dist.	AVAIL. and/or SPECIAL
8	

Fundamental Aspects Of Unconfined Explosions

J. A. Nicholls
R. S. Fry
D. R. Glass
M. Sichel
J. Vander Schaaf
A. J. Sternstein

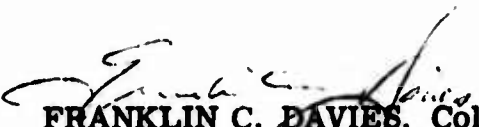
Distribution limited to U. S. Government agencies only;
this report documents test and evaluation; distribution
limitation applied March 1972 . Other requests for
this document must be referred to the Air Force Armament
Laboratory (DLIF), Eglin Air Force Base, Florida 32542.

FOREWORD

This report covers the progress made during the first year of a three-year program conducted by the Department of Aerospace Engineering, The University of Michigan, Ann Arbor, Michigan, under Contract F08635-71-C-0083 with the Air Force Armament Laboratory, Eglin Air Force Base, Florida. Major Philip J. Unrein and Lieutenant Richard E. Swanson (DLIF) served as project monitors for the Armament Laboratory. This effort was begun on 20 January 1971 and was completed on 19 January 1972.

This research was directed by Professor J. A. Nicholls. The contractor report number is UM 004880-2-T.

This technical report has been reviewed and is approved.



FRANKLIN C. DAVIES, Colonel, USAF
Chief, Flame, Incendiary, and Explosives Division

ABSTRACT

This report covers the progress made in the first year of a three-year research program. For convenience, the work is divided into two phases: Theoretical Analysis and Experimental Research.

The theoretical aspects of cylindrical strong blast waves and Chapman-Jouguet (C-J) detonations are treated in detail. Comparisons are made between the two, and a critical radius is discussed which divides the cloud into an inner blast wave zone and an outer detonation zone. Expressions for the evaluation of ground and dynamic impulse are presented. Other aspects, treated in less detail, include propagation of a C-J detonation through a cloud of fuel drops, the initiation problem, and deviations from the ideal cylindrical blast model. Also, a modified computer program for calculating detonation velocity of complex hydrocarbon fuels is discussed.

The design and operation of an experimental facility to study the propagation of two-phase detonations in a cylindrical segment of a cloud is described. The generation of strong shocks and/or detonation is achieved by explosion of a condensed explosive (Detasheet). The results of a number of experiments on the propagation of strong cylindrical shocks are presented and compared with theory. The agreement is reasonable but some questions remain. Experiments conducted with kerosene drops in air showed that at small radius the cylindrical wave decayed as a shock wave, but beyond a critical radius the wave apparently becomes a constant velocity two-phase Chapman-Jouguet detonation. Lower initiation energies show evidence of a non-sustained detonation. The experimentally determined critical radius agreed quite well with theoretical predictions. The results lend encouragement to the prediction of threshold energy levels required for detonation initiation in various geometries.

Distribution limited to U. S. Government agencies only; this report documents test and evaluation; distribution limitation applied March 1972. Other requests for this document must be referred to the Air Force Armament Laboratory (DLIF), Eglin Air Force Base, Florida 32542.

TABLE OF CONTENTS

Section	Title	Page
I.	INTRODUCTION	1
II.	THEORETICAL ANALYSIS	3
	A. Introduction	3
	B. The Cylindrical Blast Model	5
	1. Description of the Model	5
	2. Similarity Solution for a Strong Blast Wave	7
	3. The Self Similar Chapman-Jouguet Solution	13
	4. Comparison of the Blast Wave and C-J Wave Solutions	19
	C. Calculation of Ground and Dynamic Impulse	20
	1. Calculation of Total Impulse	20
	2. The Impulse at a Fixed Point	34
	3. Chapman-Jouguet Condition	38
	4. Evaluation of Ground Impulse	44
	5. Dynamic Impulse at a Fixed Point — Spherical Detonations	51
	D. Propagation of C-J Detonations Through a Cloud of Fuel Drops	58
	E. The Initiation Problem	59
	1. Blast Initiation of Gaseous Detonations	60
	2. Blast Initiation of Fuel Droplet Clouds	62
	F. Deviations from the Ideal Cylindrical Blast Model	66
	1. Nonuniform Distribution of Fuel Drops	67
	2. The Effect of Side Relief	68
	3. Propagation Beyond the Fuel Cloud Boundary	69
	4. Drop Size Distribution	69
	G. Computation of C-J Detonation Velocities for Complex Hydro-carbon Fuels	70
	H. Conclusions — Theoretical Analysis	72
III.	EXPERIMENTAL RESEARCH	73
	A. Introduction	73
	B. Experimental Facility	73
	1. Selection of Test Chamber Dimensions and Fuel Drop Size	73
	2. Method of Fuel Cloud Production	86
	3. Explosion Initiation	94
	4. Experimental Apparatus	98
	5. Experimental Procedure	107



Section	Title	Page
C.	Research Results and Discussion	110
1.	Introduction	110
2.	Blast Wave Results	112
3.	Detonation Test Results	121
IV.	FUTURE PLANS	134
A.	Theoretical Considerations	134
1.	C-J Waves with Cylindrical and Spherical Symmetry	134
2.	The Influence of Droplets on Propagation	134
3.	Idealized FAE Calculations	134
4.	Ground and Dynamic Impulse	134
5.	The Effect of Side Relief	135
6.	Initiation	135
7.	Nonuniform Droplet Distribution	135
B.	Experimental Research	135
	REFERENCES	137

LIST OF FIGURES

Figure	Title	Page
1.	Idealized FAE Model	6
2.	Behavior of Solution to Equation (22) in z-V Plane	17
3.	Behavior of Solution to Equation (22) in v-r Plane	18
4.	Blast Wave Solution, Pressure Versus Distance	21
5.	Blast Wave Solution, Velocity Versus Distance	22
6.	Blast Wave Solution, Temperature Versus Distance	23
7.	Chapman-Jouguet Detonation Solution, Pressure Versus Distance	24
8.	Chapman-Jouguet Detonation Solution, Velocity Versus Distance	25
9.	Chapman-Jouguet Detonation Solution, Temperature Versus Distance	26
10.	Fuel Air Explosions, Geometric Considerations	29
11.	Behavior of an Object in the Wake of Blast or Detonation Wave	31
12.	Universal Impulse Function	47
13.	Variation of Impulse per Unit Area with Time	50
14.	Variation of u/u_{CJ} with λ	53
15.	Variation of p/p_{CJ} with λ	54
16.	Universal Impulse Function $U_g(\tau)$ Spherical Detonation	56
17.	Variation of Dynamic Impulse per Unit Area	57
18.	Initiation Process - Ideal Versus Actual	66
19.	Chapman-Jouguet Wave with Side Relief	68
20.	Shock Interaction with Fuel Cloud Boundary	70
21.	Experimental Model Relative to Cylindrical Cloud	74
22.	Reference Frame used to Establish Experiment Scale	77
23.	Velocity Deficit Plotted Versus Hydraulic Radius for Constant Drop Size	80
24.	Reference used to Express Hydraulic Radius in Terms of Chamber Geometry	81

LIST OF FIGURES (continued)

Figure	Title	Page
25.	Radial Distance Plotted Versus Drop Size for Constant Velocity Deficit	82
26.	Velocity Deficit Versus Radial Distance from Chamber Vertex for Geometry Selected	85
27.	Terminal and Minimum Velocities of Water, Kerosene and DECH Drops	88
28.	Drops Generated by One Sub-manifold with No Pressure Disturbances Present	92
29.	Drops Generated by One Sub-manifold (Figure 34) of a Completely Integrated System with Pressure Disturbances Present. (Kerosene, $f = 1580$ cps, 360 micron drops, 1/16 OD Capillary Needles).	93
30.	Test Chamber and Associated Electrical and Fuel Systems	96
31.	Schematic of Experimental Apparatus	97
32.	Inside of Test Chamber Viewed from Exit End	99
33.	Test Chamber with Fuel Sub-manifolds (top and Breech (left))	100
34.	Sub-manifold with Seven 0.008 in. ID Needles	100
35.	Pressure Transducer Assembly	105
36.	Pressure Transducer Calibration	106
37.	Pressure Switch Assembly	108
38.	Detonation Run Raster Trace	113
39.	Blast Wave Run Pressure Trace	113
40.	Blast Wave Data Plotted as r Versus t'	114
41.	Blast Wave Data Plotted as M Versus r	115
42.	Origin of FAE Model	116
43.	Blast Wave Data Plotted as $\log r$ Versus $\log t$	119
44.	Plot of r Versus t for Experimental Values and Derived Blast Wave Equation	120

LIST OF FIGURES (concluded)

Figure	Title	Page
45.	Detonation Data Plotted as r Versus t' for 2.5 gm Detasheet "C"	122
46.	Detonation Data Plotted as r Versus t' for 1.5 gm Detasheet "C"	123
47.	Detonation Data Plotted as r Versus t' for 0.5 gm Detasheet "C"	124
48.	Detonation Plotted as M Versus r	126
49.	Critical Blast Wave Radius, r_* , Plotted Versus Initiation Energy	130
50.	Comparison of Experimental Detonation and Blast Wave Data on an r Versus t' Plot	132
51.	Comparison of Experimental and Blast Wave Data on an M Versus r Plot	133

LIST OF TABLES

Table	Title	Page
I	Comparison of Experimental Drop Formation Results with Theoretical Predictions	91
II	Summary of Experimental Tests Performed	111
III	Comparison of r_{*th} and r_{*ex}	129

NOMENCLATURE

a	local acoustic speed
A_f	frontal area of a body
c	dr_g/dt , velocity of shock wave
C_D	drag coefficient of a body
C_H	heat transfer coefficient
c_p	constant pressure specific heat
d_o	drop diameter
D	drop diameter
D	detonation wave velocity
e	specific internal energy of fluid including chemical heats of formation
E	energy release
E_o	total instantaneous energy release per unit area or per unit length respectively for planer or cylindrical blast wave geometry
f	frequency
h	specific enthalpy
ΔH_f^o	standard heat of formation
I	ground impulse per unit area
\bar{I}	total impulse imparted to ground
\bar{I}	dimensionless ground impulse
I_d	dynamic impulse on an obstacle
m_l	mass of liquid fuel per unit volume
M	Mach number
M	molecular weight
n	stoichiometric fuel-air mole fraction
N	number of fuel drops per unit volume
p	pressure
P	dimensionless pressure

Q	heat release per unit mass of mixture due to chemical reaction
\bar{Q}	heat released per unit mass of mixture due to chemical reaction and change of phase
\hat{Q}	dimensionless heat release per unit mass
r	linear spatial coordinate-radius
r_o	explosion length
R	dimensionless density
R	universal gas constant
S	length of side of volume element
t	time referenced from the origin of the cylindrical model
t'	time referenced from the oscilloscope trigger
t_b	breakup time of inert drop
T	temperature
\bar{T}_b	dimensionless drop breakup time
u	fluid velocity
u_s	actual detonation velocity
u_{so}	ideal Chapman-Jouguet velocity
U	universal impulse function
v	fluid velocity
V	dimensionless fluid velocity
\bar{x}	reaction zone length
\bar{X}_b	dimensionless drop breakup distance
z	ratio of dimensionless pressure to dimensionless density
γ	ratio of specific heats
Δ	ignition delay distance
η	actual fuel/air mole fraction
η	$1/M_s^2$
λ	dimensionless independent similarity variable
λ	wavelength

ν	geometric constant equal to 1, 2 or 3 for plane, cylindrical or spherical cloud geometry
ϕ	equivalence ratio
ρ	density
σ	surface tension
σ_ν	geometric cloud factor
τ	dimensionless time

Subscripts

0	stagnation
0	reference
1	static
1	upstream of incident shock
2	downstream of incident shock
3	downstream of C-J plane
a	air
b	breakup
c	cloud
calc	calculated
C-J	Chapman-Jouguet plane
crit	critical
d	dynamic
D	detonation
e	effective
ex	experimental
h	hydraulic
ig	ignition delay
j	jet
l	liquid fuel

min	minimum
R	Rayleigh
s	shock
s	spherical detonation
term	terminal
th	theoretical
x	x-coordinate direction
y	y-coordinate direction
y	downstream of an unspecified wave
z	z-coordinate direction
*	critical

SECTION I

INTRODUCTION

The aim of this research program is to gain a better understanding of some facets of the unconfined explosion of a distributed liquid fuel-gaseous oxidizer mixture. In the general case of such a two-phase cloud, the mean drop size and fuel-oxidizer ratio are variable throughout the cloud. Under these conditions the ignition criterion and maintenance of detonative combustion are much in question. Certainly it is possible that detonation may be established and then quenched in other parts of the cloud where the drop size is too large or the mixture is too lean or rich. Another factor of importance is the finite size of the cloud and the proximity to the ground or solid walls. The unconfined boundaries allow the detonation wave to be relieved. That is, the fact that the acoustic impedance of the surrounding gaseous phase is relatively low allows the pressure behind the detonation to be reduced by lateral expansion of the gases. This relief leads to weakening, and possibly quenching, of the wave. The mean drop size will be important in this sense.

An analytical model which is capable of predicting the time-dependent characteristics of a fuel-air explosion is completely lacking. This is in marked contrast to the point explosion problem where one can calculate the pressures, temperatures, velocities, etc., for any distance from the explosion and for any instant of time. Also, one can immediately assess the influence of the density, heat of combustion, and properties of the burned gases of the explosive. A similar level of understanding is desirable for the fuel-air explosion, although the problem is appreciably more complicated. Accordingly, one phase of this research program is directed to gaining such an understanding. A discussion of the approach used and the results gained to date are described in Section II, Theoretical Analysis.

The second general area of study in this program stems from the fact that controlled experiments on the cylindrical or spherical propagation of two-phase detonations have never been conducted. The liquid fuel drop size and the distribution of drop size and fuel-air ratio throughout the cloud are of importance to fuel-air explosions, and their influence would have to be estimated in the theoretical evaluation just described. In order to be more realistic, an experimental program has been initiated on a scaled-down model of the fuel-air explosion. Further, the laboratory model can be used to ascertain initiation energy requirements for various mixtures. The results to date from these studies are described in Section III, Experimental Research.

SECTION II

THEORETICAL ANALYSIS

A. INTRODUCTION

In the establishment of a fuel-air explosion (FAE), liquid fuel in an appropriate container is dispersed into the atmosphere as a cloud of fine droplets by the detonation of a primary charge. An appropriately placed and timed secondary explosion is then used to detonate this cloud of fuel droplets.

The shape of the fuel cloud which is generated is generally quite complex and depends upon the design of the primary charge and the fuel canister. Often the cloud is doughnut-shaped with a hole in the center generated by the munition wake. Information about particle size distribution and about the distribution of particles through the cloud is limited; however, it is clear that the cloud is far from having a uniform distribution of monodisperse droplets. The secondary blast may be initiated at the center of the cloud, or several detonators located within the periphery of the cloud may be used. The detonation of the cloud may start at the center and move outward, but in the case of the doughnut-shaped clouds the detonation may also propagate in an azimuthal direction around the cloud periphery and, of course, there may be more than one center of detonation.

Generation of ground and dynamic impulse and of a high temperature environment are key objectives of the FAE. A goal of FAE research is clearly to accomplish these objectives as effectively as possible with a given amount of fuel. Hence, it is desirable to know the detailed mechanism of the dissemination process, a subject beyond the scope of the present research. Once a fuel cloud is established, it is important to know the strength of secondary blast required to detonate the fuel cloud. The manner in which the detonation then propagates through the cloud will determine the effectiveness of the FAE.

In this report the initiation and propagation of the detonation through the fuel cloud will be considered. It is unlikely that a detailed analysis of the complex FAE as described above will be possible so that a complete understanding must rely heavily on experiment. However, much can be learned from the analytical and experimental study of relatively simple models of the actual FAE, and this is the approach followed here.

As a first step, an idealized FAE with cylindrical symmetry and a uniform monodisperse droplet distribution will be considered. This model provides a starting point for the consideration of other FAE phenomena. At very short times the idealized cylindrical FAE behaves like a cylindrical blast wave, while at long times the behavior approaches that of a cylindrical Chapman-Jouguet wave. These two limiting solutions are discussed in detail.

Expressions for the ground impulse and the dynamic impulse for Chapman-Jouguet detonations and blast waves with plane, cylindrical, and spherical symmetry have been derived. By using the similarity solutions the equations for impulse assume a particularly simple form which make it relatively easy to compare the impulse due to blast waves and detonations of various geometries. Universal functions have also been obtained which can be used to compute the total impulse at a fixed distance from the center of explosion for planar and spherical C-J waves, and several sample calculations have been carried out.

As indicated above, a critical question is whether a secondary blast will initiate a detonation in the fuel cloud. By reviewing the theory of blast initiation of detonations in pre-mixed gaseous fuels, it has been possible to, at least qualitatively, establish some criteria for the blast initiation of fuel droplet clouds.

The idealized analysis forms the basis for studying important FAE phenomena which can be treated as deviations from the idealized model. One important effect, which is omitted in the idealized analysis, is

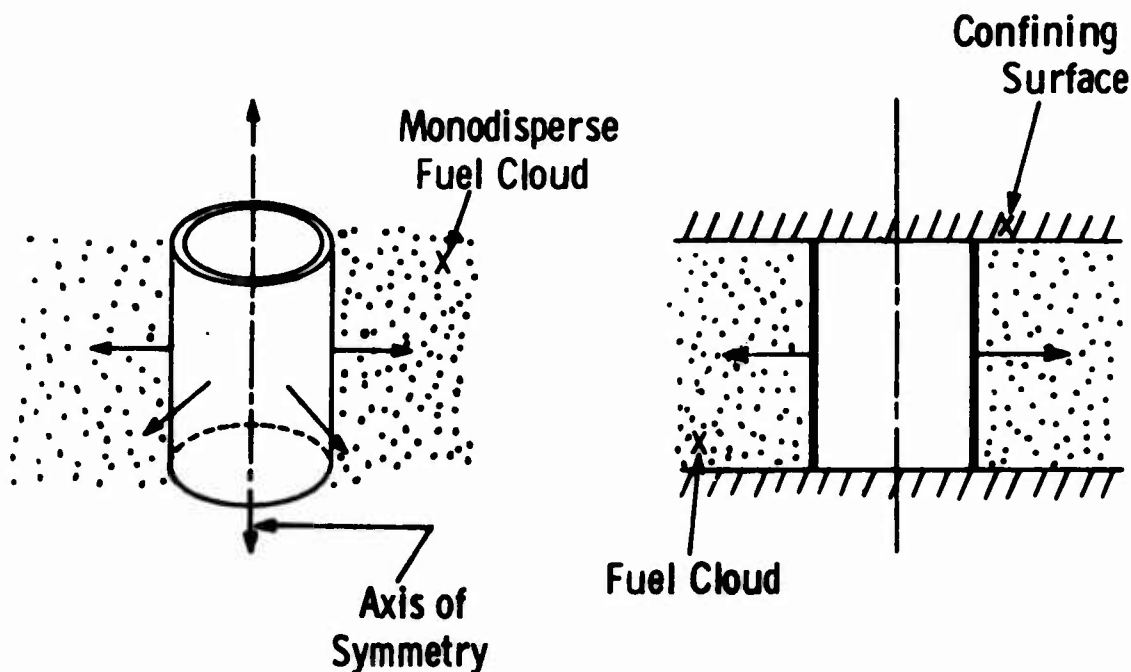
associated with the finite size of the fuel cloud. Thus, the high pressure behind the C-J detonation causes the gas behind the wave to expand into the inert region surrounding the cloud. The ground pressure therefore starts dropping to atmospheric at some finite distance behind the wave. The effect of this side relief is to reduce the impulse generated by the FAE. In this report the effects of side relief are described in the light of current work on this subject.

The droplet size distribution and the distribution of the fuel within the cloud may also have important effects on the FAE. Some modifications of the ideal model which will make it possible to examine the influence of a non-uniform distribution of fuel are considered.

B. THE CYLINDRICAL BLAST MODEL

1. Description of the Model

An idealized model consisting of a cylindrical wave propagating through a monodisperse cloud of uniformly distributed fuel droplets provides an excellent starting point for the theoretical study of the FAE process. The secondary blast is initiated by the instantaneous release of energy E_0 per unit length of the axis of the cylindrical wave. This idealized model is represented in Figure 1. The idealized model is equivalent to a cylindrical FAE confined between two non-yielding parallel surfaces (for negligible side relief) as also shown in Figure 1. A segmented test section is currently being used to simulate this idealized model of the FAE in the laboratory⁽¹⁾. The simplified model described above is amenable to both analysis and laboratory experimentation and can also form the basis for the consideration of complications introduced by the departure of the actual FAE from the ideal. The propagation of a blast wave into a detonating gas has recently been discussed by Chernyi et al⁽²⁾, Korobeinikov⁽³⁾, Bishimov et al⁽⁴⁾, and Lee et al⁽⁵⁾. From these analyses it can be concluded that at short times after the secondary explosion a strong blast wave will propagate into the fuel cloud, and at first the energy released by combustion



Cylindrical Blast Wave

Equivalent Confined Wave

Figure 1. Idealized FAE Model

will have a negligible effect upon the propagation of the wave. Provided a detonation can be initiated this blast gradually decays to a cylindrical Chapman-Jouguet (C-J) wave. It is useful to define a critical blast wave radius r_* such that the fuel energy contained within r_* is equal to the blast wave energy E_0 [Korobeinikov⁽³⁾]. Thus r_* is given by the expression

$$r_* = (\nu E_0 / \sigma_\nu Q \rho_1)^{1/\nu} \quad (1)$$

with $\nu = 1, 2$, and 3 for plane, cylindrical, and spherical geometry. The geometric factor σ_ν is given by

$$\sigma_\nu = 2(\nu - 1) \pi + (\nu - 2)(\nu - 3)$$

Q is the combustion energy released in the fuel cloud per unit mass of mixture, while ρ_1 is the initial density of the fuel cloud. Thus, when $r_g < r_*$ the idealized FAE behaves like a strong cylindrical blast wave, and with

$r_s \gg r_*$ the limiting FAE behavior approaches that of a cylindrical C-J wave, where r_s is the shock radius.

Similarity solutions of the equation of motion for the two limiting cases of fuel air explosion are available and are described in detail by Sedov.⁽⁶⁾ No simple solutions exist in the range $r \sim O(r_*)$ where a transition from blast wave to C-J wave behavior takes place. Numerical methods or semi-empirical methods similar to that proposed by Bach et al⁽⁷⁾ must be used to describe the flow in this transitional regime which is also intimately related to the initiation problem. If $r_* \ll r_c$, where r_c is the radius of the fuel cloud, the FAE will behave dominantly as a cylindrical C-J wave, and this is the regime in which practical FAE's will operate. Consequently, the blast wave and C-J similarity solutions have, as a first step, been adapted to the study of FAE behavior prior to undertaking the extensive numerical work needed to study behavior in the transitional regime.

A simple idealized model of the FAE thus consists of the blast wave solution for $r < r_*$ and the C-J solution for $r > r_*$. Although this model will not be accurate near the center of the secondary blast and in the transitional regions near $r \sim O(r_*)$, one-dimensional tests⁽⁸⁾ and some of the measurements in the segmented test section as reported below indicate that this simplified model comes remarkably close to actually describing what happens in a FAE. The strong blast wave and C-J wave similarity solutions thus play a central role in the study of FAE phenomena and hence are described in some detail below following essentially the treatment of Sedov.⁽⁶⁾

2. Similarity Solution for a Strong Blast Wave

Both the blast wave and C-J solutions are based on very general dimensional considerations. In the Eulerian approach the dependent variables of interest are the fluid velocity v , the density ρ , and the pressure p . These quantities will depend on a linear space coordinate or radius r and upon the

time t as well as other dimensional constants which enter the problem through boundary and initial conditions.

In the case of a blast wave the characteristic independent parameters are

$$\rho_1, p_1, E_0, r, t, \text{ and } \gamma$$

where ρ_1 = initial gas density

p_1 = initial gas pressure

E_0 = energy release, energy release per unit length, or energy release per unit area depending on the geometry

γ = ratio of specific heats.

From the Buckingham Pi theorem it then follows that the dimensionless velocity V , pressure P , and density R defined by

$$v = (r/t) V ; \quad \rho = \rho_1 R ; \quad p = \rho_1 (r^2/t^2) P \quad (2)$$

depend on γ and on the dimensionless ratios

$$\lambda = \pi_1 = \frac{r}{(E_0/\rho_1)^{1/\nu+2} t^{2/\nu+2}} \quad (3)$$

$$\pi_2 = \frac{p_1}{\rho_1^{1/\nu+2} E_0^{2/\nu+2} t^{-2\nu/\nu+2}} \quad (4)$$

For strong blast waves such that $p_2/p_1 \gg 1$ where p_2 is the pressure behind the shock, it is reasonable to assume that $p_1 \sim 0$ and then $\pi_2 = 0$ so that V , R , and P depend only on the single dimensionless variable λ . In this case then

$$v = (r/t) V(\lambda) ; \quad \rho = \rho_1 R(\lambda) ; \quad p = \rho_1 (r^2/t^2) P(\lambda) \quad (5)$$

so that the solution is self similar.

In the self similar blast wave the dimensionless variable λ will have a constant value on the shock and from this the conclusion follows that

$$r_s \sim t^{2/\nu+2} \quad (6)$$

i. e., r_s varies as $t^{2/3}$, $t^{1/2}$, and $t^{2/5}$ for strong planar, cylindrical, and spherical blast waves. Remarkably, this result follows from purely dimensional considerations without any recourse to the conservation equations and their solutions.

The flow behind the blast wave can only be determined once $V(\lambda)$, $R(\lambda)$, and $P(\lambda)$ are known, and the conservation equations must be solved to determine these variables. The introduction of the variable

$$z = \gamma \frac{P(\lambda)}{R(\lambda)} \quad (7)$$

in addition to V , R , and P reduces the equations for the conservation of mass, momentum, and energy to the following set of ordinary differential equations.

$$\begin{aligned} \frac{dz}{dV} = & \frac{z[2(V-1) + \nu(\gamma-1)V](V-\delta)}{[V(V-1)(V-\delta) + \nu\left(\frac{\delta}{\gamma} - V\right)z]} \\ & - \frac{z\left\{(\gamma-1)V(V-1)(V-\delta) + \left[2(V-1) + \frac{\nu\delta}{\gamma}(\gamma-1)\right]z\right\}}{(V-\delta)[V(V-1)(V-\delta) + \nu\left(\frac{\delta}{\gamma} - V\right)z]} \end{aligned} \quad (8)$$

$$\frac{d(\ln \lambda)}{dV} = \frac{z - (V-\delta)^2}{V(V-1)(V-\delta) + \nu\left(\frac{\delta}{\gamma} - V\right)z} \quad (9)$$

$$(V-\delta) \frac{d(\ln R)}{d(\ln \lambda)} = -\nu V - \frac{V(V-1)(V-\delta) + \nu\left(\frac{\delta}{\gamma} - V\right)z}{z - (V-\delta)^2} \quad (10)$$

where $\delta = 2/(\nu + 2)$. Equation (8) is a single first order equation relating z and V , and uncoupled from the other equations. The study of blast wave solutions now revolves around an analysis of Equation (8) relating z and V . Once $z(V)$ is determined R and P can be determined by quadrature or, as will be seen below, by using integral forms of the conservation equations. A study of the solution curves in the z - V plane reveals many important properties of self similar solutions of one-dimensional unsteady gas flows, and is carried out in great detail by Sedov⁽⁶⁾ and Oppenheim et al.⁽⁹⁾

The physical significance of the variable z is not always evident. Assuming that the fluid satisfies a perfect gas equation of state, it follows from the definition of $P(\lambda)$ and $R(\lambda)$ that

$$z = \gamma \frac{P}{R} = \gamma \frac{p}{\rho} \frac{t^2}{r^2} = \gamma R T \frac{t^2}{r^2} = \frac{a^2}{v^2} V^2 = \frac{V^2}{M^2} \quad (11)$$

where a is the speed of sound. Thus z may be related to the temperature or to a Mach number. For $t \neq 0$, $z \rightarrow \infty$ as $r \rightarrow 0$, i.e., z becomes infinite at the center of symmetry.

A study of the z - V plane indicates that consistent solutions of the blast wave problem do not exist without the introduction of a shock discontinuity, i.e., it is impossible to find a continuous trajectory in the z - V plane connecting the center of symmetry with the undisturbed flow at $r \rightarrow \infty$. Thus, the shock conditions in terms of z and V must be established.

The shock velocity c is readily evaluated since the shock position corresponds to a constant value of $\lambda = \lambda_*$. Hence, from the definition of λ in Equation (3), it follows that

$$r_s = \lambda_* (E_0/\rho_1)^{1/\nu+2} t^{2/\nu+2} \quad (12)$$

from which it can be shown that

$$\frac{dr_s}{dt} = c = \delta \frac{r_s}{t} = \frac{2}{\nu + 2} \frac{r_s}{t} \quad (13)$$

For a very strong shock wave propagating into a stationary fluid introduction of the variables z , P , V and R and the Equation (13) for the shock velocity into the Rankine-Hugoniot equations leads to the following result for conditions behind the shock:

$$\begin{aligned} V_2 &= \frac{4}{(\gamma + 1)(\nu + 2)} \quad ; \quad R_2 = \frac{\gamma + 1}{\gamma - 1} \\ P_2 &= \frac{8}{(\gamma + 1)(\nu + 2)^2} \quad ; \quad z_2 = \frac{8\gamma(\gamma - 1)}{(\gamma + 1)^2 (\nu + 2)^2} \end{aligned} \quad (14)$$

Ahead of the blast wave v_1 and hence $V_1 = 0$ and for the strong blast with $p_1 = 0$, it follows that $z_1 = 0$ also. Thus, the undisturbed flow corresponds to the origin of the z - V plane, while the point (z_2, V_2) immediately behind the shock is determined by Equation (14). The problem now is to determine the variation of z with V between the shock and the center of symmetry. Most treatments of blast wave theory at this stage use numerical integration of the similarity equations to determine the flow behind the blast; however, Sedov was able to obtain the following analytical expression for the function $z(V)$ by ingenious use of the integral forms of mass, momentum, and energy conservation.

$$z = \frac{(\gamma - 1) V^2 \left(V - \frac{2}{\nu + 2} \right)}{2 \left[\frac{2}{(\nu + 2)\gamma} - V \right]} \quad (15)$$

that is an explicit solution of z as a function of V is obtained and the blast wave problem is essentially solved. Using the solution (15), for $z(V)$, Equation (9) can be integrated analytically for λ as a function of V . The dimensionless density R can be determined as a function of z and V using integral forms of the conservation of mass and entropy with the result⁽⁶⁾

$$z = R^{\gamma-2} \left(V - \frac{2}{2+\nu} \right)^{-1} \lambda^{-(2+\nu)} C_2 \quad (16)$$

where C_2 is now a constant of integration whose value can be established using the shock conditions (14).

One key difficulty remains. Although dimensional considerations are sufficient to establish that $r_s \sim t^{2/(\nu+2)}$, the precise variation of shock radius $r_s(t)$ is given by

$$r_s = \lambda_* (E_0/\rho_1)^{1/\nu+2} t^{2/\nu+2} \quad (12)$$

however, the value of the constant λ_* is not known. To resolve this difficulty, Sedov⁽⁶⁾ replaced the energy release E_0 with a quantity $E \propto E_0$ but without a predetermined value. Then the choice of λ_* becomes arbitrary and for convenience the value $\lambda_* = 1.0$ is used. The relation between E and E_0 now depends on the choice of λ_* and can be obtained by noting that E_0 equals the total energy contained between the origin and shock. For a cylindrical blast, for example, equating E_0 to the total blast energy leads to the following relation between E_0 and E :

$$E_0 = \alpha(\gamma) E = \left[\pi \int_0^1 R V^2 \lambda^3 d\lambda + \frac{2\pi}{\gamma-1} \int_0^1 P \lambda^3 d\lambda \right] E \quad (17)$$

with similar relations for planar and spherical symmetry. Thus, although the similarity analysis suffices to establish how the shock radius r_s varies with time, the complete solution of the blast wave problem is needed to determine the precise variation of $r_s(t)$.

With $\lambda_* = 1$, quantities at the shock are given by the following relations:

$$\begin{aligned}
 r_s &= (E/\rho_1)^{1/\nu+2} t^{2/\nu+2} \\
 v_2 &= \frac{4}{(\nu+2)(\gamma+1)} \left(\frac{E}{\rho_1}\right)^{1/2+\nu} t^{-\nu/\nu+2} \\
 p_2 &= \frac{8\rho_1}{(\nu+2)^2(\gamma+1)} \left(\frac{E}{\rho_1}\right)^{2/2+\nu} t^{-2\nu/\nu+2} \\
 T_2 &= \frac{8(\gamma-1)}{(\nu+2)^2(\gamma+1)^2} \left(\frac{E}{\rho_1}\right)^{2/2+\nu} t^{-2\nu/\nu+2}
 \end{aligned} \tag{18}$$

The similarity variable λ now can be seen to be the ratio of the radius r to the shock radius, i.e.,

$$\lambda = r/(E/\rho_1)^{1/\nu+2} t^{2/\nu+2} = (r/r_s) \tag{19}$$

Sedov's analytical solution has been programmed for the IBM 360 computer so that all parameters of blast wave flow can be determined for different values of E_0 and for different geometries with minimal computation time. This program has been used to assess the early stages of FAE and to compare FAE and blast wave dissemination of explosive energy. To more clearly illustrate the features of blast waves, a computer-animated motion picture of the blast wave solution has been prepared.

3. The Self Similar Chapman-Jouguet Solution

As mentioned above, the C-J wave represents the limiting behavior of the idealized FAE for large times. The determination of the self similar solutions for this limiting flow following Sedov⁽⁶⁾ is outlined below.

As before, the variables of interest are v , ρ , and p , and the independent variables are again r and t ; it is also useful to introduce the dimensionless variables V , R and P defined by Equation (2). In developing the self similar solution the wave is treated as a discontinuity with heat release Q per unit mass, propagating into the unburned gas with constant speed c . The characteristic parameters of the problem are ρ_1 , p_1 , Q , r , t , and γ , and since the dimensions of Q can be expressed in terms of p_1 and ρ_1 , there are actually only 4 independent dimensional quantities in the C-J wave problem. Hence, if ρ_1 , Q and t are chosen as the primary variables, only the single dimensionless π product

$$\pi_1 = \frac{r}{\sqrt{Q} t} \quad (20)$$

can be formed from the characteristic parameters. The propagation of the C-J wave is thus self similar from the outset and, unlike the blast wave problem, no assumptions need to be made regarding the pressure p_1 in the undisturbed medium or the strength of the wave. Instead of using π_1 as the similarity variable, it is more convenient to use the variable

$$\lambda = \beta \frac{r}{\sqrt{Q} t} \quad (21)$$

where β is an arbitrary constant which is discussed below. Since λ will be constant on the detonation discontinuity in the self similar case, it is evident from Equation (21) that $r_g \sim t$, i.e., the wave will propagate with constant speed for plane, cylindrical, or spherical geometry.

Once again, it is convenient to use the variables z , V , R , and P , and then the conservation equations can be reduced to the equations

$$\frac{dz}{dV} = \frac{z [2(V-1)^2 + (\nu-1)(\gamma-1) V(V-1) - 2z]}{V [(V-1)^2 - \nu z]} \quad (22)$$

relating z and V and the equation

$$\frac{d(\ln \lambda)}{dV} = \frac{z - (V - 1)^2}{v [(V - 1)^2 - \nu z]} \quad (23)$$

The flow behind the detonation is assumed to be isentropic, and then the integral forms of mass and entropy conservation yield the relation

$$\frac{z}{R^{\gamma-1}} = \frac{C_3}{\lambda^2} \quad (24)$$

with C_3 a constant of integration. When dimensional quantities are introduced in Equation (24), this equation reduces to the statement $p/\rho^\gamma = \text{const}$, i.e., the entropy is constant in the region inside the detonation.

A continuous solution of Equation (22) extending from the center of symmetry to the undisturbed flow at $r \rightarrow \infty$ is not possible so that the jump conditions across the detonation must be introduced in order to determine the variation of z with V . The variation of λ with V can be determined from Equation (23) by quadrature once the variation of z with V is known. Unlike the blast wave problem discussed above, no analytical solution of Equation (22) for z as a function of V is known.

For propagation into a stationary gas with $V_1 = 0$, the Hugoniot conditions across the detonation, when expressed in dimensionless variables, become

$$R_2 = R_1 \left[\frac{\gamma_2}{\gamma_2 + 1} \left(1 + \frac{z_1}{\gamma_1} \right) (1 - \Lambda) \right]^{-1} \quad (25)$$

$$V_2 = 1 - \left[\frac{\gamma_2}{\gamma_2 + 1} \left(1 + \frac{z_1}{\gamma_1} \right) (1 - \Lambda) \right] \quad (26)$$

$$z_2 = \frac{\gamma_2^2}{(\gamma_2 + 1)^2} \left(1 + \frac{z_1}{\gamma_1}\right)^2 (1 - \Lambda)(1 + \gamma_2 \Lambda) \quad (27)$$

The parameter Λ is defined by the relation

$$\Lambda^2 = 1 - \frac{(\gamma_2^2 - 1) \left[\frac{2}{\gamma_1 - 1} z_1 + 1 + \frac{2Q}{c^2} \right]}{\gamma_2^2 \left(1 + \frac{z_1}{\gamma_1}\right)^2} \quad (28)$$

$\Lambda = 0$ corresponds to a C-J detonation for which the velocity downstream of the detonative discontinuity is sonic with respect to the wave front. $\Lambda > 0$ corresponds to a strong or overdriven detonation while $\Lambda < 0$ corresponds to weak detonations which, from thermodynamic considerations, cannot exist.

As before $\lambda = \lambda_* = \text{const}$ at the detonative discontinuity in the self similar case. It is readily shown that choosing the convenient value $\lambda_* = 1.0$ is equivalent to

$$\lambda = r/r_s \quad (29)$$

as in the case of the blast wave solution.

In order to find R_2 , V_2 , and z_2 from Equation (25) through (27), it is necessary to know z_1 . Now

$$z_1 = \gamma R T_1 \frac{t^2}{r_s^2} = \frac{a_1^2}{c^2} = \frac{1}{M_D^2} \quad (30)$$

where M_D is the Mach number of the detonation. For a C-J wave M_D^2 can be determined in terms of Q , a_1 , γ_1 , and γ_2 from Equation (28) with $\Lambda = 0$.

The key problem is now to obtain a numerical solution of Equation (22) starting from the center of symmetry $V = 0$, $z = \infty$ and ending at the point $V = V_2$, $z = z_2$ at the C-J discontinuity. For this purpose it is useful to study the behavior of the solution in the z - V plane shown in Figure 2 below, where a C-J solution trajectory from the center of symmetry D to the undisturbed gas at $r \rightarrow \infty$ (point 0) is shown. The parabola $z = (1 - V)^2$ corresponds to points where the velocity is sonic with respect to the discontinuity and hence the point (V_2, z_2) at the C-J front lies on this parabola. The point A where $V = 0$, $z = 1.0$ is a singularity of Equation (22) and can be shown to be a nodal point. Hence, all C-J solutions pass through the point A. It is readily shown that

$$\left(\frac{dr}{dt}\right)_A = a \quad (31)$$

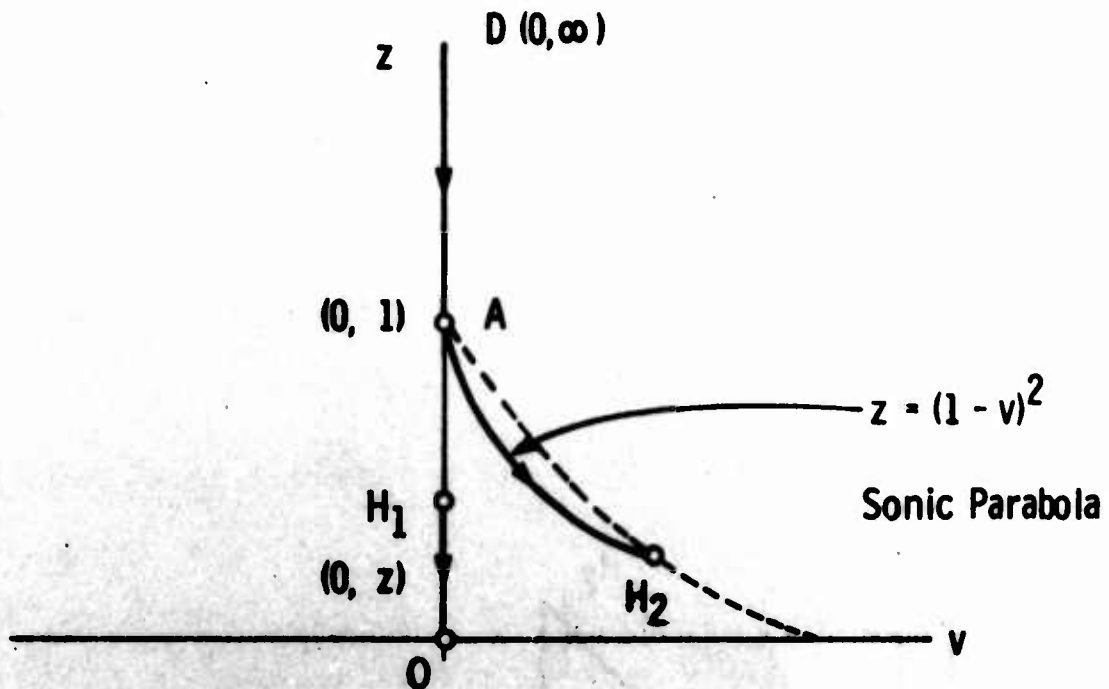


Figure 2. Behavior of Solution to Equation (22) in z - V Plane

In the physical plane the point A thus moves out with the speed of sound a and $r_A(t) = at$ is a characteristic separating a stationary core of fluid from an isentropic expansion behind the C-J front. Physically the flow will then be as shown in the graph of v versus r below. In both Figures 2 and 3 the arrow is in the direction of increasing λ .

The detailed behavior of $z(V)$ near the singularity A has been determined analytically and has been used in the numerical integration of Equation (22). From Equations (22) and (23) it is also possible to arrive at some interesting results regarding the velocity gradient dv/dr at the detonation front and on the characteristic $r = r_A$. Since

$$\lambda = (r/ct) \quad ; \quad v = (r/t) \quad V = \lambda cV$$

it follows that

$$\frac{dv}{dr} = \frac{1}{t} \left[V + \frac{1}{d(\ln \lambda)/dV} \right] \quad (32)$$

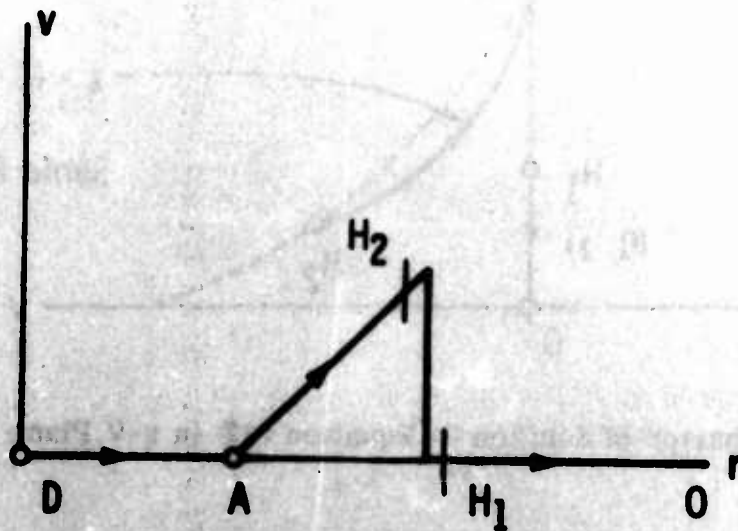


Figure 3. Behavior of Solution to Equation (22) in v - r Plane

At the detonation (point H_2 in the z - V plane) $d(\ln \lambda)/dV = 0$ for $\nu = 2, 3$ so that $(dv/dr) \rightarrow \infty$ immediately behind the detonation front for cylindrical and spherical waves. As indicated by Lee et al⁽⁵⁾, this raises the question whether true spherical and cylindrical C-J waves can exist. For planar waves with $\nu = 1$, dv/dr remains finite at the detonation. On the characteristic $r = r_A$ it can similarly be shown that $(dv/dr)_A$ remains finite for plane and cylindrical waves but $(dv/dr)_A = 0$ for spherical waves.

4. Comparison of the Blast Wave and C-J Wave Solutions

To show the difference in the behavior of the C-J and blast wave solutions we have compared these in the planar case. Specifically, the critical blast wave radius r_* which in the planar case is given by

$$r_* = E_0 / 2\rho_1 Q \quad (1a)$$

was chosen to be 20 feet and Q was based on a C-J detonation propagating through a stoichiometric methane (CH_4) air mixture. Such a mixture is representative of a typical hydrocarbon-air mixture. Knowing r_* , ρ_1 , and Q , the value of E_0 for the blast wave solution is readily calculated from Equation (1a).

For a detonation through a stoichiometric mixture of CH_4 and air at $p_1 = \text{atm}$, $T_1 = 537^\circ R$, Q is readily calculated following Eisen et al⁽¹⁰⁾ with the result that

$$Q = 1203.9 \text{ BTU/lbm}$$

and then from Equation (1a)

$$E_0 = 3405 \text{ BTU/ft}^2 = 2.649 \times 10^6 \text{ ft-lb/ft}^2$$

which is equivalent to 1.68 lbm of TNT per ft^2 . A constant value of $\gamma = 1.3$ was used in the calculations.

In Figures 4, 5, and 6 the variation of p , v , and T are shown for the blast wave as it propagates to the critical radius with the corresponding quantities shown for the C-J detonations in Figures 7, 8, and 9. It is evident that the blast wave and C-J wave flows are quite different. The presence of the quiescent core is evident in the C-J curves. The blast wave pressure is initially higher than the C-J value but rapidly drops to a value about equal to the constant pressure behind the C-J wave. The temperature T rises rapidly behind the blast wave, and $T \rightarrow \infty$ as $r \rightarrow 0$ for the blast solution which thus is not valid near $r = 0$. The density, which is not shown in the figures, drops off rapidly behind the blast wave, and in some approximate treatments it is assumed that the fluid in the region $r < r_g$ is concentrated in a small region behind the shock.

C. CALCULATION OF GROUND AND DYNAMIC IMPULSE

Both the ground impulse and the dynamic impulse are important parameters in assessing the effectiveness of fuel air explosions as compared, for example, to a blast wave with the same energy release. Both the total impulse imparted to the entire region enclosed by the wave front and the impulse per unit area at a point which is a fixed distance from the center of explosion have been considered.

1. Calculation of Total Impulse

The total impulse imparted to the ground by either a blast wave or a C-J wave is given by the integral

$$I(t) = 2 \int_0^t \int_0^{r_s} (p - p_1) dr dt \quad (33)$$

for planar waves, and by

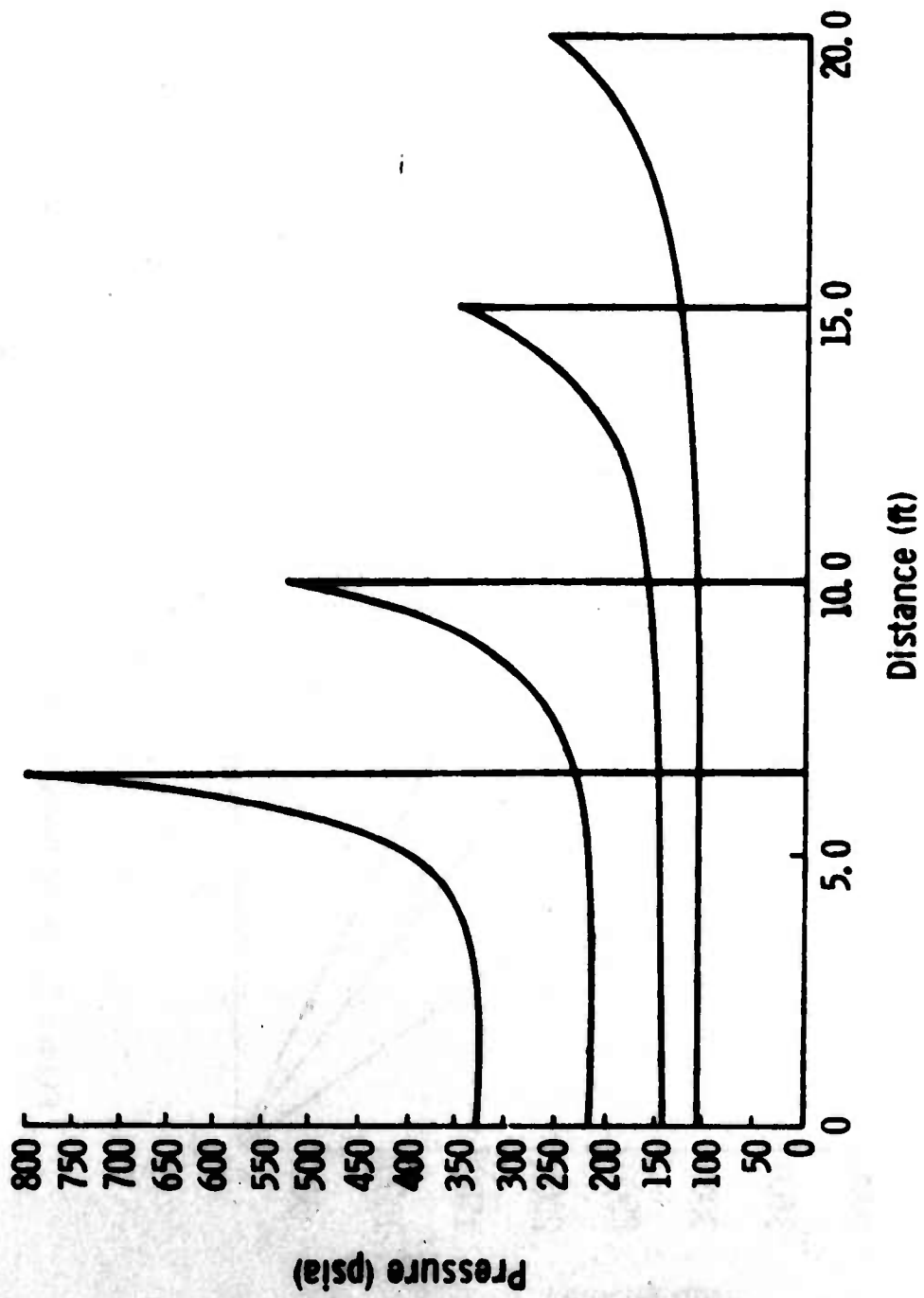


Figure 4. Blast Wave Solution Variation of Pressure

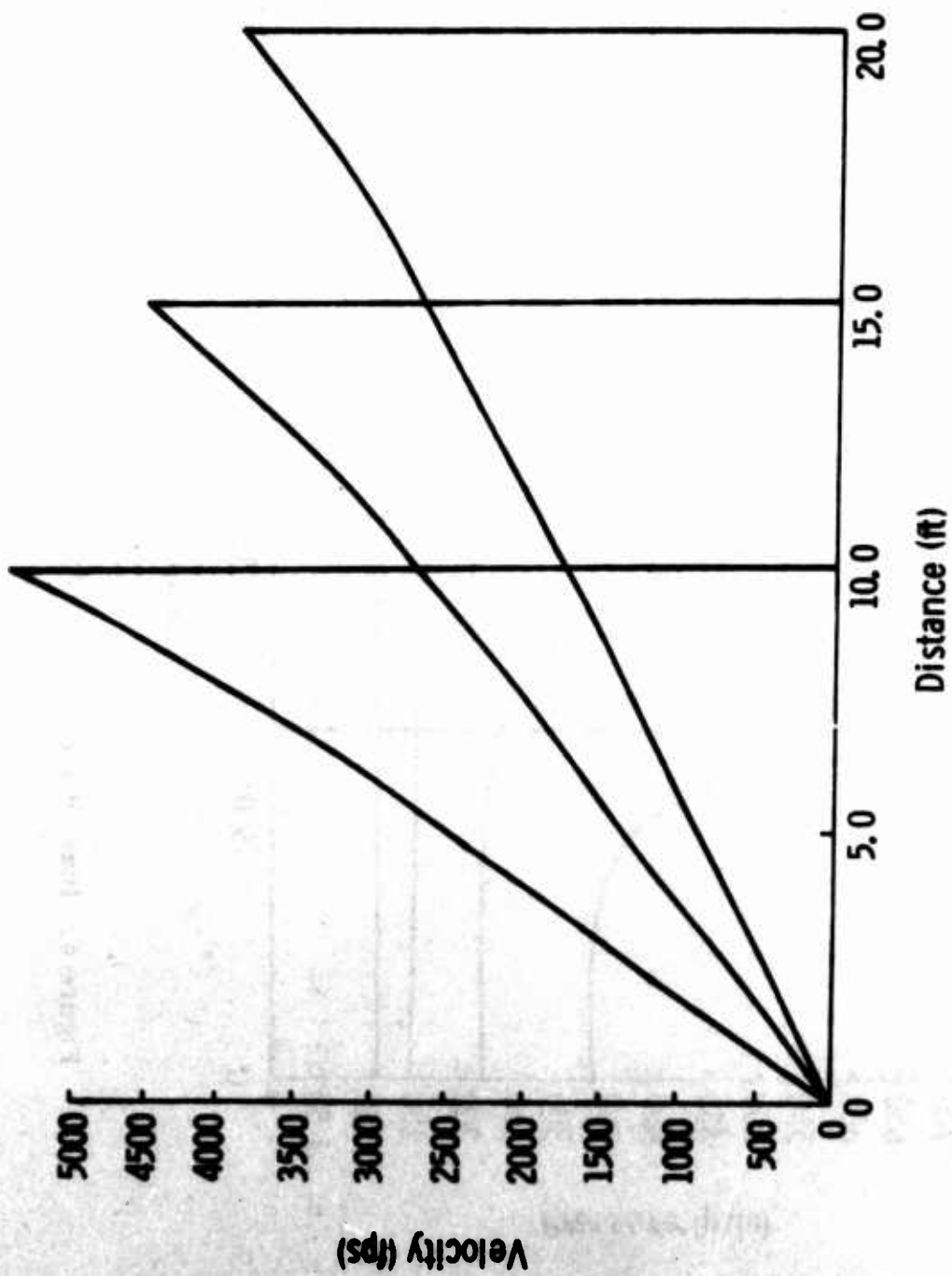


Figure 5. Blast Wave Solution Variation of Velocity

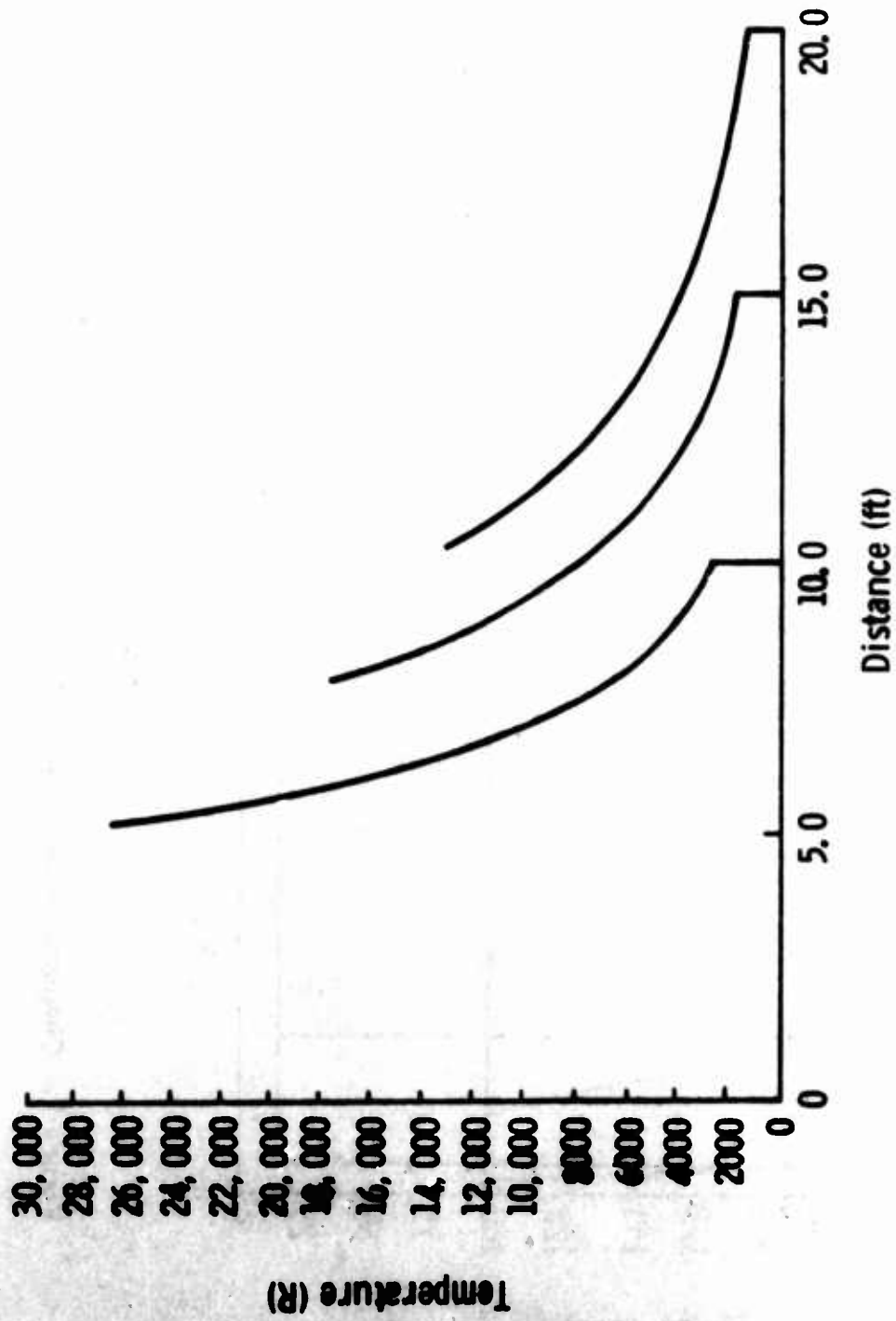


Figure 6. Blast Wave Solution Variation of Temperature

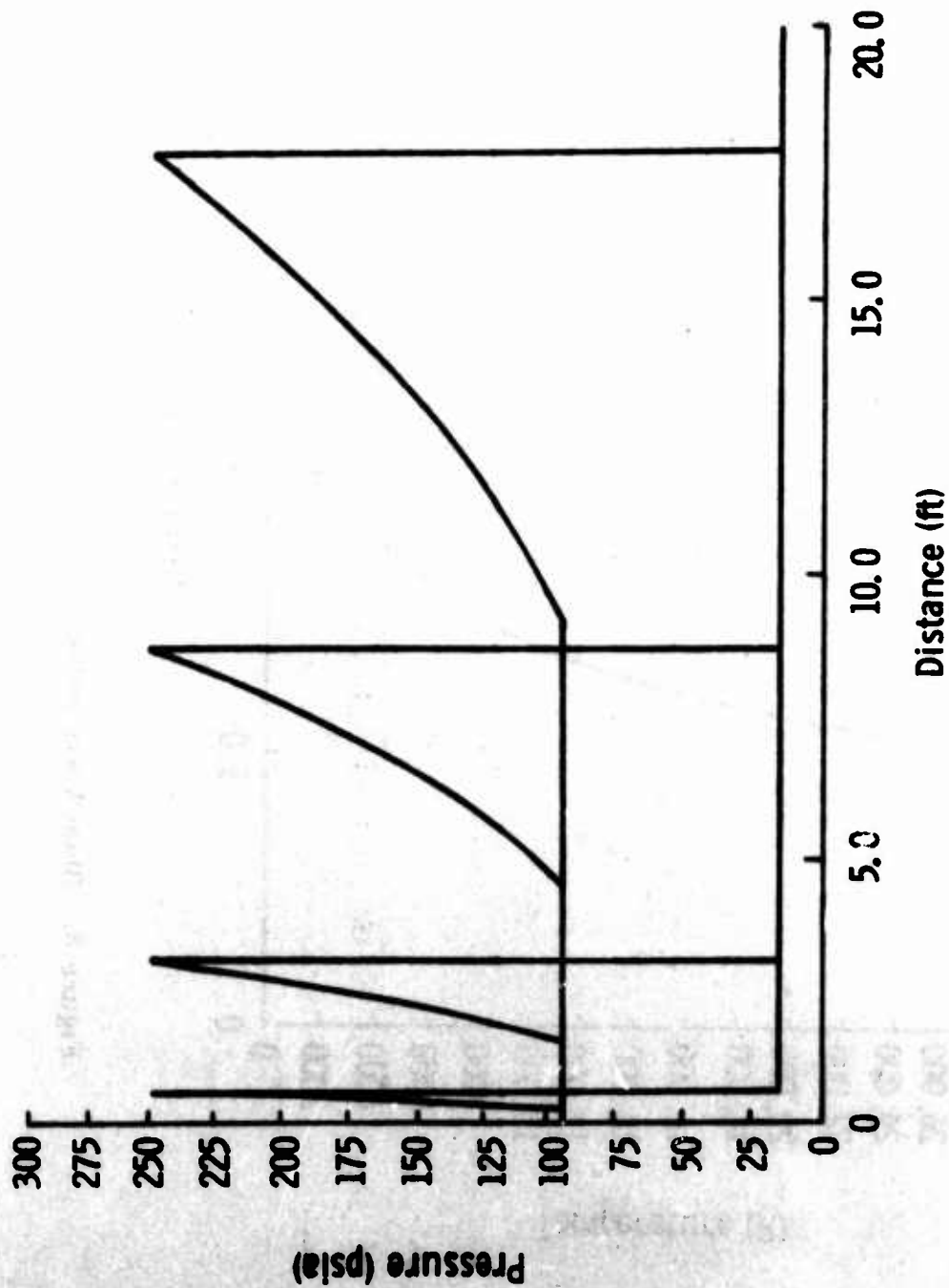


Figure 7. Chapman-Jouguet Detonation Variation of Pressure

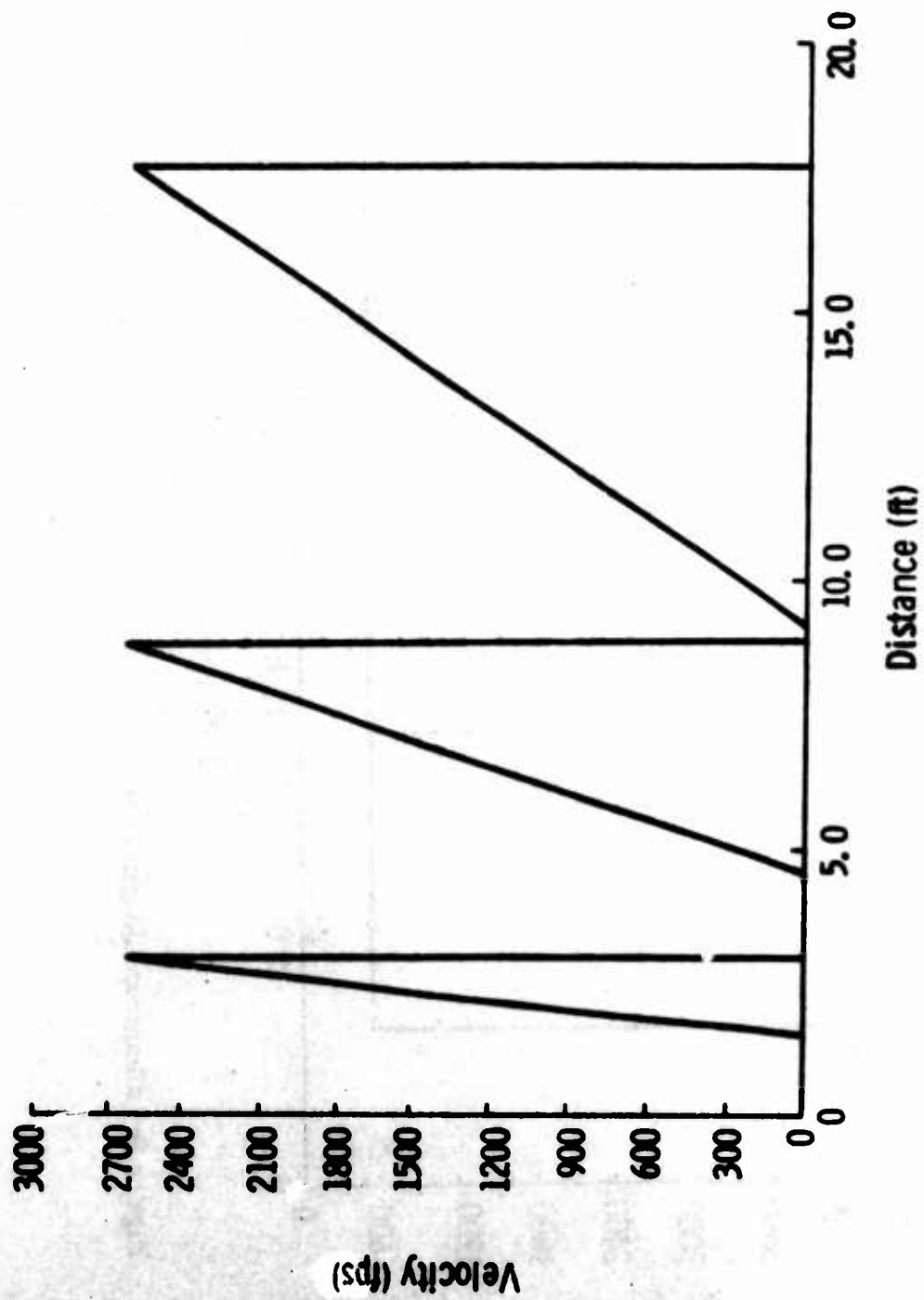


Figure 8. Chapman-Jouguet Detonation Variation of Velocity

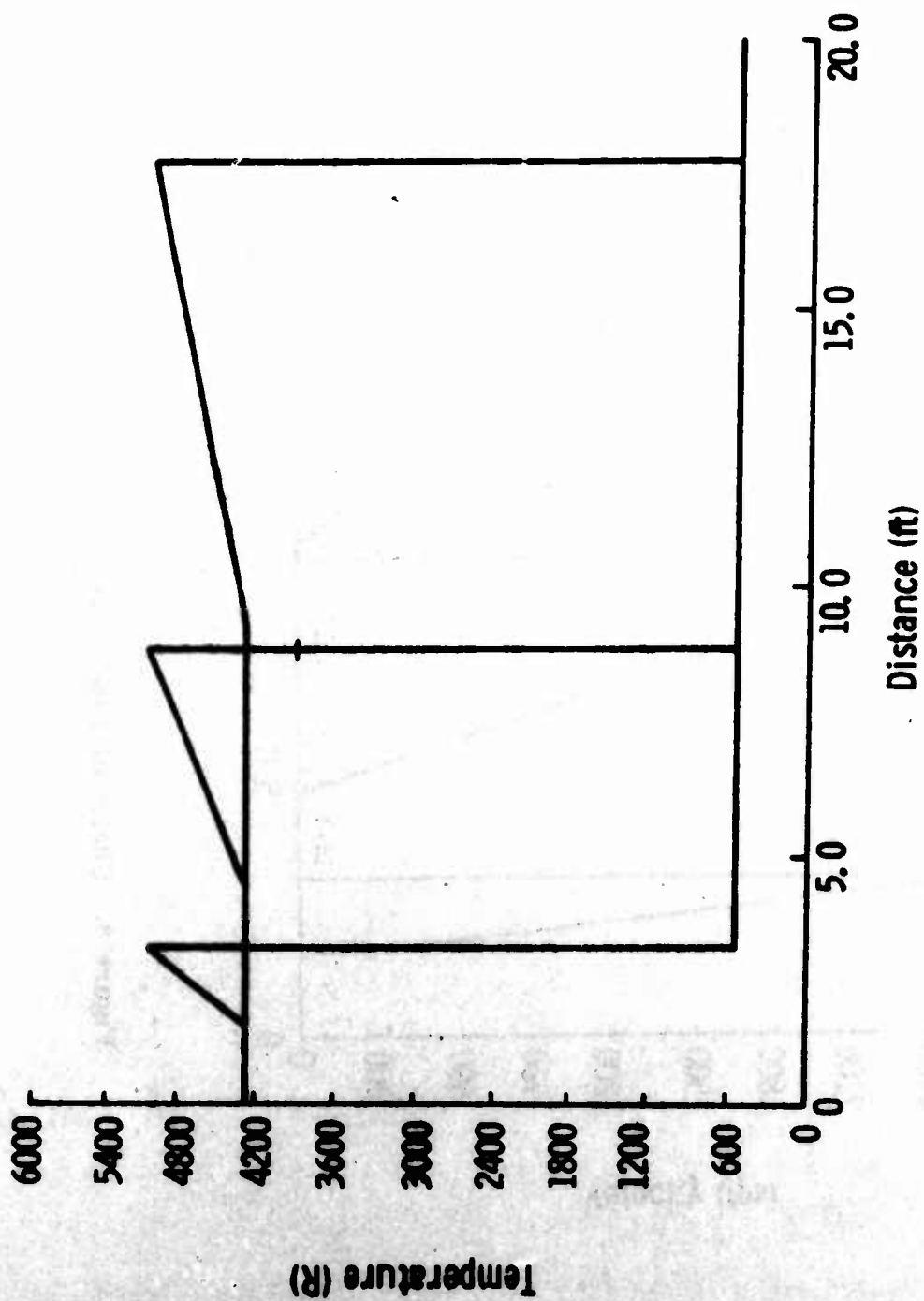


Figure 9. Chapman-Jouguet Detonation Variation of Temperature

$$\bar{I}(t) = 2\pi \int_0^t \int_0^s (p - p_1) r dr dt \quad (34)$$

for cylindrical and spherical waves, and $I(t)$ is, of course, a function of time. For the self similar blast wave and C-J solutions the integrals (33) and (34) can be reduced to a particularly simple form.

For strong blast waves $p_1 \ll p$ and hence can be neglected in (33) and (34). For plane and cylindrical symmetry, i.e., $\nu = 1, 2$, the inner integrals in (33) and (34), when expressed in terms of dimensionless variables, become

$$\int_0^s p \sigma_\nu r^{\nu-1} dr = \frac{E_0}{\alpha(\gamma)} \sigma_\nu \int_0^1 P \lambda^{\nu+1} d\lambda \quad (35)$$

The integral on the right side of Equation (35) will be a function only of γ for the self similar blast wave solution, hence letting

$$\beta(\gamma) = \int_0^1 P \lambda^{\nu+1} d\lambda \quad (36)$$

It is readily seen that the ground impulse due to a strong blast wave will be

$$\bar{I}(t) = \sigma_\nu E_0 \frac{\beta(\gamma)}{\alpha(\gamma)} t \quad ; \quad \nu = 1, 2 \quad (37)$$

that is, the ground impulse varies linearly with the time. The universal function $\beta(\gamma)$ must be evaluated numerically from the blast wave solution.

For spherical blast waves the situation is somewhat different for while the wave is spherical the ground impulse is still applied to a circular area, as in the cylindrical case. Then it is readily shown that

$$\bar{I}(t) = \frac{10}{3} \pi \rho_1 (E_0 / \alpha \rho_1)^{4/5} \left[\int_0^1 P \lambda^3 d\lambda \right] t^{3/5} \quad (38)$$

where now $P(\lambda)$ corresponds to the spherical blast solution. Not surprisingly, $\bar{I}(t)$ does not increase as rapidly for the spherical blast wave as for cylindrical and planar waves. It is important to note that in Equation (37), E_0 is blast energy per unit area or length. The impulse given by Equation (38) is that generated by a point explosion at the ground surface; however, since the spherical blast wave solution applies to an explosion in free space, E_0 in Equation (38) is twice the energy release of the ground explosion.

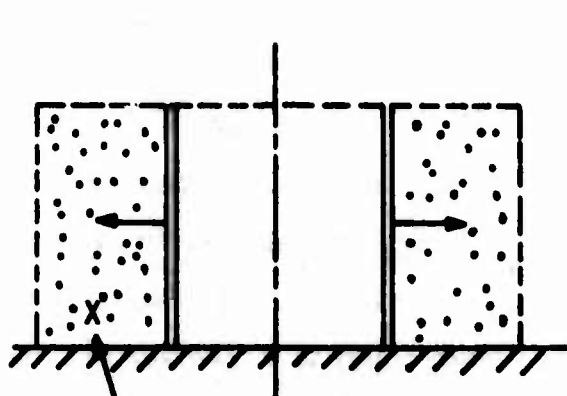
For planar and cylindrical C-J detonations the ground impulse from Equation (33) will be

$$\bar{I}(t) = \left[\rho_1 \sigma_\nu c^{2+\nu} \int_0^1 P \lambda^{\nu+1} d\lambda - \frac{P_1 \sigma_\nu c^\nu}{\nu} \right] \frac{t^{\nu+1}}{\nu+1} \quad (39)$$

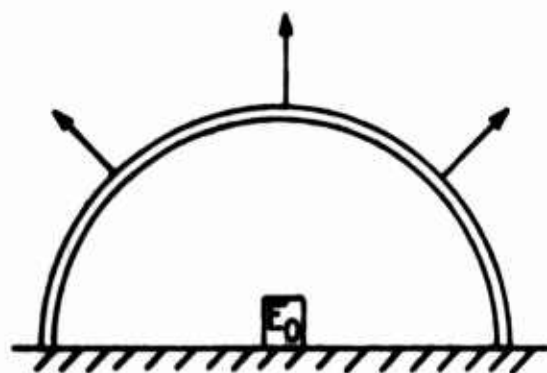
The quantity within the brackets will be constant for any given fuel oxidizer mixture; thus, the ground impulse from planar and cylindrical detonations varies as t^2 and t^3 , respectively. The ground impulse produced by a hemispherical C-J detonation can be obtained from Equation (39) with $\nu = 2$ but with $P(\lambda)$ evaluated from the solution for a spherical C-J detonation.

Equations (37) through (39) provide a relatively simple means of comparing the ground impulse from various types of waves. The variation of $\bar{I}(t)$ with wave radius also is readily established from Equations (37) through (39). Thus, $\bar{I}(t) \propto r_s^{3/2}$, r_s^2 , and $r_s^{3/2}$ for plane, cylindrical, and hemispherical waves.

Actually geometric considerations indicate that the comparison of a cylindrical FAE to a cylindrical blast wave is not an appropriate basis. Thus, as shown in Figure 10 below, if all the combustion energy in a



E_0 = cloud energy content



Equivalent hemispherical
blast wave

Figure 10. Fuel Air Explosions, Geometric Considerations

cylindrical FAE were concentrated at one point and released instantaneously, the result would be a spherical rather than a cylindrical blast wave. Consequently, the appropriate comparison with regard to ground impulse is between a spherical blast and a cylindrical FAE and such comparisons can be made using the results developed above.

Because of the induced velocity there will be a dynamic force on any body or obstacle located in the wake of either the blast wave or the detonation. The behavior of an object in the path of the wave is shown qualitatively in Figure 11 below. As the shock sweeps over the obstacle, it is diffracted, and the flow during this diffraction process will be unsteady and quite complex. After sufficient time has elapsed, it seems reasonable to assume that the flow will be quasi-steady, that is, at any instant the flow will behave like a steady flow with a free stream velocity equal to v , the velocity behind the shock or blast wave.

During the quasi-steady portion of the flow the maximum pressure on the body will equal the local stagnation pressure p_o and will occur at the forward stagnation point. There are now several ways of estimating the fluid dynamic force on a body in the flow. The maximum force per unit area will be of the order of $p_o - p$ where p is the static pressure so one estimate for the impulse at a given position might be

$$I_d = \int_0^t (p_o - p) dt \quad (40)$$

Another approach would be to use

$$I_d = \int_0^t \frac{\rho v^2}{2} A_f C_D dt \quad (41)$$

where A_f is the frontal area of the body and C_D is the drag coefficient. If the flow is subsonic, as for instance behind a C-J detonation, it is possible

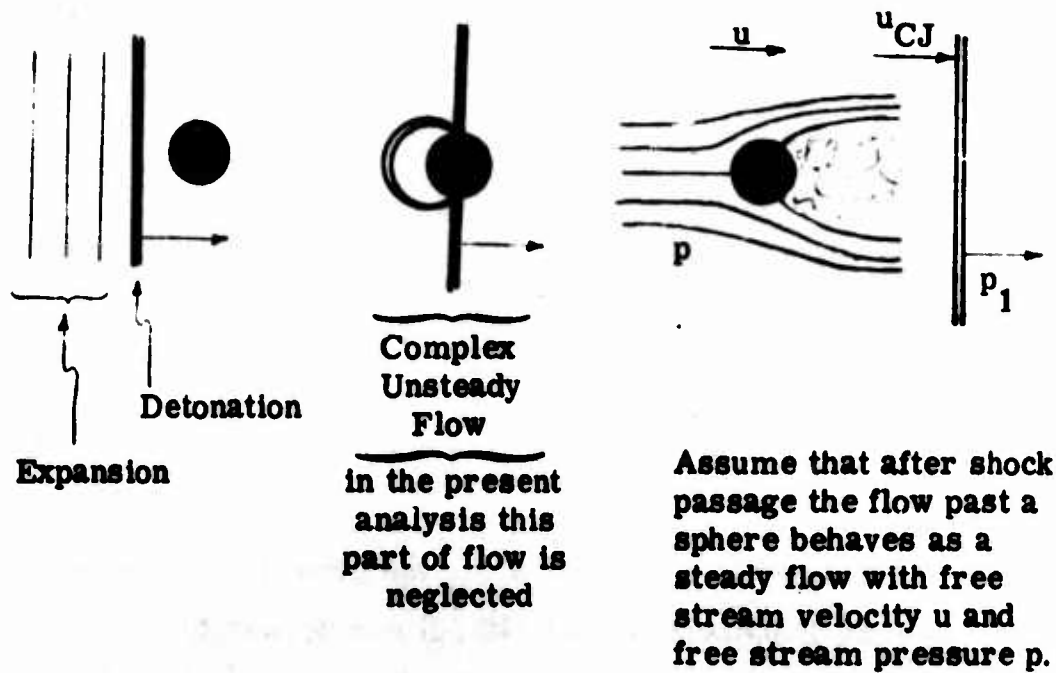


Figure 11. Behavior of an Object in the Wake of Blast or Detonation Wave

to assume isentropic flow in computing p_o . Then if the gas behind the wave is assumed perfect,

$$\frac{p_o}{p} = \left[1 + \frac{\gamma_2 - 1}{2} M^2 \right]^{\gamma_2/(\gamma_2 - 1)}$$

where γ_2 is the ratio of specific heats and M is the Mach number. Generally $[(\gamma_2 - 1)/2] M^2 \ll 1$. Even when $M = 1.0$, $[(\gamma_2 - 1)/2] M^2 \cong 0.1$. Then

$$\frac{p_o}{p} \cong 1 + \frac{\gamma_2}{2} M^2 = \frac{\gamma_2 v^2}{2a^2} + 1 = \frac{\rho v^2}{2} + 1$$

In this case Equation (40) becomes

$$I_d = \int_0^t \frac{\rho v^2}{2} dt \quad (42)$$

Here Equation (42) is used as a measure of I_d , the dynamic impulse on an obstacle. Comparing Equations (41) and (42), it can be seen that

$$C_D A_f I_d = \text{impulse on body with} \\ \text{drag coefficient } C_D \\ \text{and frontal area } A_f.$$

It should be emphasized that the effects of the shock diffraction on the impulse applied to any body in the flow is neglected in using Equation (42) as a measure of the dynamic impulse. The correctness of this assumption should be investigated.

The impulse as written in Equation (42) represents the dynamic impulse felt by a body at some fixed distance from the explosion center. The detailed evaluation of this quantity shall be considered below. First, however, measure of the overall impulse induced by the wave is needed. For planar and cylindrical waves the total dynamic impulse induced by the

wave in a region of unit height shall be used so that the total dynamic impulse \bar{I}_d becomes

$$\bar{I}_d = \sigma \nu \int_0^t \int_0^s \frac{\rho v^2}{2} r^{\nu-1} dr dt \quad (43)$$

For a strong blast wave Equation (43) can be reduced to

$$\bar{I}_d = \left[\sigma \nu \frac{E_c}{\alpha(\gamma)} \int_0^1 \frac{RV^2}{2} \lambda^{\nu+1} d\lambda \right] t \quad (44)$$

which is very similar to the result for the total ground impulse. In the case of the strong blast wave, a combination of Equation (43) and (35) and the definition of $\alpha(\gamma)$ in Equation (17) leads to the result

$$\bar{I}_d + \frac{\bar{I}}{\gamma - 1} = E_0 t \quad (45)$$

so that an expression representing what is, in essence, a combined dynamic and ground impulse is directly proportional to the blast energy and the time, in the case of planar and cylindrical waves.

In spherical waves it is more difficult to define a total dynamic impulse which can be related to dynamic effects in the region enclosed by the wave. In particular, it becomes difficult to compare total ground and total dynamic impulse since the ground impulse is applied to a circular area just as for cylindrical waves. If $\rho v^2/2$ is summed over the volume of the sphere, the total dynamic impulse is that given by Equation (44) with $\nu = 3$, or one-half that value for a hemisphere bounded by the ground. The simple relation [Equation (45)] cannot be applied in the spherical case.

For C-J detonations the total dynamic impulse will be given by

$$\bar{I}_d = \left[\frac{\sigma_\nu \rho_1 C^{\nu+2}}{2} \int_0^1 R V^2 \lambda^{\nu+1} d\lambda \right] \frac{t^{\nu+1}}{\nu+1} \quad (46)$$

2. The Impulse at a Fixed Point

The ground and dynamic impulse per unit area at a point a fixed distance from the center of explosion will now be considered. In particular, the ground impulse due to a plane C-J detonation travelling down a closed tube and the dynamic impulse due to a spherical C-J detonation have been completed. By making suitable approximations, universal functions have been derived which can be used to compute ground and dynamic impulse, in general, for these two configurations.

In the case of a detonation propagating down a closed end tube, the key boundary condition is that the velocity of the fluid must be zero at the end of the tube. Consequently, the C-J detonation is followed by an isentropic expansion in which the velocity of the fluid drops to zero as shown, for example, in Figures 7, 8, and 9. The problem of the detonation travelling down a closed tube has been treated by Sedov⁽⁶⁾ and Taylor⁽¹¹⁾ among others.

In this discussion the C-J wave is treated as an exothermic discontinuity. Immediately behind the C-J wave

$$p = \text{pressure} = p_{CJ}$$

and the velocity of the fluid is sonic with respect to the wave front, i. e.,

$$D - u_{CJ} = a_{CJ}$$

where a_{CJ} is the speed of sound in the burned gases immediately behind the front, and D is here used for the propagation velocity. As before, the gas behind the detonation is assumed to behave as a perfect gas.

Within the isentropic expansion behind the wave the pressure is given by the expression⁽¹¹⁾

$$p = p_{CJ} \left[1 - \frac{D}{a_{CJ}} \left(\frac{\gamma_2 - 1}{\gamma_2 + 1} \right) + \frac{r}{t} \frac{(\gamma_2 - 1)}{a_{CJ} (\gamma_2 + 1)} \right]^{2\gamma_2/\gamma_2 - 1} ; \quad (47)$$

thus, when $r = r_s = Dt$, $p = p_{CJ}$ according to Equation (47). The isentropic expansion is terminated at the point where the velocity u drops to zero where then

$$r = r_2 = \frac{1}{2} \left[a_{CJ} (\gamma_2 + 1) - D(\gamma_2 - 1) \right] t \quad (48)$$

and

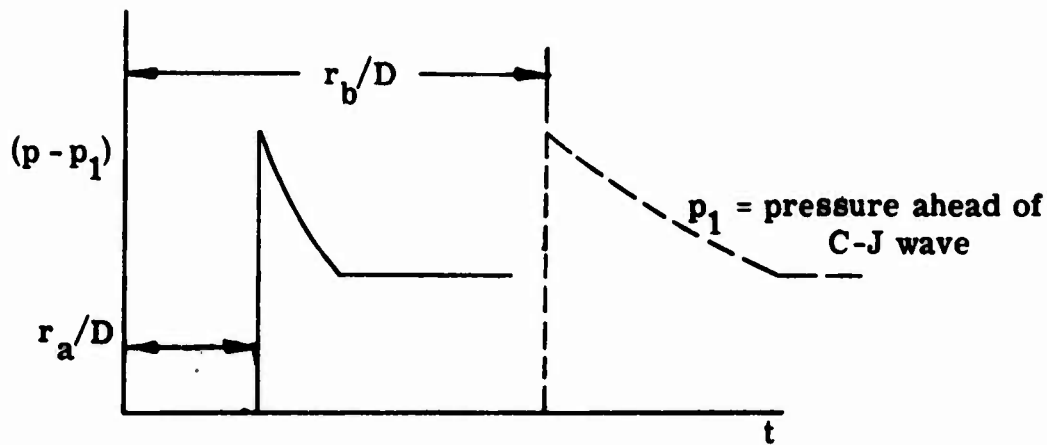
$$p = p_2 = p_{CJ} \left[\frac{1}{2} (\gamma_2 + 1) - \frac{1}{2} (\gamma_2 - 1) \frac{D}{a_{CJ}} \right]^{2\gamma_2/\gamma_2 - 1} \quad (49)$$

The length of the region occupied by the expansion is

$$\begin{aligned} r_s - r_2 &= Dt - \frac{1}{2} [a_{CJ} (\gamma_2 + 1) - D(\gamma_2 - 1)] t \\ &= \frac{\gamma_2 + 1}{2} (D - a_{CJ}) t \end{aligned} \quad (50)$$

and increases in length with time t . This can also be observed in Figures 7, 8, and 9.

In view of the discussion above the variation of pressure at a fixed position along the detonation tube would be as indicated below:



$p(t)$ is shown for two values of r , r_a and r_b with $r_b > r_a$. For a fixed radius the variation of the pressure is given by

$$p - p_1 = 0 \quad ; \quad \text{for } t < \frac{r}{D} = t_s \quad (51)$$

$$p - p_1 = p_{CJ} \left[1 - \frac{D}{a_{CJ}} \left(\frac{\gamma_2 - 1}{\gamma_2 + 1} \right) + \frac{r}{t} \frac{(\gamma_2 - 1)}{a_{CJ} (\gamma_2 + 1)} \right]^{2\gamma_2/\gamma_2 - 1} - p_1 \quad (52)$$

for

$$t_s < t < \frac{r}{\frac{1}{2} [a_{CJ} (\gamma_2 + 1) - D(\gamma_2 - 1)]} = t_2$$

and

$$p - p_1 = p_2 - p_1 = p_{CJ} \left[\frac{1}{2} (\gamma_2 + 1) - \frac{1}{2} (\gamma_2 - 1) \frac{D}{a_{CJ}} \right]^{2\gamma_2/\gamma_2 - 1} - p_1 \quad (53)$$

for

$$t > t_2$$

The ground impulse I per unit area at a fixed r is defined by the integral

$$I(r, t) = \int_0^t (p - p_1) dt \quad (54)$$

From Equations (51), (52), and (53), it follows that

$$I(r, t) = 0 \quad ; \quad t < t_s \quad (55)$$

$$I(r) = \int_{t_s}^t \left\{ p_{CJ} \left[1 - \frac{D}{a_{CJ}} \left(\frac{\gamma_2 - 1}{\gamma_2 + 1} \right) + \frac{r}{t} \frac{(\gamma_2 - 1)}{a_{CJ}(\gamma_2 + 1)} \right]^{\frac{2\gamma_2}{\gamma_2 - 1}} - p_1 \right\} dt \quad (56)$$

$$t_s < t < t_2$$

$$I(r) = \int_{t_s}^{t_2} \left\{ p_{CJ} \left[1 - \frac{D}{a_{CJ}} \left(\frac{\gamma_2 - 1}{\gamma_2 + 1} \right) + \frac{r}{t} \frac{(\gamma_2 - 1)}{a_{CJ}(\gamma_2 + 1)} \right]^{\frac{2\gamma_2}{\gamma_2 - 1}} - p_1 \right\} dt \quad (57)$$

$$+ (p_2 - p_1)(t - t_2)$$

$$t > t_2$$

The expressions for ground impulse can be reduced to the following dimensionless form in terms of the similarity variable $\lambda = r/Dt$, and a dimensionless impulse \hat{I} given by

$$\hat{I}(r, t) = 0 \quad \text{for} \quad \lambda > 1 \quad (58)$$

$$\hat{I} = \frac{ID}{p_{CJ}r} = \frac{I}{p_{CJ}t_s} = \int_{\lambda}^1 \frac{\left[1 + \frac{D}{a_{CJ}} \frac{\gamma_2 - 1}{\gamma_2 + 1} (\lambda - 1) \right]^{\frac{2\gamma_2}{\gamma_2 - 1}}}{\lambda^2} d\lambda - \frac{p_1}{p_{CJ}} \left(\frac{1}{\lambda} - 1 \right) \quad (59)$$

for

$$\lambda_2 < \lambda < 1$$

where

$$\lambda_2 = \frac{r}{Dt_2} = \frac{1}{2} \left[\frac{a_{CJ}}{D} (\gamma_2 + 1) - (\gamma_2 - 1) \right]$$

$$\hat{I} = \frac{ID}{p_{CJ} r} = \frac{I}{p_{CJ} t_s} = \int_{\lambda_2}^1 \frac{\left[1 + \frac{D}{a_{CJ}} \frac{\gamma_2 - 1}{\gamma_2 + 1} (\lambda - 1) \right]^{2\gamma_2/\gamma_2 - 1}}{\lambda^2} d\lambda$$

$$+ \frac{p_2}{p_{CJ}} \left(\frac{1}{\lambda} - \frac{1}{\lambda_2} \right) - \frac{p_1}{p_{CJ}} \left(\frac{1}{\lambda} - 1 \right) \quad (60)$$

For

$$\lambda < \lambda_2$$

The expressions (58) through (60) are in a universal form. The dimensionless integrals only need to be evaluated once for a given γ_2 and D/a_{CJ} . It should be noted that D/a_{CJ} is also equal to the density ratio across the C-J detonation.

The dependence of I on the radius of the point where I is to be evaluated enters through the quantity t_s and through the definition of λ as (r/Dt) .

3. Chapman-Jouguet Condition

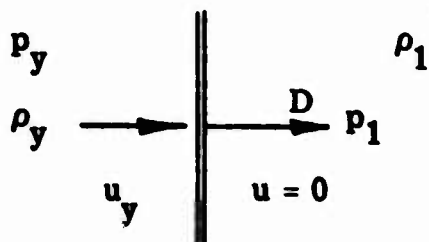
Evaluation of I from the dimensionless Equations (58), (59), and (60) requires a knowledge of

$$D, \quad p_{CJ}/p_1, \quad p_2/p_{CJ}, \quad D/a_{CJ}, \quad \lambda_2$$

and these quantities can be determined by using conservation laws across the detonation together with the Jouguet hypothesis that the velocity of the

fluid downstream of the wave moves with sonic velocity with respect to a wave front. It is here that suitable approximations can result in great simplification.

For the wave shown below (not necessarily C-J)



with u_y the velocity immediately downstream of the wave, the conservation equations are

$$\text{Mass} \quad \rho_1 D = \rho_y (D - u_y) \quad (61)$$

$$\text{Momentum} \quad \rho_1 D^2 + p_1 = \rho_y (D - u_y)^2 + p_y \quad (62)$$

$$\text{Energy} \quad e_1 + \frac{p_1}{\rho_1} + \frac{D^2}{2} = e_y + \frac{p_y}{\rho_y} + \frac{(D - u_y)^2}{2} \quad (63)$$

where now the velocity is denoted by u . In Equation (63), e_1 and e_y are the specific internal energy of the fluid including the chemical heats of formation. If A_i are the reactants and B_i are the products in the equilibrium mixture downstream of the detonation, then

$$e_1 + \frac{p_1}{\rho_1} = \frac{\sum a_i [H(T_1) - H(T_0) + \Delta H_f^0]_{A_i}}{\sum a_i \lambda_{A_i}} \quad (64)$$

\mathcal{M}_{A_i} = molecular weight of species A_i

a_i, b_i = number of moles of each species of reactant and products

ΔH_f^0 = standard heat of formation

T_0 = reference temperature (e.g., may be 0°K)

Also

$$e_y + \frac{p_y}{\rho_y} = \frac{\sum b_i [H(T_2) - H(T_0) + \Delta H_f^0]_{B_i}}{\sum b_i \mathcal{M}_{B_i}} \quad (65)$$

In the case of gaseous detonations, both the reactants and products satisfy the perfect gas equation of state although the ratio of specific heats, the specific heats, and the gas constant will change across the wave. Then the energy equation is often written in the form

$$Q + \frac{D^2}{2} + \frac{\gamma_1}{\gamma_1 - 1} \left(\frac{p_1}{\rho_1} \right) = \frac{1}{2} (D - u_2)^2 + \frac{\gamma_2}{\gamma_2 - 1} \left(\frac{p_2}{\rho_2} \right) \quad (63a)$$

where now

$$\frac{\gamma_2}{\gamma_2 - 1} \left(\frac{p_2}{\rho_2} \right) = \frac{\sum b_i [H(T_2) - H(T_0)]_{B_i}}{\sum b_i \mathcal{M}_{B_i}} \quad (66)$$

$$\frac{\gamma_1}{\gamma_1 - 1} \left(\frac{p_1}{\rho_1} \right) = \frac{\sum a_i [H(T_1) - H(T_0)]_{A_i}}{\sum a_i \mathcal{M}_{A_i}} \quad (67)$$

and presumably $T_0 = 0^\circ\text{K}$ is used as a reference. The quantity Q is related to the chemical heat release per unit mass of fuel-oxidizer mixture and is given by

$$Q = \frac{\sum a_i (\Delta H_f^\circ)_{A_i} - \sum b_i (\Delta H_f^\circ)_{B_i}}{\sum a_i m_{A_i}} \quad (68)$$

It is noted that $\sum a_i m_{A_i} = \sum b_i m_{B_i}$ since mass must be conserved in the combustion reaction.

The equations of state on the two sides of the detonation are now

$$p_1 = \rho_1 R_1 T_1 \quad p_y = \rho_y R_y T_y \quad (69)$$

$$C_{p_1} = \frac{\gamma_1 R_1}{\gamma_1 - 1}, \quad a_1^2 = \gamma_1 R_1 T_1 \quad C_{p_y} = \frac{\gamma_y R_y}{\gamma_y - 1}, \quad a_y^2 = \gamma_y R_y T_y$$

Using the perfect gas equations and the energy equation in the form (63a) and the Jouguet Hypothesis which requires that

$$(D - u_y) = a_y = a_{CJ} \quad (70)$$

it is readily shown that the density ratio across a C-J detonation is given by

$$\frac{\rho_{CJ}}{\rho_1} = \left[\frac{\gamma_2}{\gamma_2 + 1} \left(1 + \frac{1}{\gamma_1 M_D^2} \right) \right]^{-1} \quad (71)$$

where

$M_D = D/a_1 =$ Mach number of the detonation

$\gamma_y = \gamma_{CJ} = \gamma_2 =$ constant in burned products.

For most detonations $\gamma_1 \sim 1.3-1.4$ while $M_D > 3$. Hence, $\gamma_1 M_D^2 \gg 1$ so that

$$\frac{\rho_{CJ}}{\rho_1} \cong \frac{\gamma_2 + 1}{\gamma_2} \quad (72)$$

i. e., the density ratio is essentially independent of the heat release across the detonation or of the detonation Mach number M_D . For many fuel-air mixtures $\gamma_2 \simeq 1.2$ so that

$$\frac{\rho_{CJ}}{\rho_1} \cong \frac{2.2}{1.2} = 1.83 \quad (73)$$

In any case ρ_{CJ}/ρ_1 does not vary greatly with γ_2 as is evident from the following tabulation:

γ_2	1.1	1.2	1.3	1.4
$\frac{\gamma_2 + 1}{\gamma_2}$	1.91	1.83	1.77	1.71

Exact calculation of Taylor⁽¹¹⁾ and Lewis and von Elbe¹² yielded the following results for ρ_{CJ}/ρ_1 :

Fuel-Oxidizer	$H_2 + \frac{1}{2} O_2$	$CO + O$	$C_2H_2 + 10O_2$	$CH_4 + 2O_2$
ρ_{CJ}/ρ_1	1.78	1.88	1.84	1.904

For almost all C-J detonations it appears that ρ_{CJ}/ρ_1 lies in the vicinity of 1.8. In the case of $H_2 + (1/2) O_2$, $\gamma_2 = 1.215$ so that $(\gamma_2 + 1)/\gamma_2 = 1.82$. The approximate relation [Equation (72)] thus appears to be quite accurate.

It is readily shown that the pressure ratio, p_{CJ}/p_1 , is given by

$$\frac{p_{CJ}}{p_1} = \frac{1 + \gamma_1 M_D^2}{1 + \gamma_2} \quad (74)$$

and p_{CJ}/p_1 will depend very strongly on M_D^2 . Following the treatment in Sedov, it is readily shown that

$$z_1 = 1/M_D^2$$

satisfies the quadratic equation

$$z_1^2 - 2z_1 \beta + \frac{\gamma_1^2}{\gamma_2^2} = 0 \quad (75)$$

where

$$\beta = \frac{\gamma_1^2 (\gamma_2^2 - 1)}{\gamma_2^2 (\gamma_1 - 1)} (1 + \hat{Q}) - \gamma_1$$

and where the dimensionless heat release per unit mass, \hat{Q} is defined as

$$\hat{Q} = \frac{Q}{C_{p1} T_1}$$

The solution of Equation (75) is

$$z_1 = \beta \pm \sqrt{\beta^2 - \frac{\gamma_1^2}{\gamma_2^2}} \quad (76)$$

and the solution with the positive sign must be rejected here since it leads to $M_D < 1$.

For almost all detonations $\hat{Q} \gg 1$. For instance, assigning an approximate heating value of 19,000 BTU/lbm of fuel to methane yields $\hat{Q} \sim 8$ for a stoichiometric methane air mixture at 520°R. With $\hat{Q} \gg 1$ it follows from the definition of β and Equation (76) that

$$M_D^2 \cong 2 \frac{(\gamma_2^2 - 1)}{(\gamma_1 - 1)} \hat{Q} \quad (77)$$

or

$$D^2 \cong 2(\gamma_2^2 - 1) Q \quad (77a)$$

Again, since $\hat{Q} \gg 1$, $\gamma_1 M_D^2 \gg 1$, it follows from Equations (32) and (29) that

$$\frac{p_{CJ}}{p_1} \cong 2\gamma_1 \left(\frac{\gamma_2 - 1}{\gamma_1 - 1} \right) \hat{Q} \quad (78)$$

Actually when γ_1 , γ_2 and the pressure ratio are known, Equation (78) can be used to compute the dimensionless heat release \hat{Q} . For instance, in the case of $H_2 + (1/2) O_2$, $\gamma_1 = 1.4$, $\gamma_2 = 1.215$, $p_{CJ}/p_1 = 18.05$ so that $\hat{Q} = 2.0$.

Finally, the temperature ratio, T_{CJ}/T_1 across the wave can be obtained from

$$\frac{T_{CJ}}{T_1} = \frac{p_{CJ}}{p_1} \frac{\rho_1}{\rho_{CJ}} \frac{R_1}{R_2} \cong 2\gamma_1\gamma_2 \frac{(\gamma_2 - 1)}{(\gamma_1 - 1)(\gamma_2 + 1)} \hat{Q} \frac{\mathcal{M}_2}{\mathcal{M}_1} \quad (79)$$

where \mathcal{M} is the molecular weight.

4. Evaluation of Ground Impulse*

An evaluation of ground impulse will now be considered. It is necessary to evaluate the integral $\mathcal{I}(\lambda)$:

$$\mathcal{I}(\lambda) = \int_{\lambda}^1 \frac{1}{\lambda^2} \left[1 + \frac{D}{a_{CJ}} \frac{\gamma_2 - 1}{\gamma_2 + 1} (\lambda - 1) \right]^{2\gamma_2/(\gamma_2 - 1)} d\lambda \quad (80)$$

*Section C. 4 and C. 5 are natural outgrowths of the foregoing material. The information reported in these two sections was originally done for Dr. Norman Slagg of Picatinny Arsenal under a consulting arrangement. For the sake of continuity and completeness, the information is also presented here.

Now using

$$\frac{D}{a_{CJ}} = \frac{\rho_{CJ}}{\rho_1} \approx \frac{\gamma_2 + 1}{\gamma_2}$$

$\mathcal{J}(\lambda)$ becomes

$$\mathcal{J}(\lambda) = \int_{\lambda}^1 \frac{1}{\lambda^2} \left[1 + \frac{\gamma_2 - 1}{\gamma_2} (\lambda - 1) \right]^{2\gamma_2/(\gamma_2 - 1)} d\lambda \quad (80a)$$

Although the integral (80a) can be determined analytically, it is computationally simpler to evaluate (80a) numerically using, e.g., the trapezoidal rule. The integrand of (80a) is tabulated for three different values of γ below:

λ	$\frac{1}{\lambda^2} \left[1 + \frac{\gamma_2 - 1}{\gamma_2} (\lambda - 1) \right]^{2\gamma_2/(\gamma_2 - 1)}$		
	$\gamma_2 = 1.1$	$\gamma_2 = 1.2$	$\gamma_2 = 1.3$
0.5	1.44	1.41	1.390
0.6	1.23	1.22	1.21
0.7	1.11	1.10	1.10
0.8	1.042	1.042	1.040
0.9	1.010	1.010	1.010
1.0	1.000	1.000	1.000

It can be seen that over the range of interest the integrand of Equation (80a) and hence $\mathcal{J}(\lambda)$ is independent of γ_2 and thus may be considered as a universal function.

For $\lambda < \lambda_2$, it is necessary to know both λ_2 and p_2/p_{CJ} . Using the result $a_{CJ}/D = \rho_1/\rho_{CJ} \approx \gamma_2/(\gamma_2 + 1)$, it follows that $\lambda_2 = 1/2$ so that λ_2

is independent of γ_2 , Q , etc. Also

$$\frac{p_2}{p_{CJ}} = \left[\frac{1}{2} (\gamma_2 + 1) - \frac{1}{2} (\gamma_2 - 1) \frac{D}{a_{CJ}} \right]^{2\gamma_2/(\gamma_2-1)} \approx \left[\frac{1}{2} (\gamma_2 + 1) \frac{1}{\gamma_2} \right]^{2\gamma_2/(\gamma_2-1)} \quad (81)$$

p_2/p_{CJ} is tabulated versus γ_2 below

γ_2	=	1.1	1.2	1.3
p_2/p_{CJ}	\approx	0.368	0.358	0.348

and it can be seen that p_2/p_{CJ} is essentially independent of γ_2 in the range of interest.

The dimensionless impulse \hat{I} now becomes

$$\begin{aligned} \hat{I} &= 0, \quad \lambda > 1 \\ \hat{I} &= \lambda - (p_1/p_{CJ})[(1/\lambda) - 1]; \quad 1/2 < \lambda < 1 \\ \hat{I} &= \lambda(1/2) + 0.358[(1/\lambda) - 2] - (p_1/p_{CJ})[(1/\lambda) - 1]; \quad 0 < \lambda < 1/2 \end{aligned} \quad (82)$$

Actually, it is physically more meaningful to use the similarity variable

$$\tau = 1/\lambda = t/t_g$$

where t_g is the time for the wave to reach the r where \hat{I} is to be determined. Then a consideration of Equation (82) makes it clear that

$$U(\tau) = \hat{I} + (p_1/p_{CJ})(\tau - 1) \quad (83)$$

is independent of the properties of the detonation, i.e., of γ_1 , γ_2 , C_2 , etc.

$U(\tau)$ is now considered to be the universal impulse function. $U(\tau)$ is tabulated below and is also plotted in Figure 12.

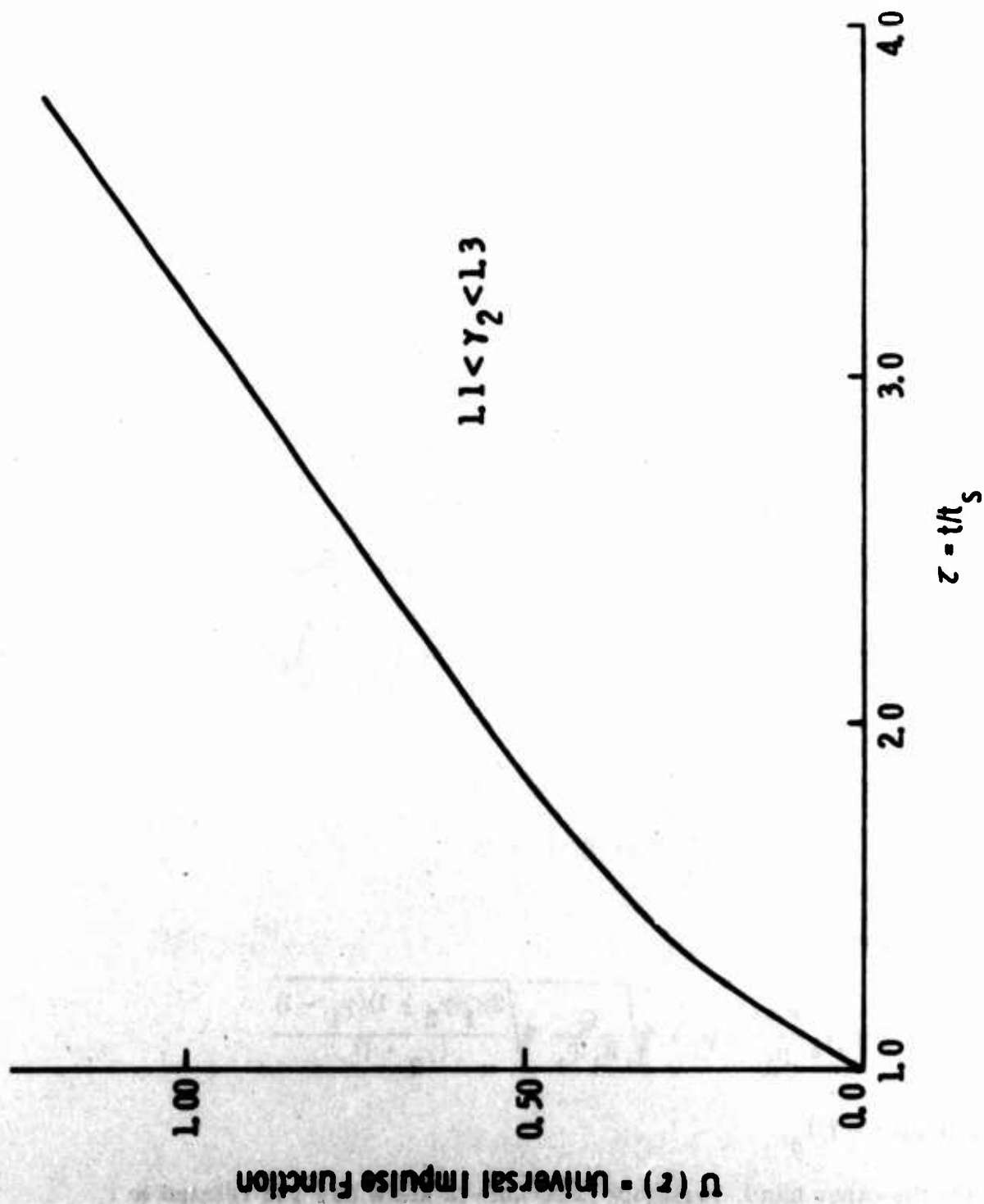


Figure 12. Universal Impulse Function

λ	τ	$U(\tau)$	λ	τ	$U(\tau)$
1.00	1.00	0.00	0.60	1.667	0.426
0.95	1.050	0.050	0.55	1.818	0.488
0.90	1.110	0.1003	0.50	2.00	0.556
0.85	1.178	0.152	0.40	2.50	0.740
0.80	1.250	0.203	0.30	3.33	1.046
0.75	1.330	0.256	0.20	5.00	1.659
0.70	1.429	0.310	0.10	10.00	3.500

In terms of $U(\tau)$

$$I = p_1 t_s \left[\frac{p_{CJ}}{p_1} U(\tau) - (\tau - 1) \right] \quad (84)$$

Several properties of I are now readily determined. Thus, since

$$t_s = \frac{r}{D} = \frac{r}{\sqrt{2(\gamma_2^2 - 1) Q}} \quad ; \quad \frac{p_{CJ}}{p_1} \approx 2\gamma_1 \left(\frac{\gamma_2 - 1}{\gamma_1 - 1} \right) Q$$

and

$$\frac{p_{CJ}}{p_1} U(\tau) \gg (\tau - 1)$$

it follows that

$$I \propto p_1 t_s \frac{p_{CJ}}{p_1} = p_1 r \sqrt{\frac{Q}{R_1 T_1}} \sqrt{\frac{2\gamma_1(\gamma_2 - 1)(\gamma_1 - 1)}{(\gamma_2 + 1)}}$$

for a fixed $\tau = t/t_s$.

On the other hand, it may be desirable to know how I is related to t , the actual time, rather than the dimensionless time τ . From Equation (82) it is clear that as $\tau \rightarrow \infty$ (or $t \gg t_s$)

$$\hat{I} = \left(0.358 - \frac{p_1}{p_{CJ}}\right) \tau$$

Therefore,

$$I = \left(\frac{p_{CJ}}{p_1}\right) p_1 \left(0.358 - \frac{p_1}{p_{CJ}}\right) t = 2\gamma_1 \frac{(\gamma_2 - 1)}{(\gamma_1 - 1)} \hat{Q} p_1 \left(0.358 - \frac{p_1}{p_{CJ}}\right) t \quad (85)$$

If $\hat{Q} \gg 1$,

$$I \propto 0.716 \frac{(\gamma_2 - 1)}{(\gamma_1 - 1)} \hat{Q} p_1 t \quad (86)$$

In the case of $H_2 + (1/2) O_2$

$$p_{CJ}/p_1 = 18.05 \quad ; \quad \text{therefore} \quad , \quad p_1/p_{CJ} = 0.0555$$

so that neglecting p_1/p_{CJ} in Equation (44) results in an error of the order of 15% in the evaluation of I .

Specific calculations of I as a function of time have been made for detonations in $H_2 + (1/2) O_2$ for $r = 0, 1, 2$, and 3 meters. The results are presented in Figure 13 below. It can be seen that, after an initial period representing the passage of the expansion wave, the impulse varies linearly with time. With increasing distance from the center of symmetry, the initial non-linear region broadens because of the broadening of the expansion wave with increasing time. The initial slope of the I - t curves is steeper than the final slope because immediately behind the wave $p = p_{CJ}$ but then drops to $p_2 < p_{CJ}$.

Knowing p_{CJ} , p_1 , and D curves of I for other detonable mixtures are readily computed using the universal impulse function $U(\tau)$.

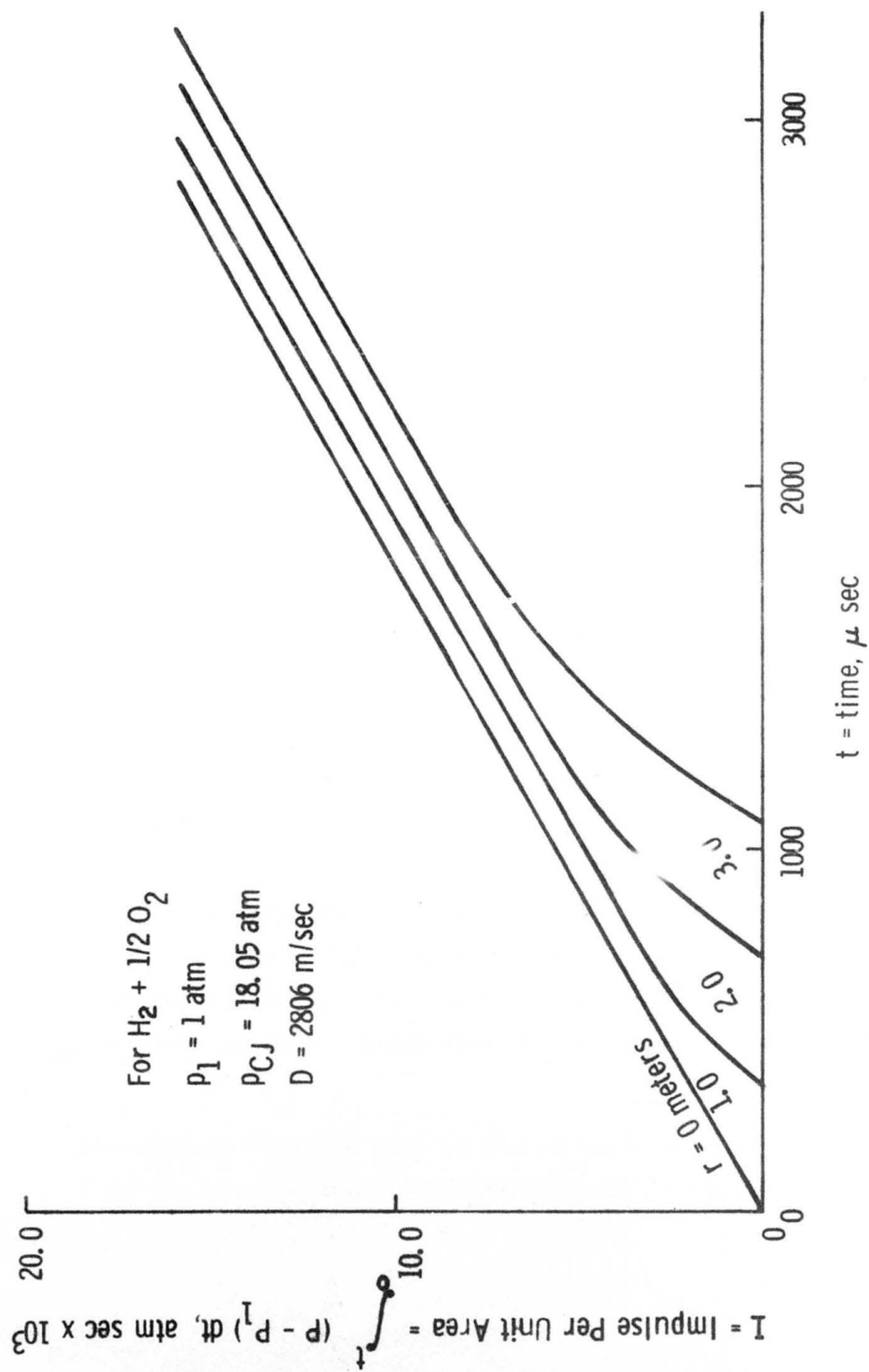
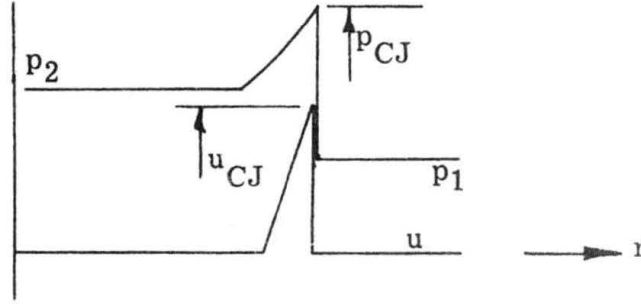


Figure 13. Variation of Impulse per Unit Area with Time

5. Dynamic Impulse at a Fixed Point - Spherical Detonations

As in the planar case, a spherical detonation is followed by an expansion wave within which the velocity of the fluid drops to zero and the pressure drops from p_{CJ} to some lower value p_2 . The variation of pressure p and velocity u behind a spherical C-J wave are shown qualitatively below:



As the wave moves outward, the width of this expansion wave increases.

Now the dynamic impulse

$$I_d = \int_0^t \frac{\rho u^2}{2} dt \quad (42)$$

is sought due to the passage of a spherical C-J detonation.

It can be shown that for a spherical C-J detonation u/u_{CJ} , and ρ/ρ_{CJ} are universal functions of $r/R = r/Dt = \lambda$ which depend only on the value of γ_2 , the ratio of specific heats downstream of the wave. In terms of the dimensionless variable λ , the dynamic impulse I_d then becomes

$$I_d = 0 \quad , \quad \lambda > 1 \quad , \quad \text{or} \quad t < t_s$$

$$I_d = \frac{\rho_{CJ} D^2 t_s}{2} \int_{\lambda}^1 \left(\frac{\rho}{\rho_{CJ}} \right) \left(\frac{u}{u_{CJ}} \right)^2 \frac{d\lambda}{\lambda^2} ;$$

$$\lambda_2 < \lambda < 1 \quad \text{or} \quad t_s < t < t_2 \quad (87)$$

At the end of the expansion wave $\lambda = \lambda_2$ and then

$$I_d = \frac{\rho_{CJ} D^2 t_s}{2} \int_{\lambda_2}^1 \left(\frac{\rho}{\rho_{CJ}} \right) \left(\frac{u}{u_{CJ}} \right)^2 \frac{d\lambda}{\lambda^2} = \text{const} \quad (88)$$

In the case of spherical symmetry, analytical solutions for (ρ/ρ_{CJ}) and (u/u_{CJ}) are not available; rather, these functions must be determined by numerical integration of the conservation equations.

The variation of (u/u_{CJ}) , (p/p_{CJ}) , a/a_{CJ} have been computed by Manson [see Taylor⁽¹¹⁾] for $C_2H_2 + O_2$ corresponding to $\gamma_2 = 1.13$ and by Sedov⁽⁶⁾ for $\gamma_2 = 1.67$. In Figures 14 and 15, p/p_{CJ} and u/u_{CJ} in the two cases are compared, and it can be seen that the results are quite insensitive to γ_2 . Hence, Manson's results will be used to evaluate the integrals in Equations (87) and (88).

First, Equations (87) and (88) will be written in a somewhat different form, i.e.,

$$I_d = \frac{\rho_{CJ} D^2}{\rho_1^2} \left(\frac{u_{CJ}}{D} \right)^2 \rho_1 t_s \int_{\lambda}^1 \frac{\rho}{\rho_{CJ}} \left(\frac{u}{u_{CJ}} \right)^2 \frac{d\lambda}{\lambda^2} \quad (89)$$

Now $\rho_{CJ} a_{CJ} = \rho_{CJ} (D - u_{CJ}) = \rho_1 D$

Therefore, $\frac{u_{CJ}}{D} = 1 - \frac{\rho_1}{\rho_{CJ}} = \frac{1}{\gamma_2 + 1}$

since $\rho_1/\rho_{CJ} = \gamma_2/(\gamma_2 + 1)$

Hence, we can also write

$$I_d = \frac{1}{2} \rho_1 D^2 \frac{1}{\gamma_2 (\gamma_2 + 1)} t_s U_s(\lambda) \quad ; \quad t_s < t < t_2$$

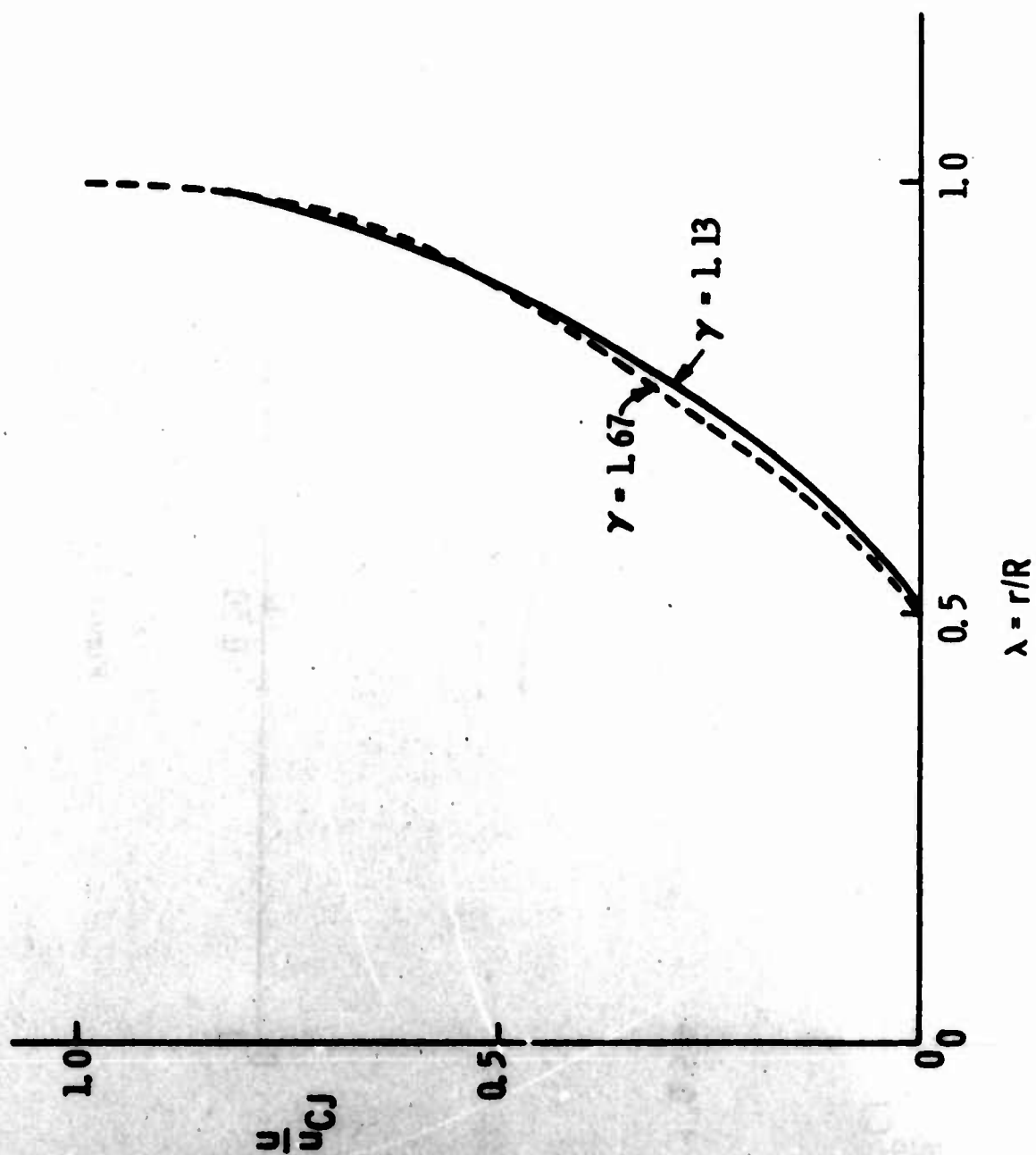


Figure 14. Variation of u/u_{CJ} with λ

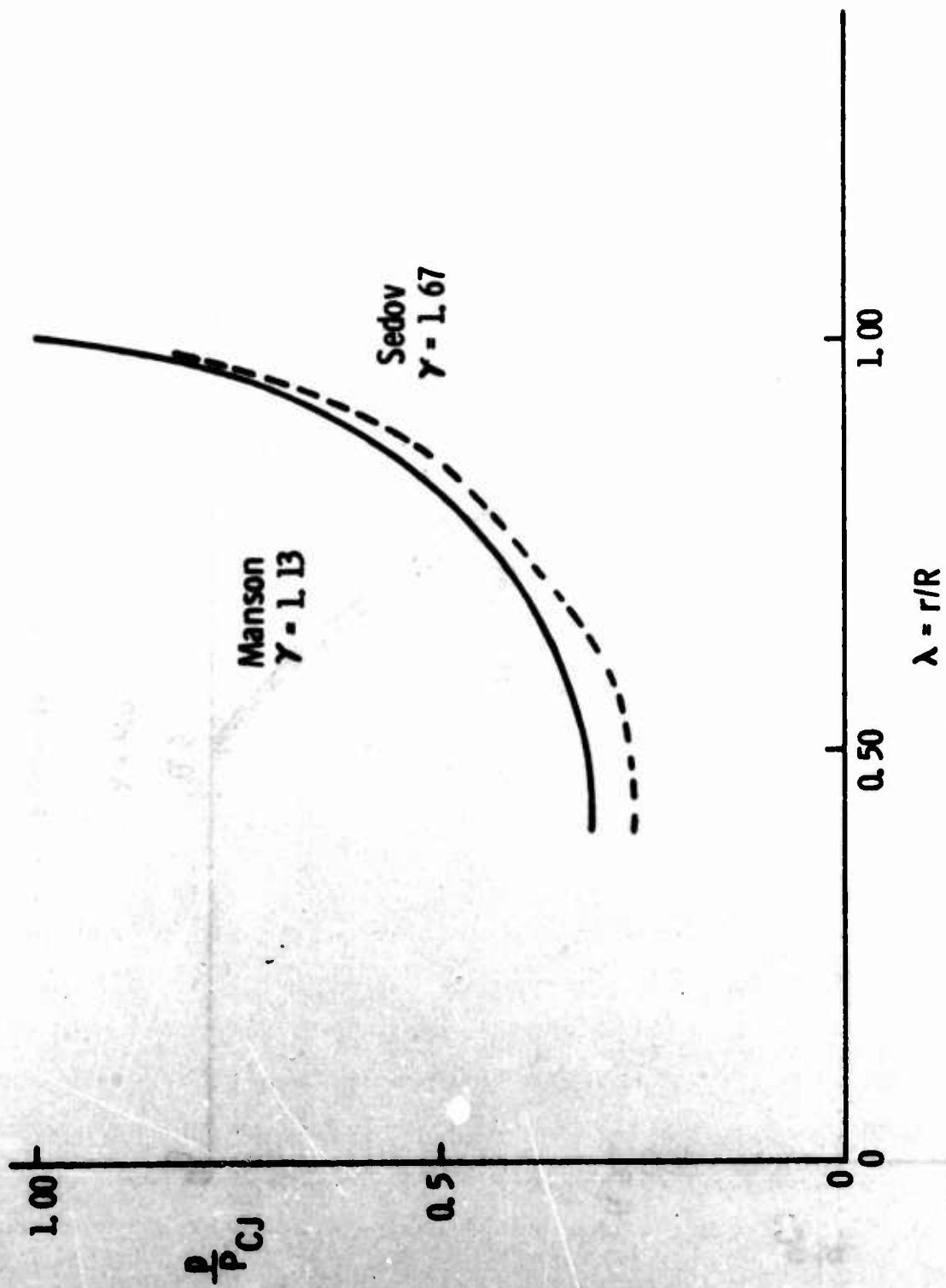


Figure 15. Variation of p/p_{CJ} with λ

where $U_s(\lambda) = U_s(\tau)$ is again a universal function defined by

$$U_s(\lambda) = \int_{\lambda}^1 \left(\frac{\rho}{\rho_{CJ}} \right) \left(\frac{u}{u_{CJ}} \right)^2 \frac{d\lambda}{\lambda^2} \quad (90)$$

and when $t > t_2$

$$I_d = \frac{1}{2} \rho_1 D^2 \frac{1}{\gamma_2 (\gamma_2 + 1)} t_s U_s(0.5) = \text{const}$$

since $\lambda_2 = 0.5$.

The universal function $U_s(\tau)$ has been evaluated and is shown in the tabulation below and has been plotted in Figure 16, for spherical detonations.

λ	U_s	τ	λ	U_s	τ
1.000	0	1.00	0.900	0.08836	1.111
0.990	0.01695	1.010	0.900	0.08836	1.111
0.980	0.02965	1.020	0.850	0.1053	1.178
0.970	0.04038	1.031	0.80	0.1183	1.250
0.960	0.04968	1.041	0.75	0.1268	1.331
0.950	0.05795	1.051	0.70	0.1318	1.430
0.940	0.06540	1.062	0.65	0.1345	1.539
0.930	0.07200	1.073	0.60	0.1359	1.667
0.920	0.07793	1.088	0.55	0.1360	1.819
0.910	0.08336	1.099	0.50	0.1362	2.000

I_d has been computed for $H_2 + (1/2) O_2$ at $r = 1m, 2m, 3m$ and is shown in Figure 17.

From Figure 17 it can be seen that the dynamic impulse increases to some final value after which it remains constant. This reflects the presence of a stagnant region about the center of symmetry. As r increases, the width of the expansion wave behind the detonation front increases; consequently, the total dynamic impulse increases, and this behavior is reflected in the graph (Figure 17).

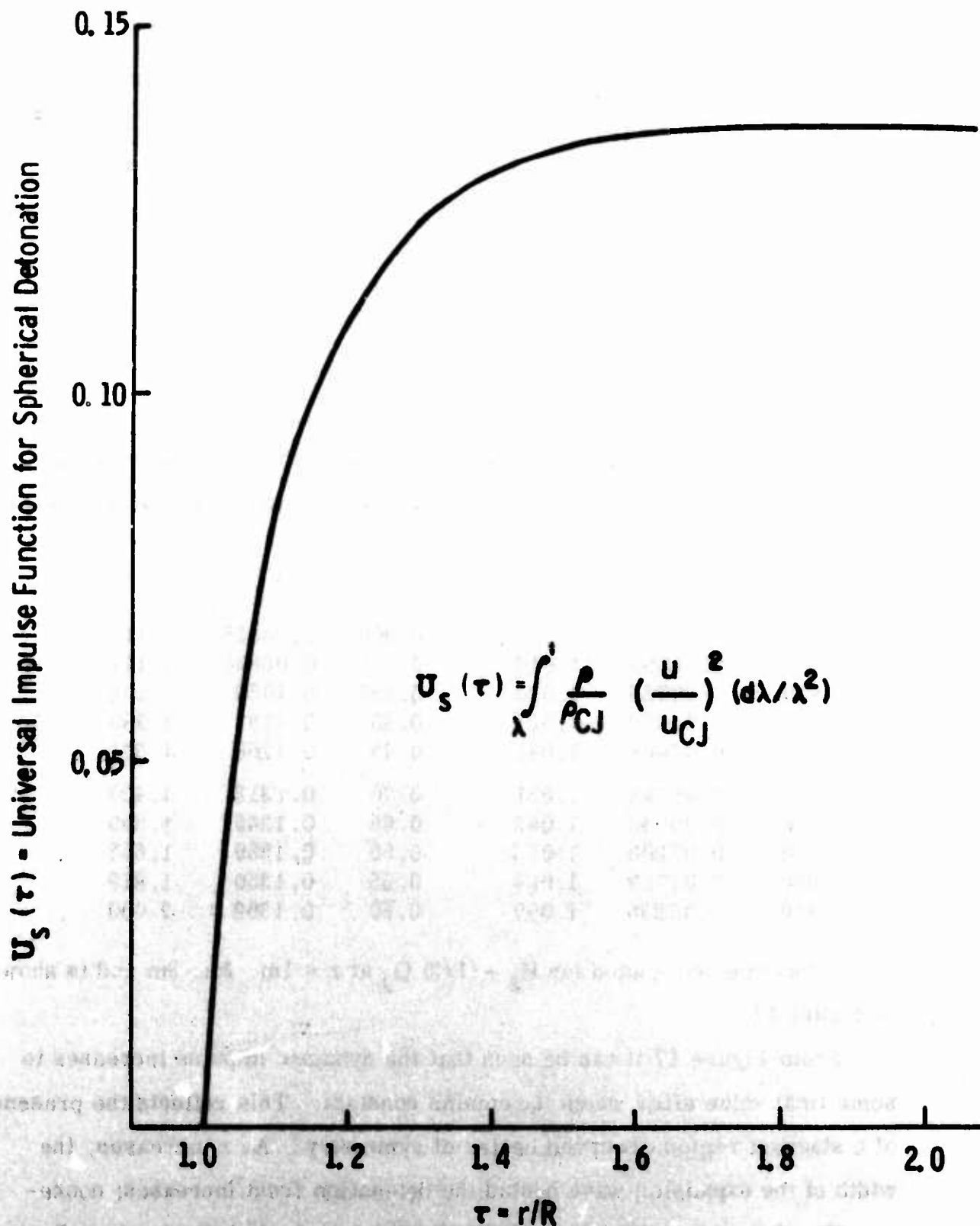


Figure 16. Universal Impulse Function $U_s(\tau)$ Spherical Detonation

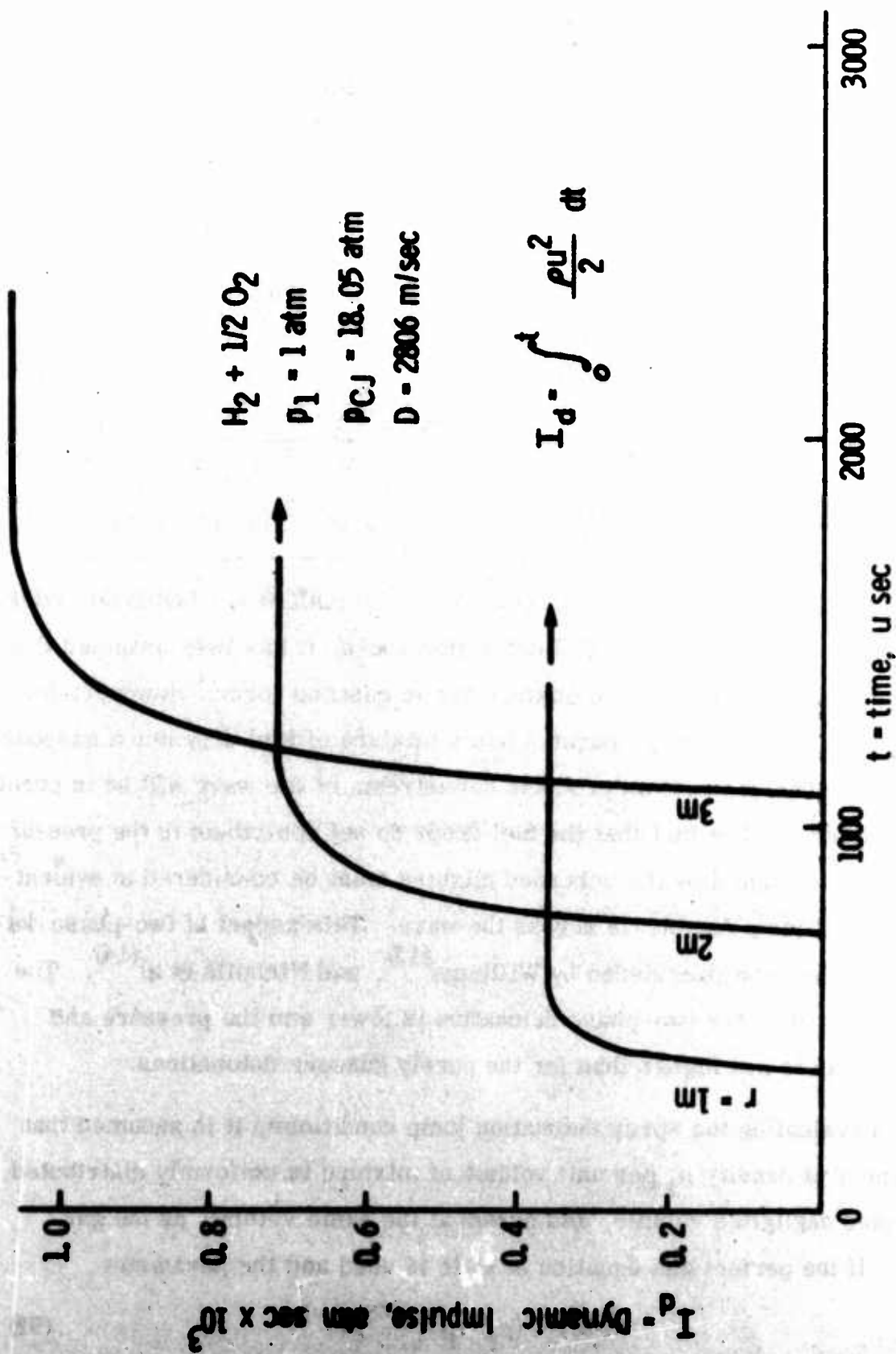


Figure 17. Variation of Dynamic Impulse per Unit Area

The variation of the final value of I_d is readily determined and is given by

$$I_{\text{final}} = \frac{1}{2} p_1 \gamma_1 M_D^2 \frac{1}{\gamma_2 (\gamma_2 + 1)} t_s U_s(\tau)_{\tau=2.0} \quad (91)$$

In the case of $H_2 + (1/2) O_2$

$$I_{\text{final}} = (7.35)(.136) r/D = 1.0 (r/D) \quad D = 2806 \text{ m/sec}$$

I_{final} for $H_2 + (1/2) O_2$ is tabulated below

$r(m)$	1	2	3	10	20	30	40	100
$I_{\text{final}} (\text{atm sec} \times 10^3)$	0.356	0.712	1.068	3.56	7.12	10.68	14.22	35.6

D. PROPAGATION OF C-J DETONATIONS THROUGH A CLOUD OF DROPS

In the discussion of the C-J detonation above, it has been assumed that both the burned and unburned mixture are in gaseous form. However, for the FAE the detonation propagates into a mixture of fuel drop and a gaseous oxidizer. The combustion products downstream of the wave will be in purely gaseous form. The fact that the fuel drops do not contribute to the pressure or volume occupied by the unburned mixture must be considered in evaluating the C-J jump conditions across the wave. This aspect of two-phase detonations has been considered by Williams⁽¹³⁾, and Nicholls et al⁽¹⁴⁾. The Mach number of the two-phase detonation is lower and the pressure and density ratios are higher than for the purely gaseous detonations.

In evaluating the spray detonation jump conditions, it is assumed that the spray of density ρ_f per unit volume of mixture is uniformly distributed, occupies negligible volume, and moves at the same velocity as the gas. Then, if the perfect gas equation of state is used and the parameter

$$\alpha = 1 + (\rho_f/\rho_1) \quad (92)$$

which is the mass of liquid and gas per unit mass of the gaseous component is introduced, the equations of mass, momentum, and energy conservation across the wave become

$$\alpha \rho_1 (v_1 - c) = \rho_2 (v_2 - c) \quad (93)$$

$$p_1 + \alpha \rho_1 (v_1 - c)^2 = p_2 + \rho_2 (v_2 - c)^2 \quad (94)$$

$$\frac{1}{\alpha} \frac{\gamma_1}{\gamma_1 - 1} \frac{p_1}{\rho_1} + \frac{1}{2} (v_1 - c)^2 + Q = \frac{\gamma_2}{\gamma_2 - 1} \frac{p_2}{\rho_2} + \frac{1}{2} (v_2 - c)^2 \quad (95)$$

The heat release Q is now defined as

$$Q = \bar{Q} + (\alpha - 1) e_l / \alpha$$

with \bar{Q} the heat released per unit mass of mixture due to chemical reaction and change of phase and with e_l the specific internal energy of the liquid.

The self similar C-J solution described in subsection D, above, will remain valid even for two-phase detonations. The presence of the liquid fuel will, however, modify the values of z_2 and V_2 and R_2 immediately downstream of the waves.

E. THE INITIATION PROBLEM

As mentioned above, the initiation of the detonation by the secondary blast is a crucial part of the FAE process. It is important to know how much blast energy is required to make a fuel cloud of a given shape and droplet density detonate. The answer to this question will require extensive experimentation; however, various theoretical aspects of the initiation problem are discussed here. Even in the case of gaseous detonations, there is, at present, no completely satisfactory theory to describe the blast initiation of a detonation wave. However, some of the analytical results which

have been obtained in the gaseous case should be applicable to the FAE initiation problem and, therefore, will first be discussed.

1. Blast Initiation of Gaseous Detonations

The problem of establishing what happens when a blast wave is set off in a combustible gas mixture has received the attention of a number of investigators. The current status of this problem is discussed in the reviews by Chernyi et al⁽²⁾ and Lee et al⁽⁵⁾, and in the articles by Bishimov et al⁽⁴⁾, Korobeinikov⁽³⁾, and Bach et al⁽⁷⁾. When combustion reactions are very rapid, the detonation front can be treated as an exothermic discontinuity. Then it can be shown that blast waves weaken with increasing radius and eventually change to a C-J detonation travelling at constant speed. In the planar, $\nu = 1$ case, this transition occurs only as $r \rightarrow \infty$; however, for cylindrical and spherical geometry the transition occurs at a finite value of the radius of the order of the critical radius r_* . The problem of blast initiation when the reaction rates and hence the detonation thickness are finite was considered by Bishimov et al⁽⁴⁾. The results of this analysis, together with experimental data, led Chernyi et al⁽²⁾ to conclude that:

" . . . with the limitations of the one dimensional flow model the initiation of an overdriven detonation wave by means of a piston (the role of which may be played by an expanding compressed gas), or by concentrated energy input, followed by the weakening of such waves, does not lead (in cases of practical interest) to their transition to the Chapman-Jouguet mode. "

Thus, with increasing radius the width of the reaction zone increases and the combustion zone becomes uncoupled from the leading shock wave.

Regardless of these theoretical results, blast waves do initiate detonations, and the key to this conflict between theory and experiment lies in the portion of the quotation above which has been underlined by the present

author. Most detonations do not have a one-dimensional structure; rather, there are transverse waves within the reaction zone which generate local hot spots and thus continually renew the combustion process [Strehlow⁽¹⁵⁾]. The blast initiation of detonations thus appears to be associated with instability of the leading shock front and the formation of a complex three-dimensional detonation structure.

A phenomenological theory which predicts the main features of blast initiation has been developed by Bach et al⁽⁷⁾. The key element of this theory is that the interaction between the combustion and the propagation of the blast wave is accounted for by treating the wave as an exothermic discontinuity with an effective heat release Q_e , which is only a fraction of the heat of reaction Q . Thus, Bach et al⁽⁷⁾ set

$$Q_e = Q \cdot F(\eta, z) \quad (96)$$

where

$$\eta = \frac{1}{M_s^2}, \quad z = \frac{r_s}{r_0} \quad (97)$$

and r_0 is a quantity called the explosion length which is defined by

$$r_0^\nu = \frac{E_0}{\rho_1 a_1^2 k_\nu} = \frac{\sigma_\nu}{\nu k_\nu} \frac{Q}{a_1^2} r_*^\nu \quad (98)$$

$$k_\nu = 1, 2\pi, 4\pi \quad \text{for} \quad \nu = 1, 2, 3$$

In general, r_0 is thus greater than the critical radius r_* . The choice of the function $F(\eta, z)$ is empirical and depends on the magnitude of z relative to $\delta = \Delta/r_0$, a dimensionless induction distance and on the magnitude of η relative to η_{CJ} , the Chapman-Jouguet value, and to η_0 , the critical value for auto-ignition behind the shock. In the theory the ignition delay or

induction distance Δ is chosen of the order of the ignition delay distance of a plane C-J detonation. To compute the propagation speed of the wave, the variation of velocity density and pressure behind the wave are a priori assumed to have the same form as previous analytical blast wave solutions.

A key result of the theory is that for a large ignition energy E_0 such that $\delta = (\Delta/r_0) \ll 1$ the blast wave monotonically decays to a C-J wave. When the ignition energy is small so that $\delta \gg 1$, the wave decays to an acoustic wave. Qualitatively, the theory reproduced the experimentally observed blast initiation of detonations. The critical energy E_0 for initiation is thus related to the ignition delay distance so that

$$(E_0)_{\text{crit}} \propto \rho_1 a_1^2 \Delta^\nu = \gamma_1 p_1 \Delta^\nu \quad (99)$$

The question now is whether a theory similar to that of Bach et al⁽⁷⁾ can be developed for the FAE. This problem is discussed qualitatively below.

2. Blast Initiation of Fuel Droplet Clouds

It is clear from the discussion above that, regardless of the theoretical model used, the ignition delay or induction distance Δ will play a central role. In the gaseous case Δ is governed by the chemical kinetics of the combustion reactions; however, in two-phase combustion the process by which the liquid fuel and the gaseous oxidizer are mixed plays the central role.

The ignition of single fuel droplets by an incident shock wave has been extensively investigated by Kauffman⁽¹⁶⁾, Kauffman et al⁽¹⁷⁾, Kauffman and Nicholls⁽¹⁸⁾, Ragland⁽¹⁹⁾, Ragland et al⁽²⁰⁾, and Dabora et al⁽²¹⁾. After the shock passes over the droplet a detached bow shock is formed ahead of the drop, the droplet flattens out, and a fine micromist is stripped from the droplet by the surface boundary layer induced by the flow over the drop.

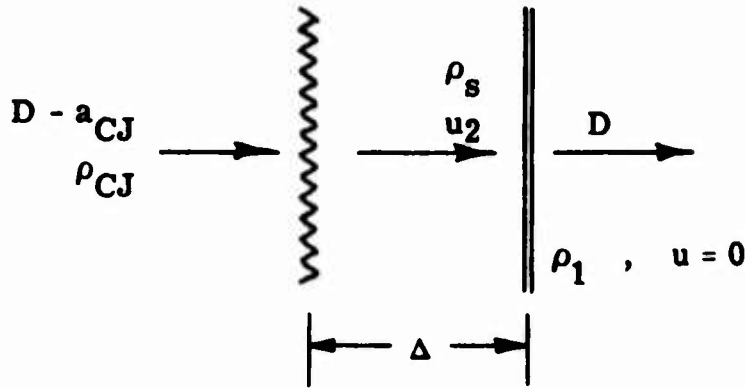
This micromist is entrained in the droplet wake, and the ignition process is characterized by an explosion of the fuel mist in the wake. Photographs of fuel droplets at various stages of ignition are presented by Kauffman et al⁽¹⁷⁾.

Unfortunately, no simple theory or correlation exists for the ignition delay time t_{ig} or the ignition delay distance Δ . In the case of both reacting and nonreacting drops it is possible to define a dimensionless droplet breakup time \bar{T}_b

$$\bar{T}_b = \frac{u_2}{d_o} \frac{\rho_2}{\rho_l} t_b \quad (100)$$

where u_2 is the velocity behind the shock, ρ_l is the density of the liquid fuel, d_o is the droplet diameter, and t_b is the droplet breakup time. This dimensionless breakup time was found to be approximately constant over the range of experimental conditions investigated by Kauffman et al⁽¹⁷⁾. For diethycyclohexane drops \bar{T}_b was found to lie in the range of 3.0 to 5.0. Further the droplet ignition delay time was found to be of the same order of magnitude as the value of \bar{T}_b may provide the basis for a first estimate of the ignition delay distance Δ for droplet clouds.

Bach et al⁽⁷⁾ chose Δ as the ignition delay distance behind a steadily propagating C-J detonation. If it is supposed that $t_b \sim t_{ig}$, then following Bach et al⁽⁷⁾ $\Delta \approx Dt_b$ where D is the C-J velocity. In the expression [Equation (100)] for t_b , u_2 is the velocity induced by the shock wave which precedes the reaction zone of the detonation front as pictured below, while ρ_2 will be equal to ρ_g , the density behind the shock.



From Equation (100) it now follows that

$$\Delta = \frac{D}{u_2} \bar{T}_b d_o \sqrt{\frac{\rho_l}{\rho_2}} \quad (101)$$

From the continuity equation across the shock wave

$$(D/u_2) = [1 - (\rho_1/\rho_2)]^{-1}$$

so that Equation (101) can also be written in the form

$$\Delta = [1 - (\rho_1/\rho_2)]^{-1} \bar{T}_b d_o \sqrt{\frac{\rho_l}{\rho_1}} \sqrt{\frac{\rho_1}{\rho_2}} \quad (102)$$

Combining Equations (102) and (99) then leads to the following expression for the critical initiation energy:

$$(E_o)_{crit} \propto \rho_1 a_1^2 \left[\frac{\bar{T}_b d_o \sqrt{(\rho_l/\rho_1)} \sqrt{\rho_1/\rho_2}}{1 - (\rho_1/\rho_2)} \right]^\nu \quad (103)$$

Thus, the critical initiation energy will, according to Equation (103), depend upon \bar{T}_b , an empirical constant, upon the droplet diameter d_o , upon the density of the gas ahead of the wave, on the sound speed ahead of the wave, or since $a_1^2 = \gamma_1 R_1 T_1$, upon the upstream temperature. Finally, $(E_o)_{crit}$ depends on the shock density ratio ρ_2/ρ_1 and on the density of the liquid fuel. The influence of the detonation Mach number, M_D enters through

its influence on ρ_2/ρ_1 since the shock density ratio is given by

$$\frac{\rho_2}{\rho_1} = \frac{\gamma_1 + 1}{\gamma_1 - 1} \left/ \left[1 + \frac{2}{(\gamma_1 - 1) M_D^2} \right] \right. \quad (104)$$

The validity of Equation (103) should be tested experimentally.

There are also certain geometrical considerations which enter in a consideration of FAE initiation. In the usual initiation analysis it is presumed that the geometry of the initiating blast and final detonations are the same; however, this is not necessarily true. If a point charge is used to detonate a cylindrical fuel cloud the initiating blast will be spherical, as shown in Figure 18 below.

Transverse waves appear to play an important role in the initiation of gaseous detonations as discussed above, although a theory of initiation which includes the effect of these waves is not yet available. The theory of Bach et al⁽⁷⁾ only accounts for the interaction between the combustion and the initiating blast in a global way. The detonation of two-phase fuel-oxidizer mixtures always appears to be accompanied by secondary shocks or blast waves within the reaction zone, and an explosion or blast wave appears to be an essential feature of the shock ignition of fuel droplets. These droplet wake explosions should, in addition to transverse waves, also play an important role in the initiation process, for the blast wave emanating from the droplet wake provides a mechanism of interaction between the droplet combustion and the initiating blast. It may be necessary to incorporate the effect of these droplet explosions in the theory of FAE initiation.

It should be possible to develop at least a phenomenological theory of FAE initiation. Such a theory will depend in a crucial way on the proper description of fuel droplet ignition.

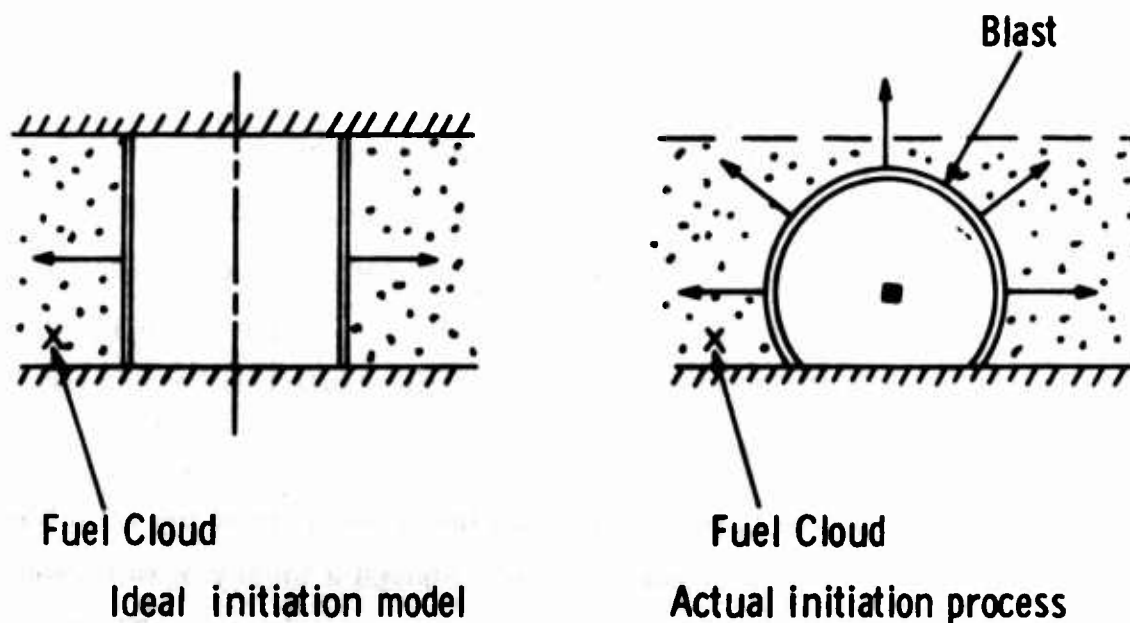


Figure 18. Initiation Process - Ideal Versus Actual

F. DEVIATIONS FROM THE IDEAL CYLINDRICAL BLAST MODEL

Most of the foregoing analysis and discussion is based on the idealized model of the FAE consisting of a cylindrical blast and detonation through a monodisperse and uniform fuel cloud. Deviations from this ideal model will now be considered qualitatively.

1. Nonuniform Distribution of Fuel Drop

It is highly probable that the blast dissemination of the liquid fuel will not result in uniform cloud of fuel droplets. Rather, the drop density and hence the heat release Q per unit mass of fuel oxidizer mixture will be a function of radius. Then the self similar C-J wave discussed above will no longer be the limiting behavior at large time, i.e., as $t \rightarrow \infty$.

However, self similar solutions are also available when $Q = Q(r)$ and should be a valuable aid in studying the effect of nonuniform fuel distribution. For instance, suppose that Q varies with radius according to

$$Q = B/r^\omega \quad (105)$$

Then the characteristic parameters of the C-J wave problem are ρ_1 , p_1 , B , r , t , and γ . When $\omega \neq 0$, there are no combinations of the dimensions of ρ_1 and p_1 having the dimensions of the proportionality constant B . Consequently, all of the characteristic parameters above are dimensionally independent; hence, no self similar solution for the C-J detonation exists, in general, when Q varies with r . However, if the pressure ratio across the detonation is large so that p_1 can be neglected, a self similar solution can be found. Then only a single π product can be formed from the characteristic parameters and leads to the similarity variable

$$\lambda = \beta r/B^{1/2+\omega} t^{2/2+\omega} \quad (106)$$

where β is again an arbitrary constant. Upon choosing the similarity variable λ as unity on the detonation front

$$r_s = B^{1/2+\omega} t^{2/2+\omega} / \beta \quad (107)$$

and

$$c = \frac{dr_s}{dt} = \frac{2}{2+\omega} \frac{r_s}{t} = \left(\frac{2}{2+\omega}\right) B^{1/2+\omega} / t^{\omega/2+\omega} \beta \quad (108)$$

Thus, r_s does not increase as rapidly with t than when $\omega = 0$ and the velocity of propagation c decreases with increasing time.

A wide variety of self similar solutions for variable Q , and ρ_1 are also discussed by Bishimov et al⁽²²⁾, and the study of such solutions should provide considerable insight to the effects of nonuniformities on FAE behavior.

2. The Effect of Side Relief

Even if a uniform cylindrical fuel cloud can be established, the upper surface of the cloud will be bounded by the inert atmosphere rather than by the confining surface of the ideal model. As the detonation passes such an inert boundary, a shock is propagated into the inert gas and an expansion usually propagates into the combustion products [Sichel⁽²³⁾, Dabora et al⁽²⁴⁾]. The presence of the inert boundary causes the detonation wave to become curved and results in a reduction in the velocity of propagation.

A sectional view of the possible form of a cylindrical wave with side relief is shown in Figure 19 below.

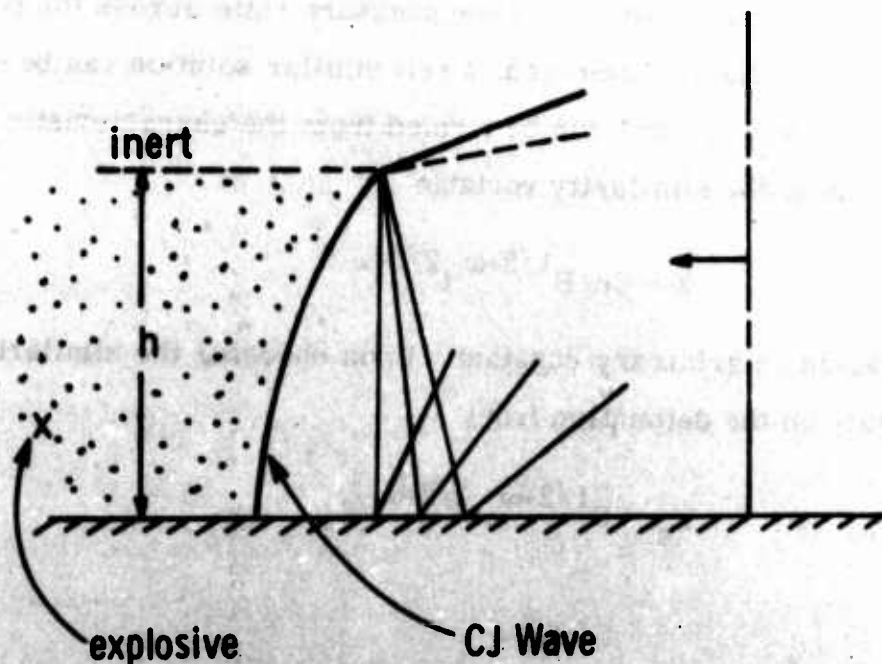


Figure 19. Chapman-Jouguet Wave with Side Relief

Plane detonations with side relief have been investigated by Sichel⁽²³⁾, Dabora et al⁽²⁴⁾, and Tsuge et al⁽²⁵⁾. The author is not aware of any work dealing with the influence of side relief on cylindrical diverging waves. The extent to which the inert boundary influences the propagation of the detonation is dependent, to a large degree, on the ratio of the ignition delay distance or reaction zone length Δ to the width, h of the explosive, i.e., on (Δ/h) , as well as on the properties of the inert boundary. An important effect of the inert compressible boundary is that the detonation will fail to propagate when (Δ/h) exceeds a certain critical value. Clearly, the presence of inert compressible boundaries will have an important effect on the FAE propagation.

3. Propagation Beyond the Fuel Cloud Boundary

Even in the ideal cylindrical model, a shock will propagate into the region beyond the fuel cloud, i.e., for $r > r_c$. This shock will also contribute to the total ground impulse provided by the FAE and must be taken into account. As the detonation reaches the edge of the fuel cloud, a shock will be propagated into the inert region $r > r_c$ and either an expansion or shock will propagate back into the burned gas, as shown in Figure 20. Beyond the edge of the fuel cloud, $r > r_c$, the transmitted shock will gradually decay to an acoustic wave. It is questionable whether a self similar solution can be used to describe the propagation of the transmitted wave into inert gas beyond the fuel cloud. The problem of the transmitted wave has been considered by Kiwan⁽²⁶⁾ who used a numerical scheme to compute the propagation of the wave into the region beyond the fuel cloud.

4. Drop Size Distribution

In the ideal FAE model it is assumed that the droplets are uniformly distributed in the fuel cloud and that all fuel droplets have the same diameter. In the actual fuel clouds the droplet diameters will be distributed over a wide range of diameters. The smaller droplets will ignite more

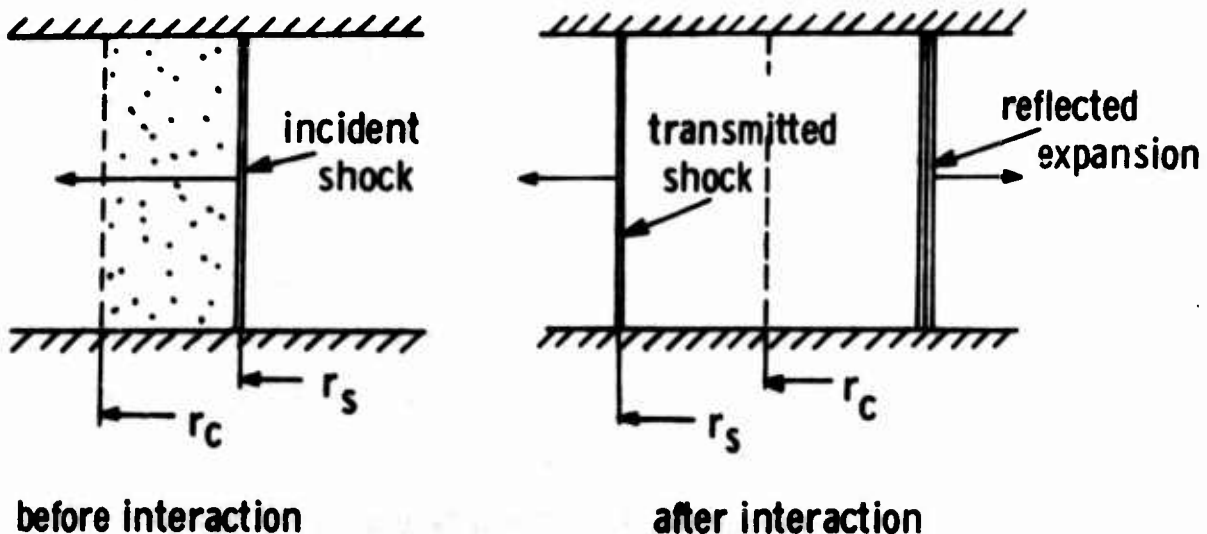


Figure 20. Shock Interaction with Fuel Cloud Boundary

rapidly than the large droplets and no doubt will influence the ignition of the larger droplets. The ignition properties of droplets with a bimodal size distribution are currently being investigated by Pierce⁽²⁷⁾. From his results it appears that the presence of different sized droplets can have an important effect on the ignition and detonation processes.

G. COMPUTATION OF C-J DETONATION VELOCITIES FOR COMPLEX HYDRO-CARBON FUELS

In order to analyze FAE propagation in detail, it is necessary to accurately compute the C-J velocities for complex hydrocarbon-air mixtures. Generally, such computations are tedious and time-consuming. However, the National Aeronautics and Space Administration has, over the past ten years, developed a computer program which very rapidly carries out such computations for gaseous detonations. This program has been adapted to the University of Michigan Computing Center and is currently being used to compute detonation velocities through various MAPP gas-air mixtures.

It is planned to modify the program to compute detonations through droplet clouds. The features of the NASA program are described in detail below.

The NASA publication SP-273 ⁽²⁸⁾ describes the existing program which calculates (1) complex chemical equilibrium compositions for assigned thermodynamic states, (2) rocket performance, (3) incident and reflected shocks, and (4) Chapman-Jouguet detonations. It was found to be very desirable to have parts (1) and (4) for use here.

The basic approach for part (1) is as follows: Chemical equilibrium is usually described by either of two equivalent formulations; equilibrium constants or minimization of free energy. The program authors found the free-energy minimization to be the better of the two in terms of storage and computer time; hence this approach is used.

The condition for equilibrium may be stated in terms of any of several thermodynamic functions such as the minimization of Gibbs free energy or Helmholtz free energy or the maximization of entropy. If one wishes to use temperature and pressure to characterize the final thermodynamic state, the Gibbs free energy is most easily minimized inasmuch as temperature and volume (or density).

The program assumes all gases are ideal and that interactions between phases are neglected.

The method used for obtaining Chapman-Jouguet detonation parameters uses three steps. The first step consists of obtaining an initial estimate of the detonation pressure and temperature. The second step is an improved estimate of these parameters by means of a recursion formula. The third step consists of obtaining the correct values by means of a Newton-Raphson iteration procedure. The standard conservation equations for continuity

momentum and energy apply with the additional constraint that the burned gas velocity is sonic in the Chapman-Jouguet plane.

The program had to be modified since it was originally written for use on an IBM 7090 computer under a standard IBM operating system. [The University of Michigan uses an operating system called MTS (Michigan Terminal System) and IBM 360/67 computers.] The modifications to the program have been completed, and the C-J velocities in MAPP-air mixtures are currently being computed.

H. CONCLUSIONS—THEORETICAL ANALYSIS

Initially the FAE behaves like a strong blast wave; then after a period of transition, the FAE tends toward the behavior of a C-J wave. Although a completely detailed description of the FAE will require lengthy numerical integration of the conservation equations, the discussion above indicates that much useful information can be gained, with minimal computational effort, from a consideration of the well-known self similar blast wave and C-J solutions. For many considerations it may be sufficient to model fuel air explosions by a self similar blast wave for $r_g < r_*$ followed by a C-J wave for $r_g > r_*$.

The ignition delay distance plays a key role both in the initiation process and in establishing the influence of side relief. In the FAE this distance will be mainly governed by the fuel droplet breakup and ignition process rather than by reaction rates as in the gaseous case.

SECTION III

EXPERIMENTAL RESEARCH

A. INTRODUCTION

The purpose of this phase of research has been to conduct controlled experiments on the cylindrical propagation of two-phase detonation. Heretofore, controlled experiments have never been conducted on the cylindrical or spherical propagation of such explosions wherein fuel-air mixture ratio and/or drop sizes are controlled. Since such conditions are important in fuel-air explosions, an estimate of their influence is desirable. In order to increase the confidence of the theoretical estimates, experiments were performed on a scaled-down model of a fuel-air explosion in the laboratory. A cylindrically shaped cloud was modeled which is idealized to the extent that cloud conditions (i. e. , mean drop size and local mixture ratio) vary only with radius rather than with azimuth or in a direction parallel to the axis. Due to the axial symmetry of the problem and in order to minimize the magnitude of the explosion, the test chamber configuration chosen is a pie-shaped segment of a cylindrical cloud (Figure 21).

B. DESIGN OF THE EXPERIMENTAL FACILITY

1. Selection of Test Chamber Dimensions and Fuel Drop Size

The walls of a detonation test chamber will, in general, have some effect on the detonation process due to heat and momentum losses to the wall. While a very large chamber will essentially eliminate the wall effects on the overall process, if a test chamber is to be operated within a laboratory, it is important that the chamber not be excessively large.

Two-phase detonation studies in constant area test chambers⁽²¹⁾ have demonstrated that there is a relation between fuel drop size, test chamber dimensions, and the magnitude of the wall effects on the detonation process.

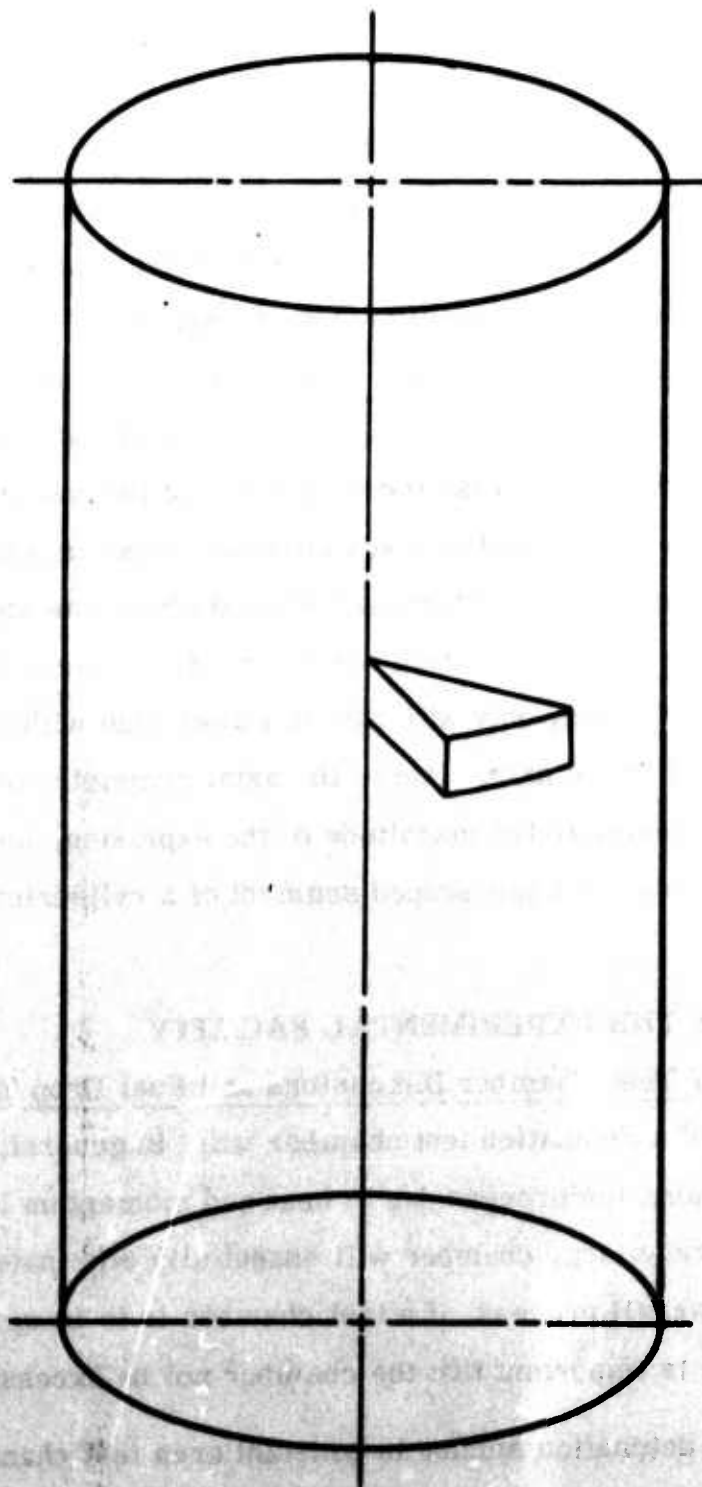


Figure 21. Experimental Model Relative to Cylindrical Cloud

Therefore, in the process of determining the dimensions of a test chamber which will minimize wall effects and still be of a practical size and shape, it is necessary to simultaneously consider the size of the fuel drops.

The selection of the size and distribution of the fuel drops within the test chamber must also be based on the practical limitations of the drop-producing mechanism and the fuel-to-air ratio desired.

The mass of liquid fuel per unit volume of air, m_f , is given by

$$m_f = N(\pi/6) D^3 \rho_f \quad (109)$$

where N = number of drops per unit volume of air

D = drop diameter

ρ_f = density of liquid fuel

The mass of the air per unit volume may then be given by

$$m_a = [1 - N(\pi/6) D^3] \rho_a \quad (110)$$

Neglecting the volume of the droplet compared to that of the control volume and neglecting evaporation of fuel, the fuel/air mixture ratio from Equations (109) and (110) becomes

$$m_f/m_a = N(\pi/6) D^3 \rho_f/\rho_a \quad (111)$$

The mixture ratio, by weight, is equivalent to the product of the fuel/air mole fraction, η , times the ratio of their molecular weights, M_f/M_a .

This is expressed as

$$m_f/m_a = \eta(M_f/M_a) = n\phi(M_f/M_a) \quad (112)$$

Here n is the stoichiometric mole fraction and ϕ the equivalence ratio.

Equating (111) and (112) and solving for N gives

$$N = \frac{6}{\pi D^3} [n\phi(\rho_a/\rho_f)(M_f/M_a)] \quad (113)$$

The fuel selected for this experimental work was kerosene because of its relatively low vapor pressure, reasonably good other physical characteristics, and its availability. For kerosene drops in theoretical air at standard conditions, we have from Equation (113) the result

$$N = 1.98 \times 10^{-4} (\phi/D^3) \quad (114)$$

where drop size D is given in centimeters.

The distribution of fuel drops could be rather simply determined by Equation (114) if the drops were equally spread in all directions. However, with the hypodermic needle technique of producing fuel drops, which was contemplated for this work, the vertical distance between the drops is necessarily relatively short. It is necessary for the horizontal spacing to be appreciably greater than the vertical spacing if very rich fuel/air mixtures are to be avoided.

The rectangular volume element which surrounds and is apportioned to each fuel drop is defined as the product of the sides of the element.

Thus

$$S_x \cdot S_y \cdot S_z = V = \text{volume of element/fuel drop} \quad (115)$$

and

$$V = 1/N$$

The arrangement of a volume element within the test chamber configuration planned is shown by Figure 22. The magnitude of S_x , S_y , and S_z are not, in general, equal, but the following relations can be assumed:

$$S_x = a S_z \quad (116)$$

$$S_y = b S_z$$

Using Equation (115), the number of drops/unit volume can be expressed by

$$N = \frac{1}{S_x S_y S_z} = \frac{1}{a b S_z^3} \quad (117)$$

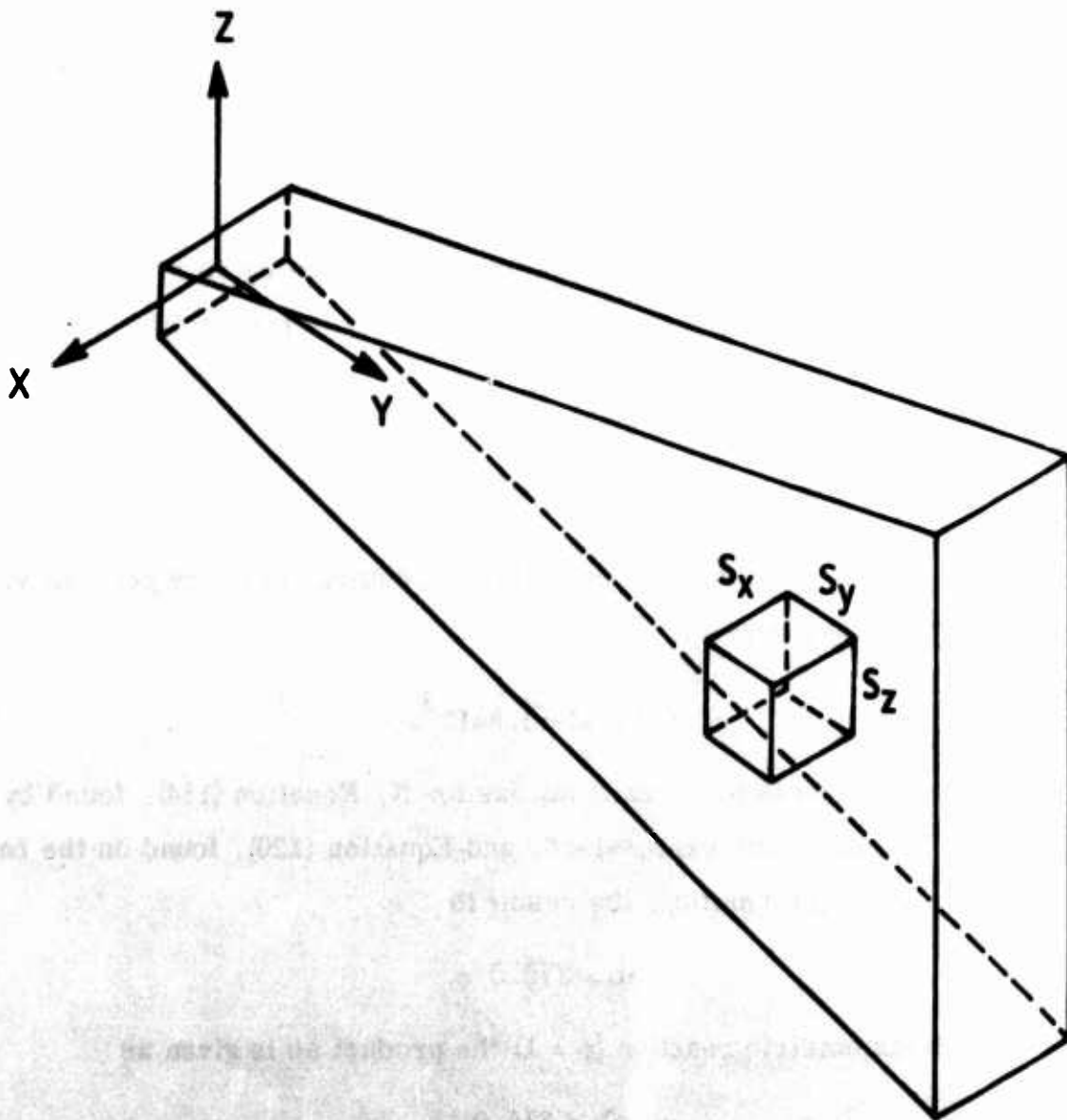


Figure 22. Reference Frame used to Establish Experiment Scale

In order to arrive at practical values for a and b in Equation (117), the mechanism of drop formation must be considered. The drop-generating technique under consideration involves the breakup of a stream of liquid fuel from a small tube. Although such small jets will generally break up due to instabilities, the breakup would normally be rather irregular unless special conditions exist. If the liquid jet is disturbed at the frequency at which it is most unstable, the Rayleigh disturbance frequency, the jet will break up and form quite uniformly sized drops. At such a disturbance frequency the wavelength, λ , is given as a function of drop diameter by

$$\lambda/D = 2.38 \quad (118)$$

Tests show λ compares approximately with the vertical drop spacing, S_z if, as assumed here, the terminal drop velocity is equal to the liquid jet velocity. The drop size may then be related to vertical drop spacing through

$$S_z/D \approx 2.38 \quad (119)$$

Using Equation (117) in Equation (119), the number of drops per unit volume is related to drop size by

$$N \approx 1/ab (2.38D)^3 \quad (120)$$

Equating the results of the calculations for N , Equation (114), found by relating mixture ratio expressions, and Equation (120), found on the basis of optimum drop formation, the result is

$$ab = 375.0/\phi \quad (121)$$

For a stoichiometric reaction ($\phi = 1$) the product ab is given as

$$ab = 375.0 \quad (122)$$

It follows that the drop spacing dimensions of Equation (116) may be arrived at by selecting a desired drop size and choosing values for the constants a and b, subject to Equation (122). For a given drop diameter, the vertical dimension is found using Equation (119); then using the result, Equations (122) and (116), the x and y dimensions can easily be found.

The nominal drop size was selected following an examination of the frictional and heat losses to the walls of a prospective test chamber and the reaction zone length of a detonation process. The wall losses may be taken into account through the use of the Equation (123)⁽²¹⁾, where u_s is the actual detonation velocity, u_{so} the ideal C-J velocity, γ_3 the ratio of specific heats at the Chapman-Jouguet plane, ρ_f the fuel density, ρ_1 the oxidizer density in front of the shock wave, C_H the heat transfer coefficient, and r_h the hydraulic radius.

$$u_s/u_{so} = [1 + (30D/r_h) \gamma_3^2 (\rho_f/\rho_1)^{1/2} C_H]^{-1/2} \quad (123)$$

The product in the brackets is small compared to one, allowing $(u_{so} - u_s)/u_{so}$, the dimensionless velocity deficit to be expressed by the binomial expansion

$$\Delta u_s/u_{so} = 1 - (u_s/u_{so}) \approx 15D/r_h (\gamma_3^2 C_H (\rho_f/\rho_1))^{1/2} \quad (124)$$

For $\gamma_3 = 1.2$, $C_H = 2.5 \times 10^{-3}$ and the appropriate densities, Equation (124) becomes

$$\Delta u_s/u_{so} \approx 5.5 \times 10^{-5} (D/r_h) \quad (125)$$

for D in microns and r_h in inches. Equation (124) is plotted in Figure 23. Hydraulic radius, defined as 2x crosssectional area/perimeter, may be expressed as a function of test chamber geometry through (see Figure 24),

$$r_h = 2 \tan(\theta/2) / [(1/r) + (2/h) \tan(\theta/2)] \quad (126)$$

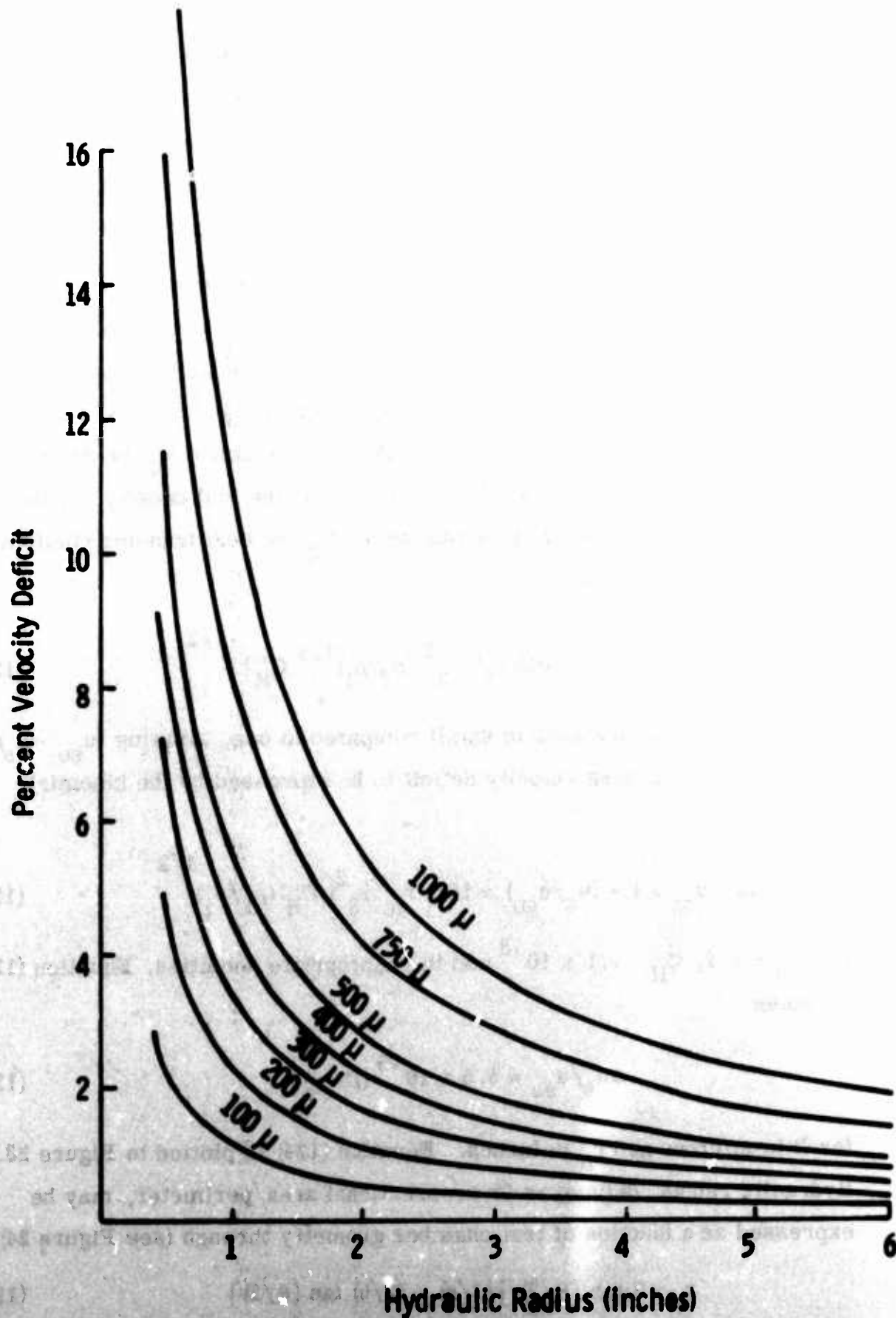


Figure 23. Velocity Deficit Plotted Versus Hydraulic Radius for Constant Drop Size

The velocity deficit of Equation (125) using Equation (126) can then be expressed as a function of drop diameter and test chamber geometry. The resulting expression was examined, and plots similar to Figure 25 were made for various chamber configurations. For a selected chamber geometry, this figure gives chamber radial distance versus drop diameter for curves of constant velocity deficit. As expected, the velocity deficit becomes very large in the chamber vertex region. It was decided that conditions should be selected which would allow the flow properties to be well established, with few wall losses, by a radial distance of 6 inches. Hence, a practical chamber geometry was selected on the basis of a tolerable velocity deficit.

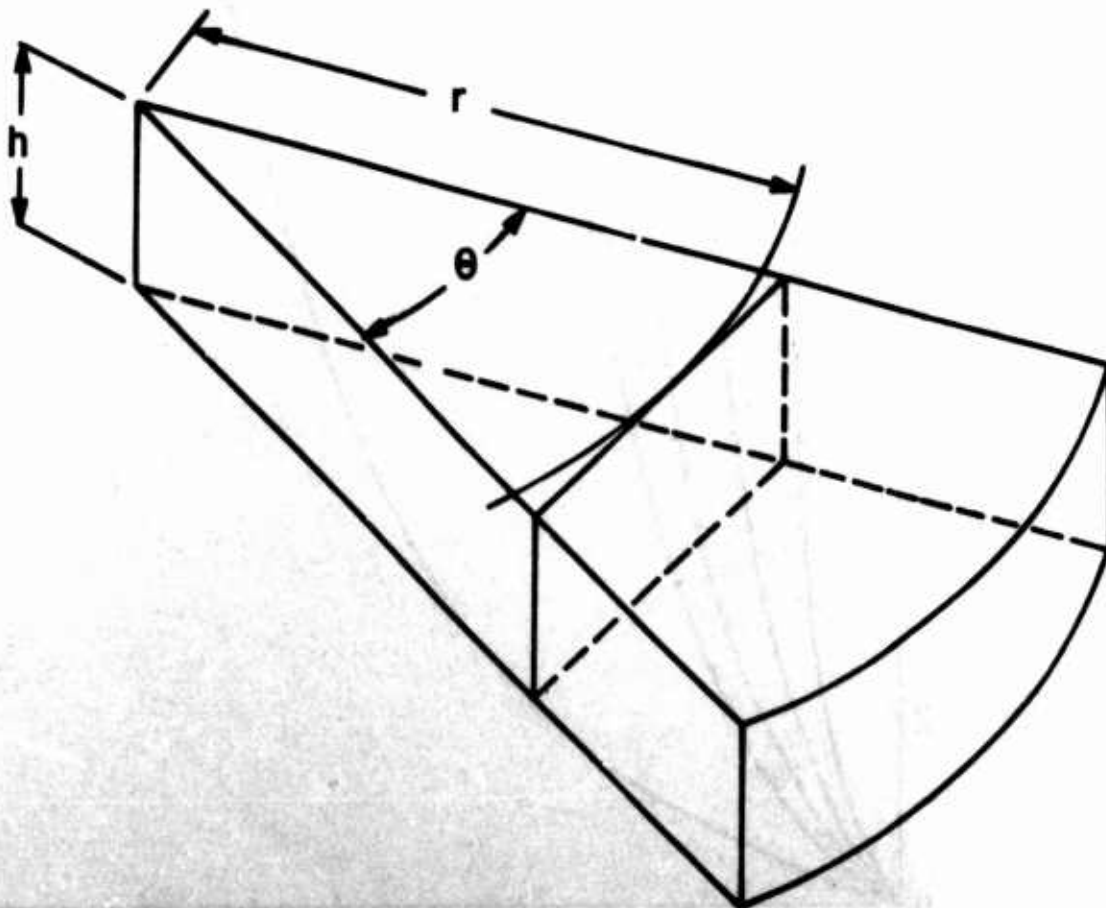


Figure 24. Reference used to Express Hydraulic Radius in Terms of Chamber Geometry

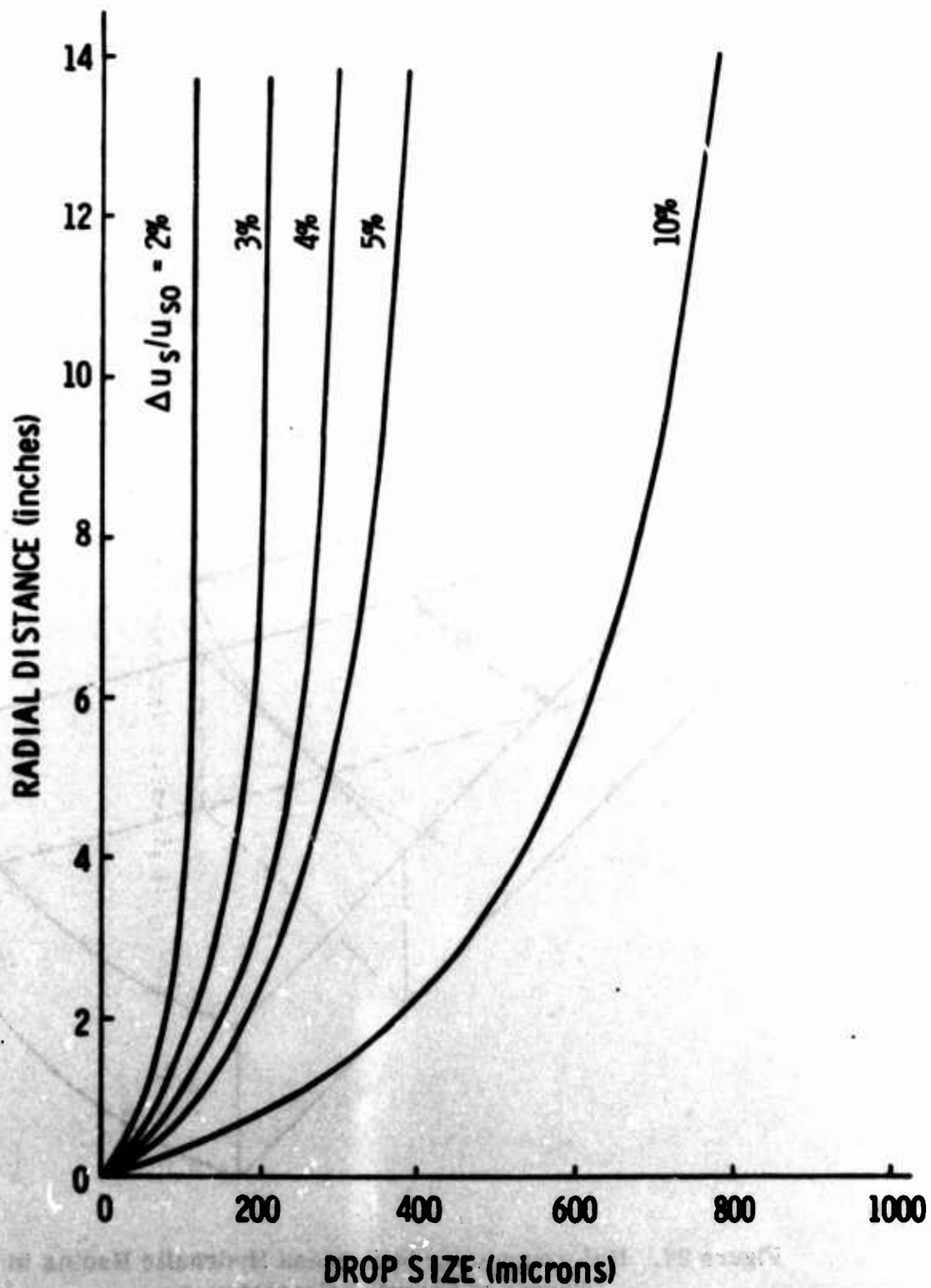


Figure 25. Radial Distance Plotted Versus Drop Size for Constant Velocity Deficit

The nominal drop size was established by considering the detonation reaction zone lengths as a function of drop size in conjunction with the above mentioned figures. It had previously been concluded²⁰ that the reaction zone length for two-phase detonations is controlled by the drop breakup time. Breakup time, t_b , of inert drops by shock waves can be related to the dynamic pressure of the convective flow behind the shock and the initial drop diameter D as follows⁽²¹⁾:

$$t_b/D = k [\rho_l/(\rho_2 u_2^2)]^{1/2} \quad (127)$$

where k is approximately equal to 5 and ρ_l is the liquid density, and ρ_2 and u_2 are the convective flow density and velocity. A better estimate of actual drop breakup time in a detonation is achieved if an average dynamic pressure is used. Since dynamic pressure in a convective flow behind a C-J plane is less than 10 per cent of that behind a shock traveling at the same Mach number, for $M > 3$ an average dynamic pressure equal to one-half that used in Equation (127), can then be used. Then Equation (127) becomes

$$t_b/D = 1.41k (\rho_l/\rho_1)^{1/2} (\rho_1/\rho_2)^{1/2} (1/u_2) \quad (128)$$

In terms of shock velocity we have

$$\bar{X}_b \equiv t_b u_s / D = 1.41k (\rho_l/\rho_1)^{1/2} (\rho_1/\rho_2)^{1/2} [1 - (\rho_1/\rho_2)]^{-1} \quad (129)$$

Equation (129) gives $\bar{X}_b = 162$ for $M = 3$ and decreases to 120 for M becoming infinitely large. For this case then Equation (129) becomes

$$\bar{X}_b \equiv t_b u_s / D = \bar{x}/D \approx 162 \quad (130)$$

In order to have a smoothly propagating detonation wave, the drop spacing S_y (Figure 22) must be of the order of the reaction zone length \bar{x} given in Equation (130). Thus, Equation (130) becomes

$$S_y \leq 162D \quad (131)$$

The final selection of the nominal fuel drop size and the test chamber dimensions were made on the basis of allowable limits on velocity deficit and the practical problems of drop generation. By examining a series of graphs similar to Figure 25 and by considering that the allowable limit on the velocity deficit at a six-inch radial distance should be about 5 per cent, a nominal drop size of less than 400 microns was obtained. By orienting the pie-segment shaped test chamber as shown in Figure 22 and injecting the fuel drops through the top surface, the vertical separation between the drops is S_z . As a practical matter, the needle positions were chosen so that groups of fuel injection needles would be installed in the top of the chamber along lines parallel to the x axis (Figure 22). The separation between the individual needles in each of these rows is S_x while the (projected) separation between each row of needles is S_y .

The value of S_z is essentially fixed by the choice of drop size, according to Equation (119). The value of S_y is limited by Equation (131). Combining values of S_z and S_y with Equations (116) and (122) results in a value for S_x . The drop spacings finally arrived at were

$$S_x = 0.64 \text{ cm} \quad ; \quad S_y = 5.4 \text{ cm} \quad ; \quad S_z = 0.095 \text{ cm}$$

Since the chamber is essentially 2 inches wide, an x-separation of 0.64 cm results in seven needles per row. It was decided that an overall chamber length of about 30 inches would be suitable for this research. Therefore, eleven rows of needles with a y-separation of 5.4 cm were required, or a total of 77 needles is required. It is of interest to note that for a nominal drop size of 400 microns, the approximate length of the reaction zone is 6.35 cm. Figure 26 is provided which shows velocity deficit as a function of radial distance for the selected chamber geometry.

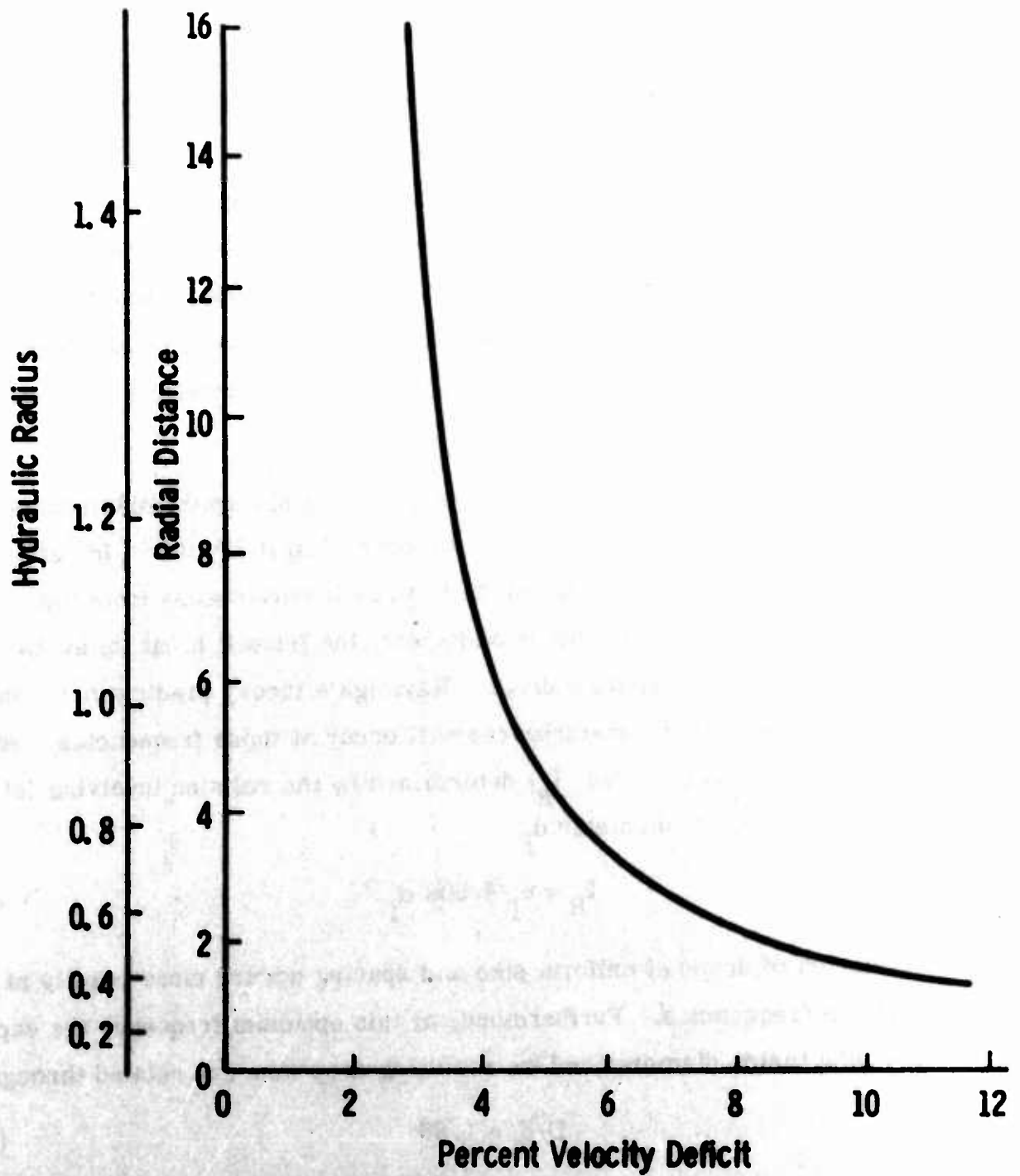


Figure 26. Velocity Deficit Versus Radial Distance from Chamber Vertex for Geometry Selected

2. Method of Fuel Cloud Production

This phase of the research has been directed toward establishing a satisfactory technique for generating a cloud of fuel drops, initially of uniform size. A drop-generation technique, different from those previously employed in our work, was developed to produce a spray of fuel drops of nearly uniform size and spacing (Figure 29). The technique provides for a further extension to the vibrating capillary jet methods, based essentially upon Rayleigh's⁽²⁹⁾ analysis of jet instability. The decision to develop a new technique was made following preliminary tests involving those already in existence.

The basis of all the techniques is to apply a sinusoidal disturbance to a liquid jet emerging from a vertically mounted capillary tube. In each such jet, the disturbance will grow in the fluid as it moves away from the capillary exit. If this growth rate is sufficient, the jet will break up at its contractions, forming separate drops. Rayleigh's theory predicts maximum amplification of cyclic disturbances will occur at those frequencies (referred to as Rayleigh frequencies, f_R) determined by the relation involving jet velocity, u_j and jet diameter d_j :

$$f_R = u_j / 4.508 d_j \quad (132)$$

Formation of drops of uniform size and spacing occurs more readily at such Rayleigh frequencies. Furthermore, at this optimum frequency the capillary tube inside diameter and the resulting drop size are related through

$$D/d_j = 1.89 \quad (133)$$

Similarly, the wavelength associated with f_R in Equation (132) is related to drop size by

$$\lambda/D = 2.38 \quad (134)$$

It should be pointed out that Rayleigh's analysis was developed for a stationary capillary column of an inviscid fluid. The analysis was later extended to include the effects of liquid viscosity and jet velocity. Two characteristic velocities can be associated with the problem of liquid exiting from a capillary tube. The velocity of a smooth jet exiting from a capillary tube is dependent on surface tension σ , density of the liquid ρ_l , and diameter of the jet d_j through

$$u_j^2 \geq 8\sigma/\rho d_j \quad (135)$$

Hence, Equation (135) expresses the fact that a capillary jet must have a certain minimum velocity, u_{\min} , to avoid dripping. Using Equations (132) and (135), a Rayleigh frequency associated with this minimum velocity can be obtained

$$f_R = 0.627 [\sigma/(\rho d_j^3)]^{1/2} \quad (136)$$

Upon exiting from the capillary tube, the liquid jet will break up and the drops will accelerate due to gravity and approach their terminal velocity. In the approximate range of drop diameters $290\mu < D < 2600\mu$ the drag law for falling drops ($10 < Re < 1000$) can be taken as $Re^{1/2} C_D = 9.64$. Thus, it can be shown⁽³⁰⁾ that when the initial jet velocity equals the terminal drop velocity, the particular Rayleigh frequency for these conditions, f_R^* , is determined by

$$f_R^* = 0.112 (\rho_l^2 g^2)/(\rho_g \mu_g)^{1/3} \quad (137)$$

Operating at f_R^* tends to deter coalescence of successive kerosene drops greater than approximately 350 microns, since the drops are formed at their terminal velocity and therefore do not accelerate further. Figure 27 compares the terminal velocities of liquid drops in air, u_d , with the minimum jet velocities required to avoid dripping.

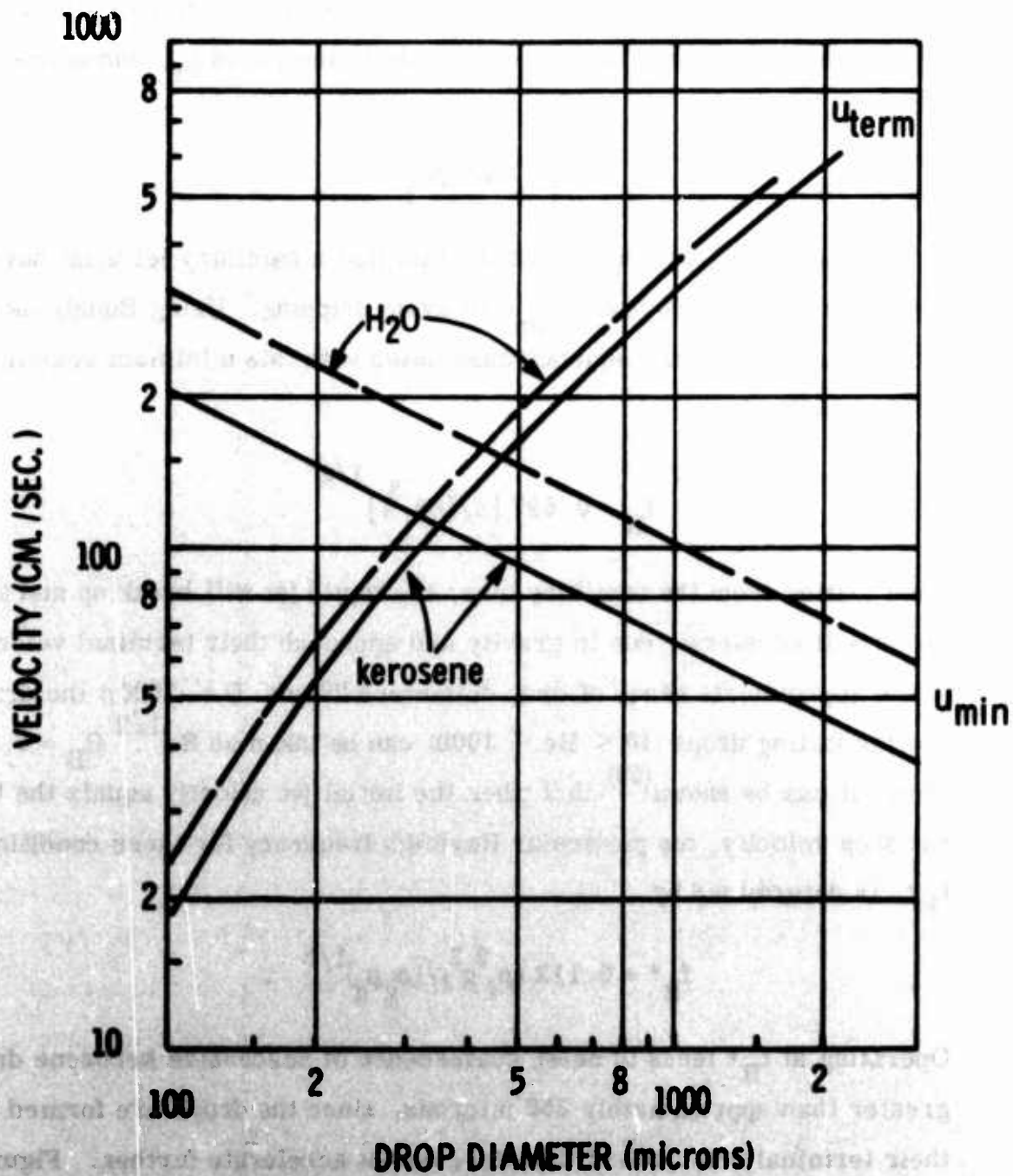


Figure 37. Terminal and Minimum Velocities of Water, Kerosene and DECH Drops

Heretofore, the research efforts of these laboratories into two-phase detonations have made extensive use of a method of spray production developed by Dabora et al^(31, 32). In his method the cyclical disturbance is introduced in the liquid supply reservoir by means of a vibrating diaphragm. This disturbance is transmitted through the fluid moving in the capillary needles, located directly below the diaphragm, to the free jet. In his research Dabora chose to operate his system at the minimum jet velocity. Consequently, he had drop coalescence occurring for drop sizes with $u_{\min} < u_{\text{term}}$ (Figure 27). This was partially overcome in such cases by introducing an air stream collinear to the liquid jet, termed coflow. More recently, T. H. Pierce⁽²⁷⁾ developed a second method during the course of his work involving both monodisperse and polydisperse sprays⁽³³⁾. By his technique the fluid flow to each individual needle is carried by a small inside diameter flexible plastic tube which passes through a vibrating platform. The oscillatory disturbance introduced into the fluid in this way is transmitted to the jet issuing from the needle. The operating frequency of the disturbance is established by Equation (137), i. e., the maximum amplification frequency is chosen as the operating frequency, $f = f_R^*$.

It was anticipated from the outset that the present research would be involved with capillary needles numbering nearly an order of magnitude more than had previously been used. Hence, every possible simplification was deemed desirable as prospective spray generation techniques were considered. The latter method by Pierce was rejected in view of the complexity of the plumbing required. The former method by Dabora et al had the undesirable trait of requiring coflow to establish drops of uniform size and spacing in the present research. Undue eddies and turbulence would have been established within the test chamber, the

effects of which would have been difficult to ascertain. A further word on this subject is in order. In previous applications the direction of the coflow and the direction of detonation wave propagation were colinear. In the present research, however, had coflow been used it would have been normal to the wave propagation direction. Hence, coflow-induced turbulence greatly enhanced spray distribution uniformity in previous research, whereas in the present work it would have greatly disturbed the distribution.

Both of these drop-generation techniques make use of a vibrator to supply the necessary sinusoidal disturbance. In each case the mass of fluid being disturbed is small; hence, the vibrator power requirement was never questioned since a suitable vibrator was always available. However, in the present research, the mass of the fluid to be disturbed is of an order of magnitude greater, suggesting larger vibrator power requirements. Indeed, tests proved this statement to be true; sufficient disturbances could not be obtained using in-house equipment. Hence, in addition to the undesirable traits mentioned, using either of these drop-generation techniques in the present research would have carried with it a demand for very high vibrator power.

In view of the foregoing considerations, an alternate technique was devised to generate the required monodisperse spray. A motor-driven system was developed in order to generate stronger pressure pulses. The sinusoidal disturbances of the liquid fuel is generated by periodically interrupting the flow to the needles. By this new technique, the disturbance is introduced to the fluid through rotation of a 48-tooth gear enclosed in a cylindrical case. The inlet and outlet ports are so positioned that the top land of the rotating gear simultaneously opens or closes both ports. Kerosene under pressure is fed through one port to the rotating gear. The fuel leaving the pulse generator enters the test chamber through a connected series of eleven sub-manifolds, made up of seven capillary needles each.

Figures 31 through 34 are descriptive of the new drop-generation system. The new system underwent thorough testing to determine operating conditions necessary to generate drops of uniform size and spacing. Table I compares the values of drop size, operating frequency, and fuel/air mixture ratio obtained experimentally with those computed by Equations (133) and (137).

TABLE I. COMPARISON OF EXPERIMENTAL DROP FORMATION RESULTS WITH THEORETICAL PREDICTIONS

	Experimental	Theoretical	Per cent Difference
D	360 μ	384 μ	-6.25
f_R	1584 cps	1550 cps	+1.94
n	1/15.4	1/15.0 (stoichiometric)	-2.6

Strain gage pressure transducers were located in the system to measure both the static pressure of the fuel and the magnitude of the pressure disturbances. The pressure fluctuations at the capillary needles were found to have a 10 per cent peak-peak variation about a static pressure of 13.5 psig.

Photographs were taken of the drops formed at each of the eleven sub-manifold stations along the main fuel manifold to establish the presence of any nodal points in the main manifold exhibited by the formation of drops of highly singular sizes and spacings. Such tests revealed the presence of no such points. Drop formations at the given operating conditions at all eleven stations were very satisfactory. Figure 28 shows the type of drop formation resulting when no disturbances are present, while Figure 29 reveals the nature of good drop formations.

Inherent advantages of this drop-generation system lie in its ease of maintenance and flexibility in terms of future test possibilities. The plugging of small capillary needles by combustion products has always

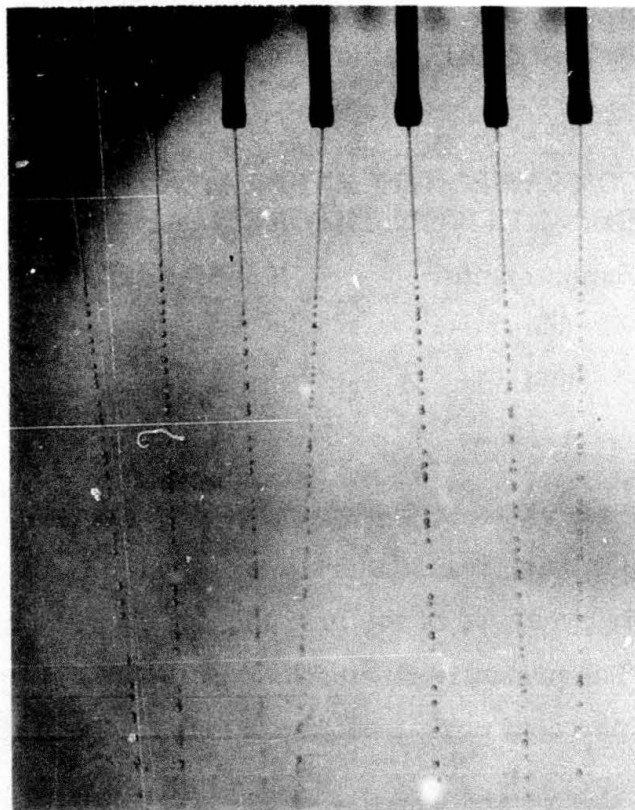


Figure 28. Drops Generated by One Sub-manifold with No Pressure Disturbances Present

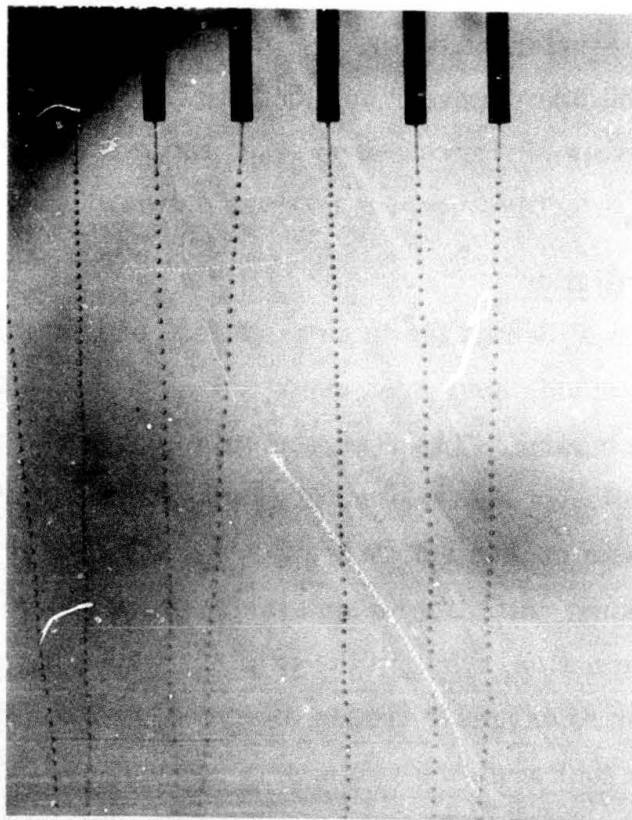


Figure 29. Drops Generated by One Sub-manifold (Figure 34) of a Completely Integrated System with Pressure Disturbances Present. (Kerosene, $f = 1580$ cps, 360 micron drops, 1/16 OD Capillary Needles).

been a problem. The use of quick release fittings to hold the sub-manifolds in place allows for their easy replacement. With such a capability, it is also possible to interchange currently used sub-manifolds with others of varying design. Such design changes could include reduction in the number of needles per sub-manifold or the use of capillary tubing of varying inside diameter, with outside diameter held constant. The second change would result in tests involving varying drop size, while both would involve tests investigating the effects of varying mixture ratios.

3. Explosion Initiation

The initiation of detonation in gaseous fuel-oxygen mixtures is relatively easy and many methods have been used (i. e., spark plugs, glow plugs, shock waves, and even cigars). The replacement of oxygen with air renders initiation more difficult, yet many detonation experiments on gaseous fuel-air mixtures have been conducted. When the fuel is in the form of liquid drops rather than gaseous, initiation is apparently more difficult. In recent studies on two-phase detonation, wherein the oxidizer was systematically varied from pure oxygen to oxygen-nitrogen mixtures, it was found extremely difficult to ignite the fuel when the volumetric percentage of oxygen in the oxidizer was less than about 35 per cent. Further, IIT investigators were unable to generate a sustained detonation with liquid fuel drops of several types in air, although it is possible that part of this difficulty could be attributed to small cloud size and insufficient igniter energy. In view of the above, it was deemed important to carefully consider the method of initiation in connection with the present research.

Initiation techniques considered included auxiliary shock or detonation tubes as well as solid explosives. Auxiliary shock and detonation tubes require more support equipment than the comparable solid explosive system, and the time between experimental runs would be longer. An advantage, however, would be that these techniques can produce a sustained

high pressure, high temperature, and high velocity blast directed at the drops. On the other hand, the explosive process is accompanied by a rapid decrease in these gas dynamic characteristics immediately behind the shock. The latter would render initiation more difficult. In spite of the latter, it was decided to select the solid explosive technique due to its simplicity, flexibility, and the ease with which the energy level could be increased. Uncertainty in the location of the energy threshold point required experimental runs of vastly differing energy releases. Blasting caps and Dupont Detasheet C were used in varying combinations to achieve varying amounts of total energy release. This energy release can be established. The composition of Detasheet C is 63 per cent Pentaerythrite Tetranitrate (PETN), 8 per cent Nitrocellulose (NC), and 25 per cent non-combustibles. The heats of combustion⁽³⁴⁾ for PETN and NC are, respectively, 4280 ft-lb/gram and 2640 ft-lb/gram. Taking a weighted average of these, the heat of combustion for Detasheet is given as 2911 ft-lb/gram or 188 ft-lb/grain. Detasheet was exploded using Dupont blasting caps with a nominal energy release of 1110 ft-lb. Hence, the total initiation energy in the tests described later is equal to the blasting cap energy added to the energy of the Detasheet used.

4. Experimental Apparatus

The detonation chamber shown in Figure 30 is mounted on a Unistrut framework with the chamber centerline approximately 4 feet above the floor. The fuel storage, motor-driven fuel pressure pulse generator, fuel valving, and electrical solenoids are also mounted within the Unistrut framework. A rack cabinet immediately to one side of the detonation chamber houses most of the associated electrical and electronic equipment. Figure 31 is a schematic of the experimental apparatus.

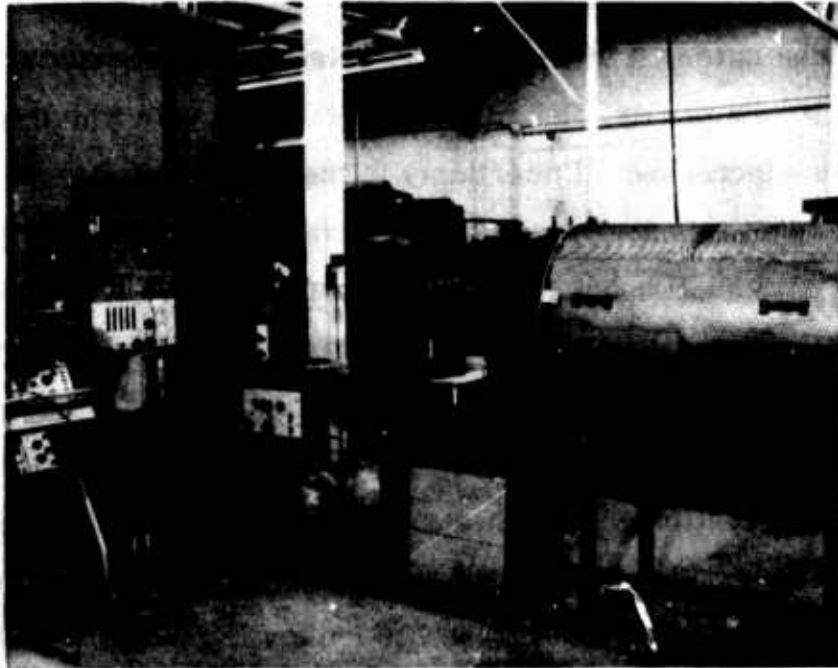


Figure 30. Test Chamber and Associated Electrical and Fuel Systems

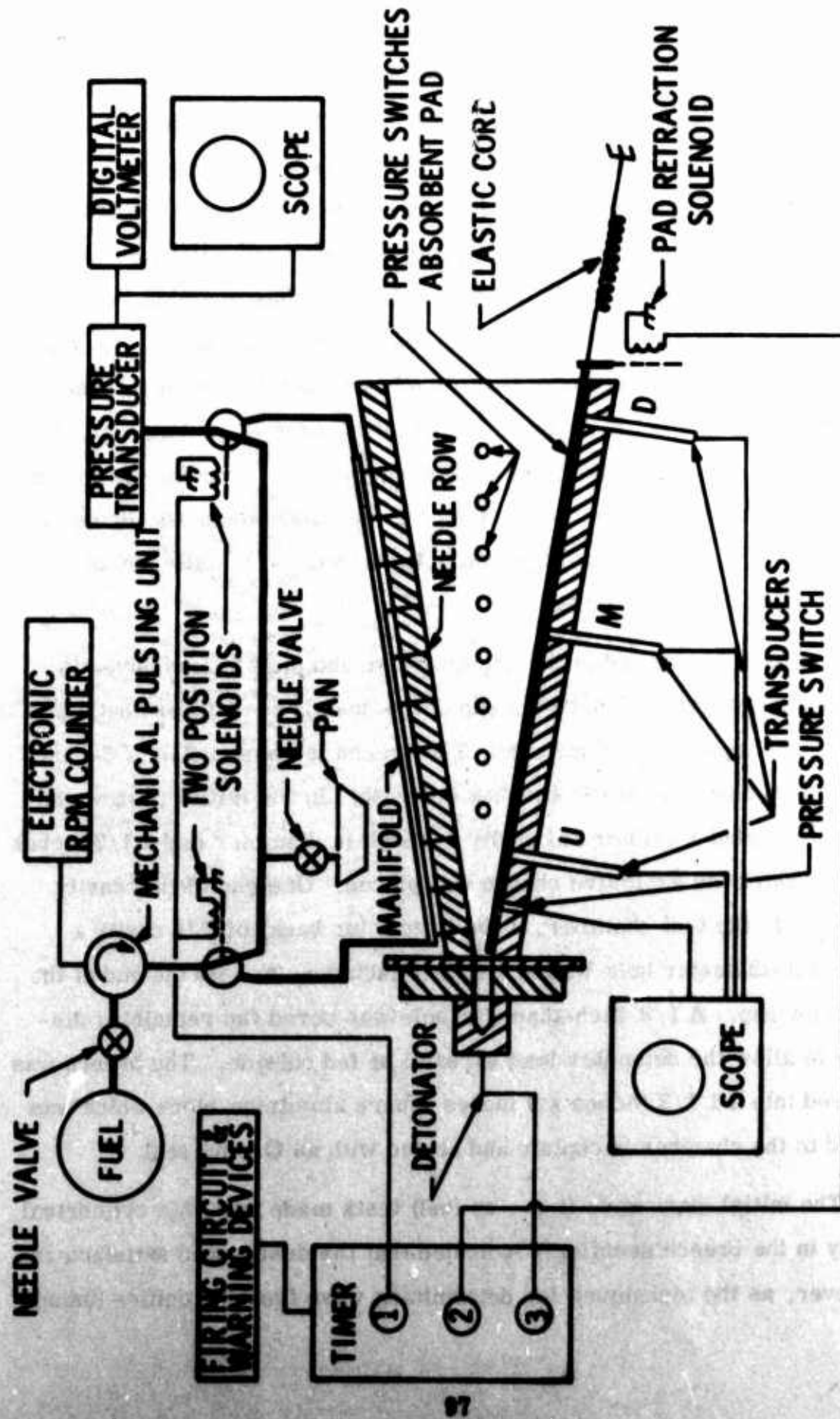


Figure 31. Schematic of Experimental Apparatus

The detonation chamber, without the breech-like explosive charge holder, is 28 $\frac{3}{4}$ inches along the centerline. The top and bottom bars diverge at a 20° total included angle. The inside dimensions of the chamber are 2.05 inches wide, 1 inch high at the narrow end, and 11 inches high at the open end. The top and bottom bars, as shown in Figure 32, are constructed of 1 $\frac{1}{2}$ inches x 4 inches aluminum stock with $\frac{1}{2}$ inch x 1 inch grooves milled along the longitudinal edges. The side windows fit into these grooves and are held in place by larger $\frac{1}{2}$ -inch-thick cold rolled steel side plates bolted through the aluminum top and bottom bars with hardened steel high-strength bolts. For the initial tests aluminum plates have been substituted for the glass windows. However, 1 inch-thick Pyrex windows are available and will be installed when photographic data is required.

A breech, which holds the detonator cap and plastic explosive, is mounted to the narrow upstream end of the chamber. Outward details of the breech are apparent in Figure 33. The breech is constructed of 3-inch-diameter round steel stock 4 inches in length. In the initial design, the breech included a cylindrical cavity $\frac{7}{8}$ inch in diameter and 2 $\frac{1}{2}$ inches deep in which the explosive charge was placed. One end of this cavity was open to the test chamber; at the bottom (or back) of this cavity a $\frac{9}{32}$ -inch-diameter hole was drilled $\frac{1}{4}$ -inch deep to hold the end of the detonator cap. A $\frac{1}{8}$ -inch-diameter hole was bored the remaining distance to allow the detonator lead wires to be fed outside. The breech was pressed into a 1 $\frac{1}{2}$ inches x 9 inches square aluminum block which was bolted to the chamber backplate and sealed with an O-ring seal.

The initial blast wave (i. e., no fuel) tests made with this cylindrical cavity in the breech seemingly indicated that the design was satisfactory. However, as the techniques for determining wave front velocities (using

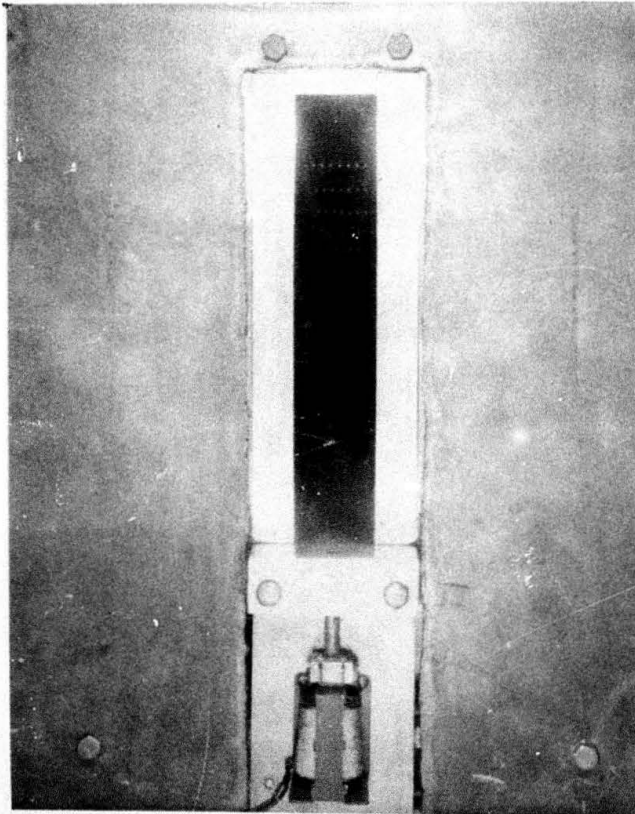


Figure 32. Inside of Test Chamber Viewed from Exit End

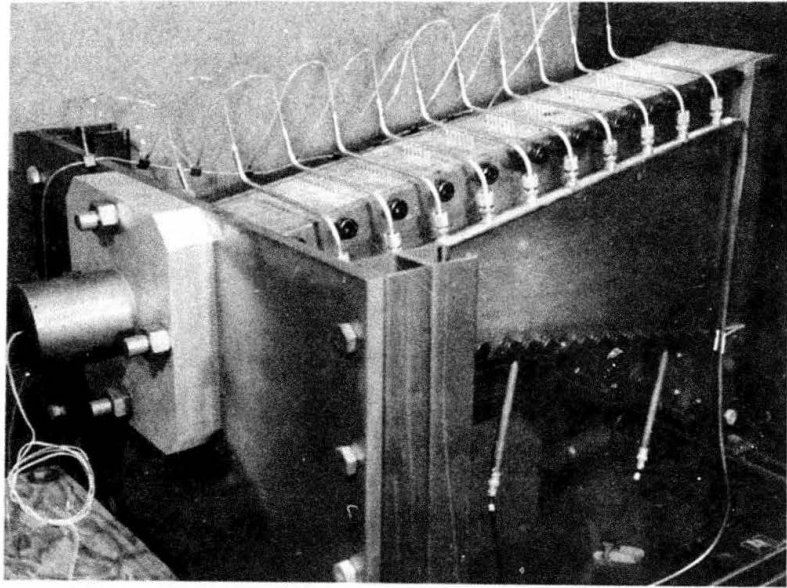


Figure 33. Test Chamber with Fuel Sub-manifolds
(top and breech (left))

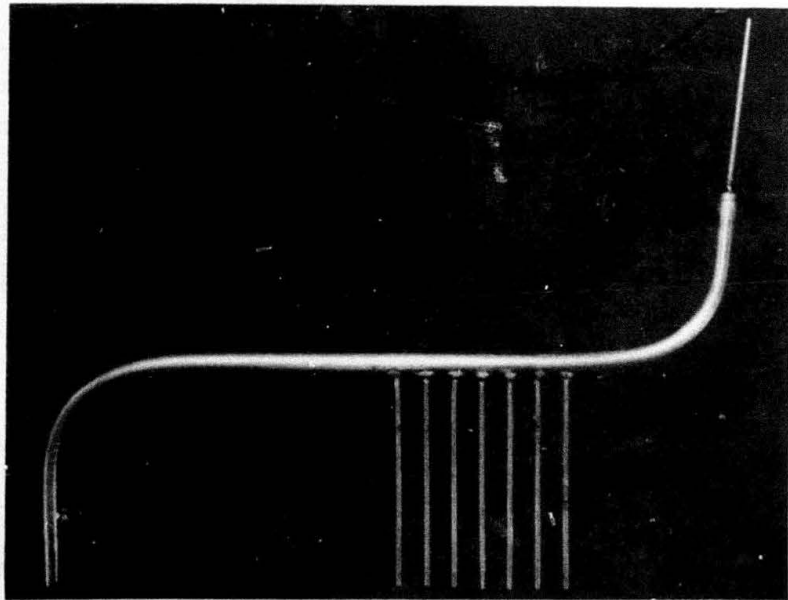


Figure 34. Sub-manifold with Seven 0.008 in. ID Needles

multiple pressure switches, etc.) were improved and the data became more reproducible, an anomaly appeared. The indicated velocity of the blast wave showed sudden increases at downstream chamber positions, although blast waves in a diverging chamber would normally be expected to slow down with increasing values of r .

On the hypothesis that a second shock was overtaking the leading shock (blast wave) and thereby reinforcing and increasing the velocity of the leading wave, the pressure traces (see later discussion regarding pressure transducers used) were examined in detail. In many cases it was apparent that the pressure at a given upstream position increased sharply with the leading wave, and then increased again rather sharply a few microseconds later.

Since both velocity and pressure measurements supported the thesis that a second wave (or waves) was, presumably, reflecting from the backend of the cylindrical explosion cavity, it was decided that this cavity should be redesigned. A new insert for the breech assembly was therefore made. The explosive charge cavity in this modified breech is a compromise between a cylinder and a cone so that the cavity is flared out to match the 1-inch by 2-inches entrance to the test chamber proper. Also, the explosive charge can now be located very nearly at what would be the apex of the top and bottom sides if they were extended.

Although there are surely some reflected waves with this new breech design, the problem of a significant second wave has seemingly disappeared. Essentially all of the blast/detonation wave test results reported in this report were obtained with this improved breech.

Fuel is fed into the chamber through 77 capillary-tube needles. The needles are in 11 groups of 7 needles; the groups are $2 \frac{5}{32}$ inches apart and the needles in each group are $\frac{1}{4}$ inch apart. The stainless steel

needles are 2 inches long, $1/16$ inch outside diameter, and .008 inch inside diameter. These needles are soldered into sub-manifolds of $3/16$ inch stainless steel, seven needles to each sub-manifold as shown in Figure 34. The sub-manifolds are connected to the main manifold with 11 Conax connectors. The main manifold is constructed of a $1/2$ inch outside diameter, $1/4$ inch inside diameter brass tube which runs the length of the chamber top bar. Fuel is fed into the lower end and a pressure transducer is connected to the upper end through a solenoid which is opened during the detonation to prevent damage to the transducer. The main and sub-manifolds were constructed so that gas could not be trapped in any connections or fittings. Continuous gas bleeds are provided on each sub-manifold.

Fuel is stored in a one-cubic-foot spherical tank. In normal operation, fuel is forced out by pressurizing the tank to approximately 50 psig with nitrogen. Fuel flows to the motor-driven pressure pulse generator through a 60-micron filter, a solenoid shut-off valve, a rotometer, and a throttling valve. The pulse generator is driven by a $1/3$ horsepower variable speed motor. Motor speed is indicated by a photo-transistor, light source, and electronic counter arrangement which gives 1 pulse output for 48 pressure pulses in the fuel.

When the fuel system is operated in the setup mode, fuel flows into the chamber into a Plexiglas catch pan, and a pressure transducer is connected to the main manifold. After the proper pressure and disturbance frequency are adjusted, the system is switched to the ready mode. In this mode, fuel is switched to a bypass which is throttled to reflect the same pressure and mass flow as the needles represent. The pressure transducer is also connected to the bypass line. In the automatic firing sequence, the fuel is switched from the bypass to the main manifold $2\frac{1}{2}$ seconds prior to detonation. The bypass arrangement causes the fuel jets and thus the droplets from the needles to be established more quickly.

To prevent fuel from wetting the floor of the detonation chamber during the 2 1/2 seconds the drops are stabilizing, a 1/4-inch-thick absorbent pad covers the entire floor. The pad is snapped out approximately 80 msec prior to detonation. In this way a minimum amount of fuel wets the chamber floor. In spite of these precautions, evidence of film combustion on the chamber walls was observed. This phenomenon was qualitatively established on the basis of a special series of tests. A series of blast wave (no fuel added) tests were performed immediately following a series of detonation tests without cleaning the chamber walls. These special runs revealed both audible and visual evidence typical of kerosene combustion. Quantitative indications of film combustion were also obtained from detonation tests by a comparison of the data taken before with that taken after careful cleaning of chamber walls. Such comparisons of detonation test results showed that film combustion apparently results in greater scatter in the experimental data as well as a modest increase in the magnitude of wave pressure and velocity. These increases were more evident in the upstream portion of the chamber where the ratio of wall surface to cross-sectional area is greatest.

In view of the indication that residual fuel had remained on the chamber wall and reacted in later tests, a better procedure for chamber cleaning between tests was adopted. The chamber walls are now washed out with trichloroethylene between tests involving liquid fuel. The effects of any reaction with a film of residual fuel have seemingly been eliminated. The results of tests involving fuel presented in this report were obtained using the improved cleaning procedure.

The test results presented in this report were obtained by means of three pressure transducers and several pressure switches. The output from these transducers and switches were recorded using three Tektronix oscilloscopes, each with an oscilloscope camera.

One pressure switch and three pressure transducers were mounted in the bottom of the chamber 0.18, 0.54, 1.39, and 2.28 feet, respectively, from the vertical back plate of the test chamber. The pressure switch is the first device to sense the blast wave from the explosive charge. The signal from this switch triggers the scopes and provides a point of time reference for all other data recorded. The pressure transducers, shown in Figure 35, are similar to those described by Rao⁽³⁵⁾. As shown in this figure, a .125-inch-diameter, 0.050-inch-thick lead-zirconate titanate (PZT) element is soldered between two .125-inch-diameter copper rods, .375 inch and 6.50 inches long. Since copper has approximately the same acoustic impedance as the PZT crystal, very little reflection of the longitudinal elastic wave occurs at the interfacial surfaces. The elastic wave does reflect off the far end of the copper rod and affect the transducer output but at a time after most of the desired pressure data has been recorded. PZT exhibits a very low mechanical Q, and this reduces problems with oscillation or ringing of the crystal. The rod crystal assembly is potted in a brass housing with Dow Corning RTV 521 Silastic. The short copper rod is connected electrically to the outer housing by a very fine copper wire, and the end of the long copper rod is connected to the center of a BNC connector attached to the end of the transducer housing. A typical calibration curve for one of the transducers is shown in Figure 36. These transducers were individually calibrated in a detonation tube using known gaseous detonation conditions.

In addition to the three pressure transducers and the one pressure switch referred to above, eight pressure switches have been installed in a radial line along one of the side walls of the test chamber. The distance between each pressure switch is 2.4 inches. These switches are connected into a raster circuit so that as the leading wave, blast or detonation, passes each switch in succession, the event is indicated on a scope trace.

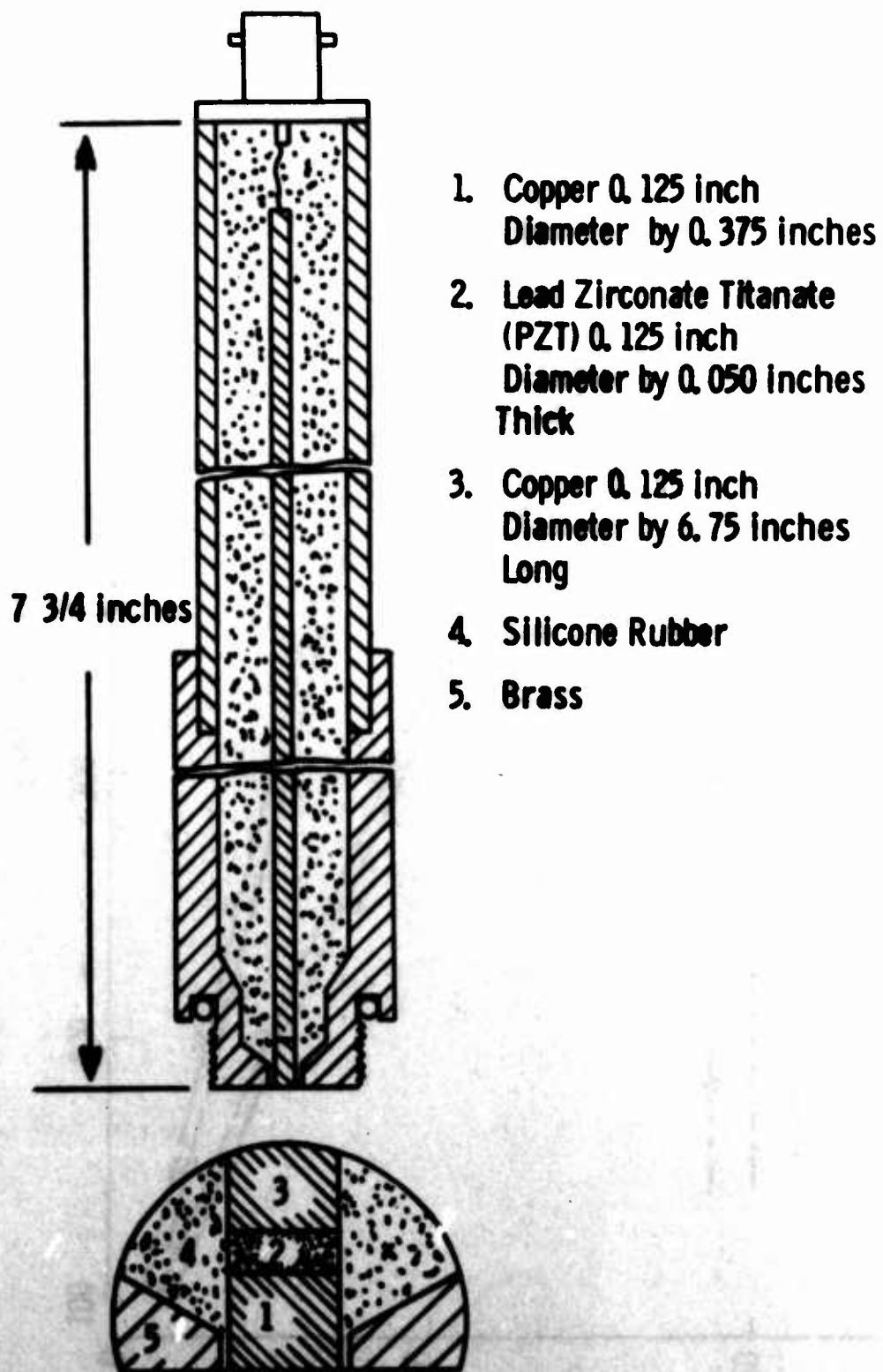


Figure 35. Pressure Transducer Assembly

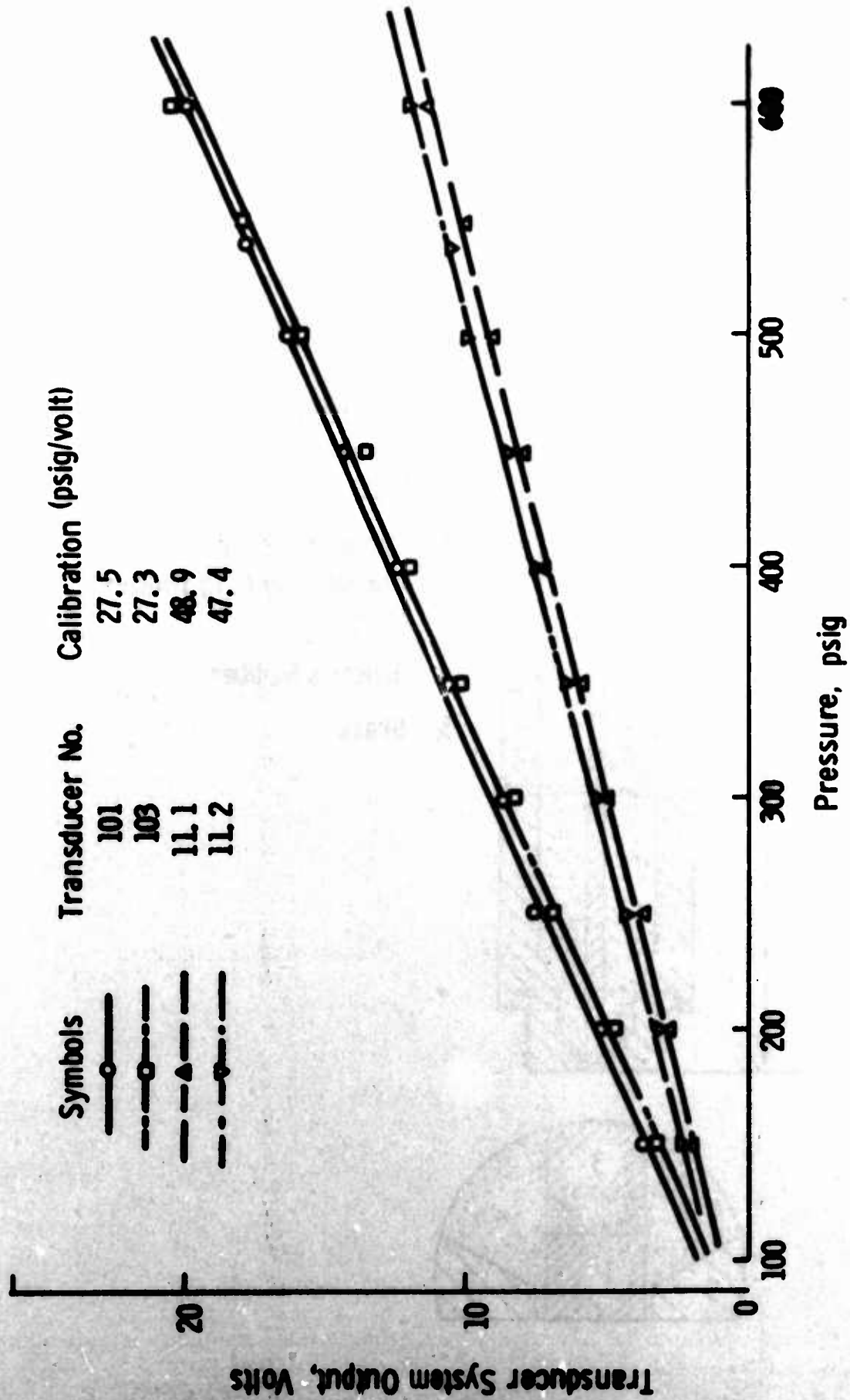


Figure 36. Pressure Transducer Calibration

These pressure switches are made up essentially of a 1/3 inch stainless steel tube with an insulated center conductor and a thin diaphragm soldered across the end of the tube exposed to the chamber. Figure 37 is a sketch of one of these switches. Although pressure switches of a basically similar nature have been used at this laboratory for years in detonation work, the switches used here are of a new design. The main virtues of this revised design over switches previously used are its small diameter and extended length. Since a large number of switches were to be mounted fairly close together in a fairly thick wall, this particular design appeared to be appropriate.

Prior to the design and fabrication of these pressure switches several small and inexpensive Pin-ducers* had been installed in the same locations. While these inexpensive pin-ducers apparently had the desired characteristics of fast response time and relatively high outputs (for the pressure increase expected), they failed to survive a large number of blasts. After a few tests they generally became erratic, apparently due to erosion of the very thin coating on the pressure-sensitive end. When it was learned that these Pin-ducers were really designed to survive only one strong blast wave, no further attempts were made to use them. Effort was therefore directed toward the development of the pressure switches discussed above.

5. Experimental Procedure

A systematic experimental procedure was established to minimize the chances of wasted runs, either as the result of equipment failure or human error. The sequence of events prior to a detonation run is as follows:

*These Pin-ducers are co-axial piezoelectric (modified barium titanate) transducer pins, Channel Industries part number PK 14-X.

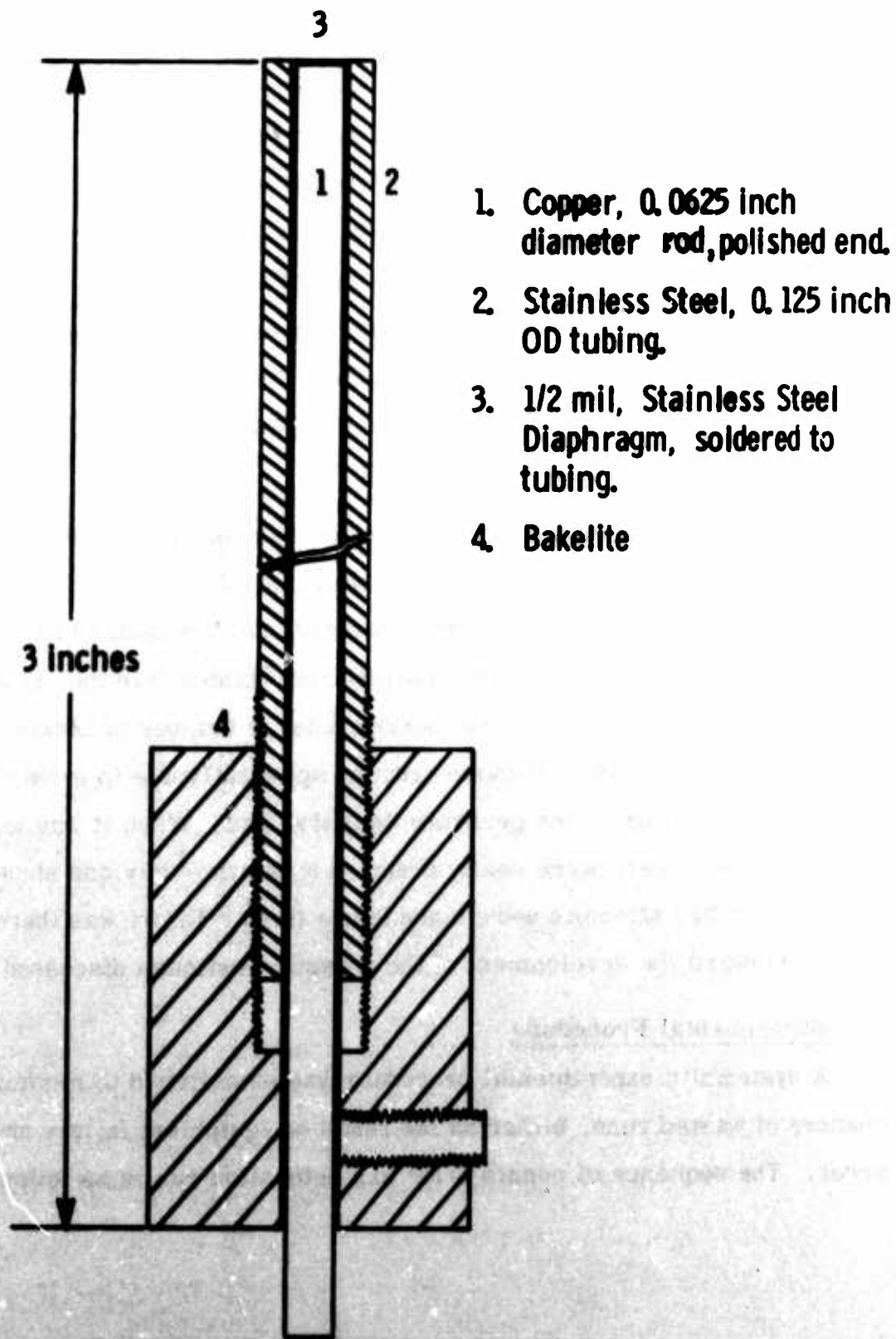


Figure 37. Pressure Switch Assembly

1. Inspect detonation chamber and remainder of basic hardware.
2. Inspect and adjust pressure and time of arrival measurement instrumentation.
3. Clean detonation chamber thoroughly.
4. Install fuel catch-pan in chamber and start fuel flow.
5. Adjust fuel pressure and pressure pulse generator frequency to operating conditions.
6. Switch fuel system to ready mode and remove catch-pan.
7. Install absorbent pad and arm pad retraction mechanism.
8. Install detonator cap with appropriate amount of plastic explosive attached in breech.
9. Secure breech to backplate studs.
10. Arm detonator circuit.
11. Arm automatic run sequencer.
12. Open scope camera shutters.

The start-run switch activates warning lights and an eight-second duration warning horn in the test area. Ten seconds after start, a mechanical microswitch timer is started. The timer turns fuel on immediately, 2 1/2 seconds prior to detonation and turns off within 1 second after detonation. Approximately 80 msec prior to detonation, the absorbent pad is snapped from the chamber.

Immediately following detonation, fuel is shut off, the detonator and automatic run sequencer are disarmed, and the photographs of the oscilloscope traces are developed. When detonation in an oxygen-enriched atmosphere is desired, the chamber is first purged of air by filling the chamber with premixed oxygen and nitrogen through a port in the bottom near the pressure switch and a thin film of plastic is taped across the open exit end. Throughout the run, the premixed N_2-O_2 is blown slowly into the chamber to maintain the desired chamber atmosphere. The procedure required to carry out blast wave runs eliminates steps 4 through 7.

C. RESEARCH RESULTS AND DISCUSSION

1. Introduction

It is unlikely that a complete and detailed analytic solution is possible to the complex problem of fuel-air explosions. The formulation and solution of such a complex model must then rely heavily upon experiment. Theoretical consideration of this problem was initially directed toward a detailed discussion of the two limiting solutions of a complete FAE model—the cylindrical blast wave and cylindrical Chapman-Jouguet detonation wave.

Experimental FAE research has similarly been directed toward the study of these two limiting cases. To this juncture, work has focused upon the evaluation of detonation initiation and propagation characteristics in a fuel cloud. To properly achieve this goal, thorough experimentation was required for both the blast wave as well as the detonation wave. Considerable emphasis has been placed on the attainment of good blast wave data. The reasons for this are basically three-fold. First, it was an expedient way to debug much of the apparatus and instrumentation and to gain experience and confidence in the operation. Second, it was deemed important to assess the degree to which cylindrical blast waves were being generated. Third, good documentation and understanding of the blast wave data should provide an experimental technique for the determination of initiation requirements for the two-phase detonation.

Table II gives an abbreviated summary of experimental tests performed during the course of this research. Work progressed from the initial stage of hardware development and calibration through the preliminary testing phase to the final data seeking phase.

The information obtained during the controlled tests consisted of the wave time of arrival at eight different chamber radii and wave pressure at three different radial positions. The wave time of arrival data is

TABLE II. SUMMARY OF EXPERIMENTAL TESTS PERFORMED

Run No.	Type	Explosive Charge ^a	Comments
	Hardware Development and Calibration		Items tested included pin transducers, pressure switches, pressure transducers and associated instrumentation.
1-30	Blast Wave	1100-8400	Original breech design
31-41	Blast Wave ^b	1100-8400	Improved breech
42-46	Detonation	1100-7000	O ₂ enriched atmosphere
47-60	Detonation	2500-8400	Air detonation with wall wetting problem
61-63	Special	2500	Film combustion check
64-76	Blast Wave ^b	2500-8400	Improved breech
77-85	Detonation ^b	2500-8400	Air detonation with minimized wall wetting

^aTotal energy release in ft-lbf as computed by technique of Section B. 3.

^bResults of these tests presented in detail in the discussion.

obtained from pressure switches positioned in the chamber side wall. The output from these switches is displayed by means of a raster circuit on an oscilloscope. An example of time of arrival data is given in Figure 38 in the form of a scope picture of a raster trace. The wave speed of propagation can be obtained approximately by knowing the distance between pressure switches and the time between raster spikes. However, it is determined more accurately from the slope of the smoothed position-time data. The majority of the data discussed in the following sections is presented in terms of a time measured from the scope trigger time, t' . Figure 39 is representative of wave pressure data taken during the tests.

The following sections present and discuss the results of good experimental blast wave and detonation tests. The problem of relating the wave propagation characteristics, measured experimentally with respect to time t' , to a time associated with the hypothetical origin of the cylindrical model is recognized and discussed. Experimental blast wave data is presented and briefly discussed in terms of its fit to the strong blast wave theory.

The importance of the critical blast wave radius is discussed in light of both experimental and analytical detonation work. Experimental detonation and blast wave results are compared to establish the probable occurrence of a fuel-air detonation.

2. Blast Wave Results

Strong shock waves (blast waves) were produced with various ignition energy levels and without any fuel present in the chamber. As mentioned above, the data were obtained by measuring the time of arrival of the blast waves at various stations along the chamber. This time, t' , was measured from the farthest upstream pressure switch which was used as a trigger for the oscilloscopes. Comparisons of experimental data obtained for three different energy levels are shown in Figures 40 and 41. The energy level indicated represents the grams of Detasheet used in addition

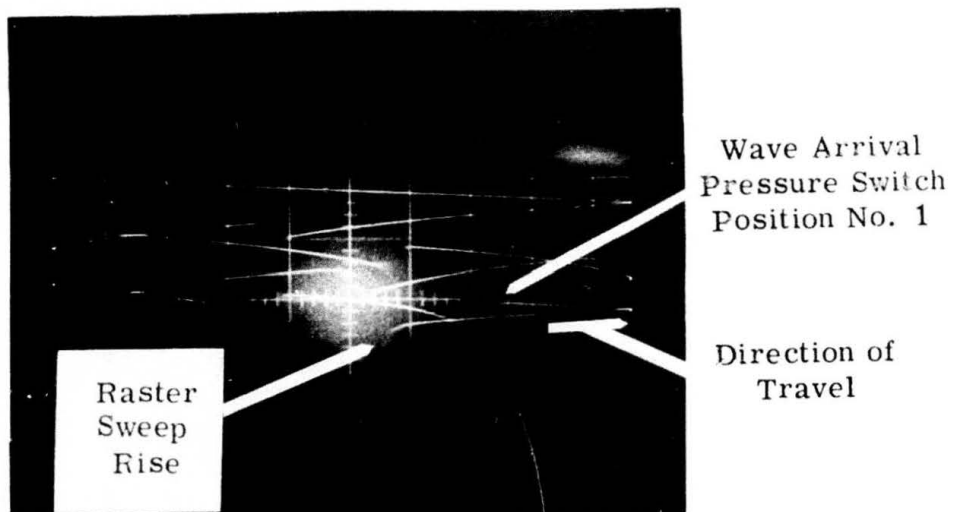


Figure 38. Detonation Run Raster Trace

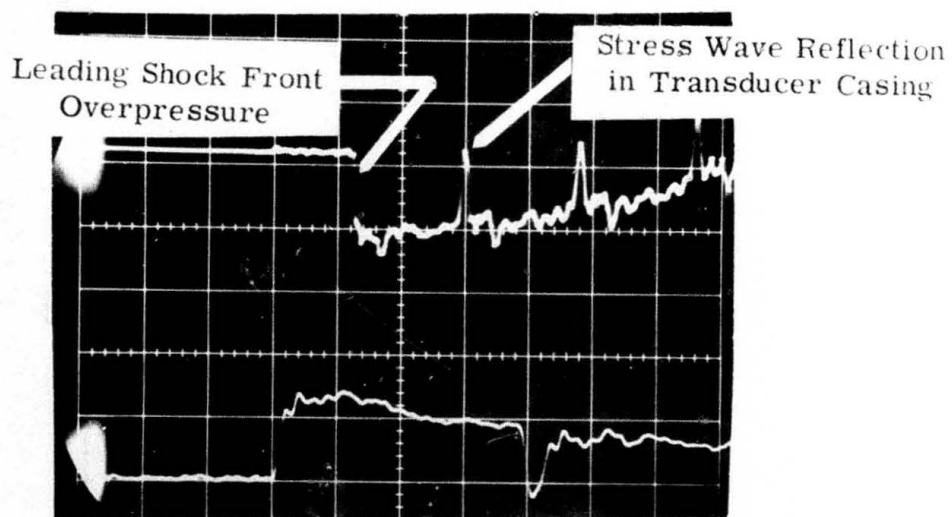


Figure 39. Blast Wave Run Pressure Trace

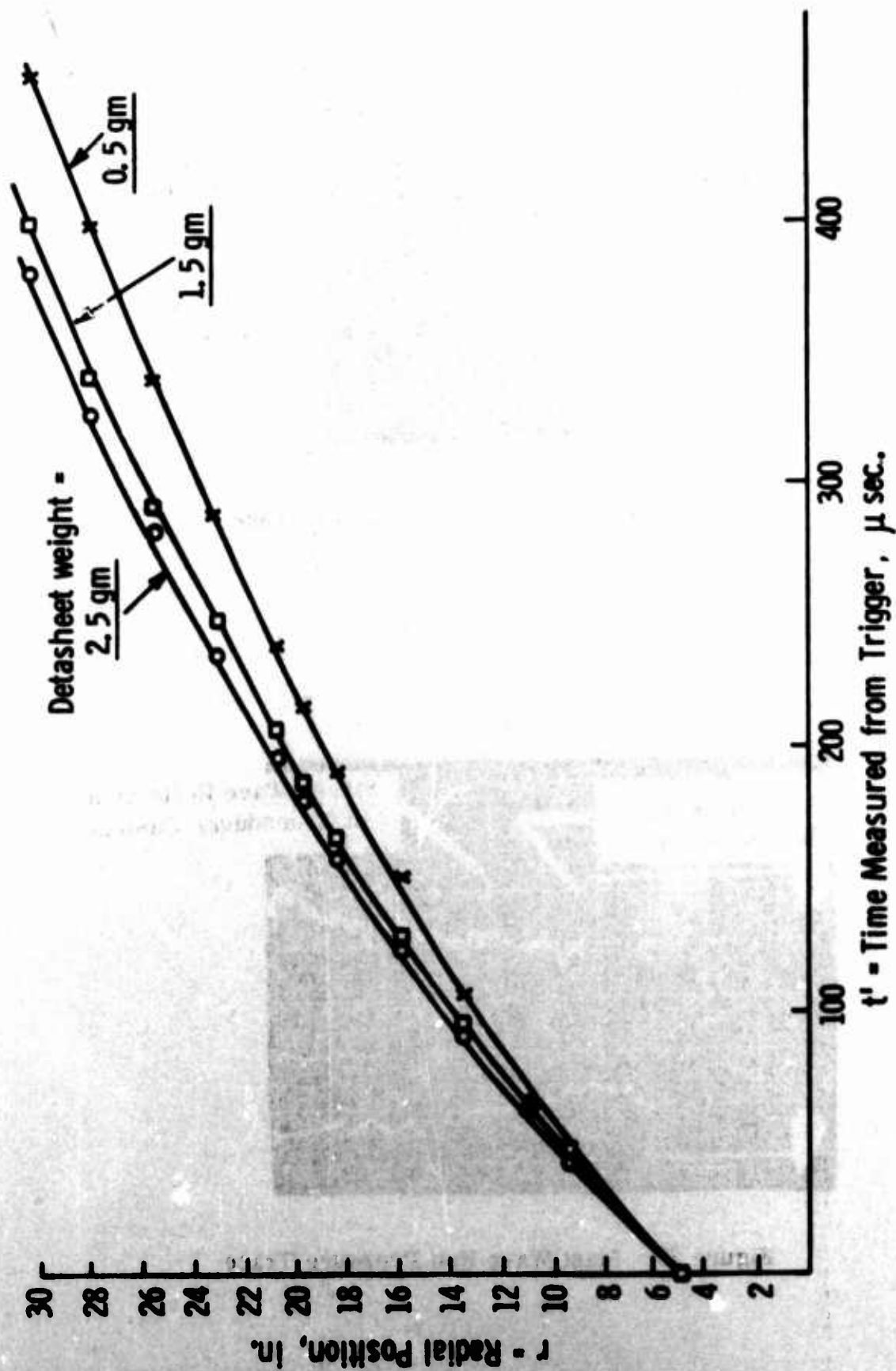


Figure 40. Blast Wave Data Plotted as r Versus t'

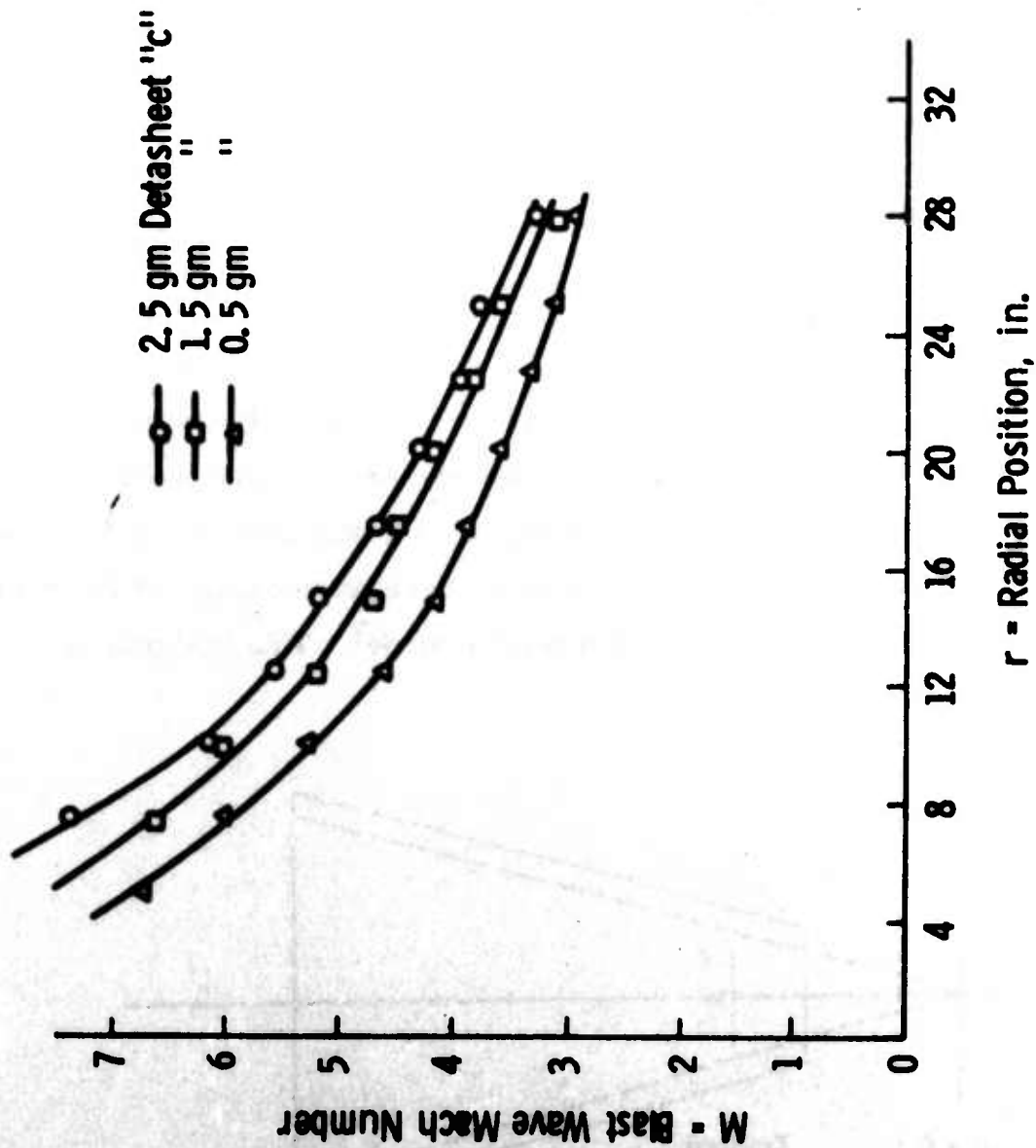


Figure 41. Blast Wave Data Plotted as M Versus r

to the blasting cap. Four runs were made at each energy level. Figure 40 shows the shock wave position versus t' , and the curve drawn for each energy level is the mean curve for the 4 runs. Figure 41 shows the same data plotted as shock Mach number, M , versus r . Values of M were derived from $M = v/a$ where v is shock velocity, a is the speed of sound, and v was obtained from the slope of the $r - t'$ curves. As seen, the data are quite reproducible, and the scatter is reasonably small. As expected, the lower energy levels produced weaker blast waves. Near the end of the chamber the shock strengths have decreased below $M = 4$ for each energy level and hence would begin to deviate from strong blast wave behavior. In all cases, the shocks gradually decay towards Mach waves.

It was of interest to interpret these results in light of cylindrical blast wave theory. In order to do this, it was necessary to determine both the theoretical geometric origin and the time origin of the modeled line-source explosion. First of all, a radius value of $r = 0$ was assumed to be at the hypothetical apex of the chamber; that is, the assumed origin of the cylindrical wave the equipment was designed to model. This is shown in Figure 42.

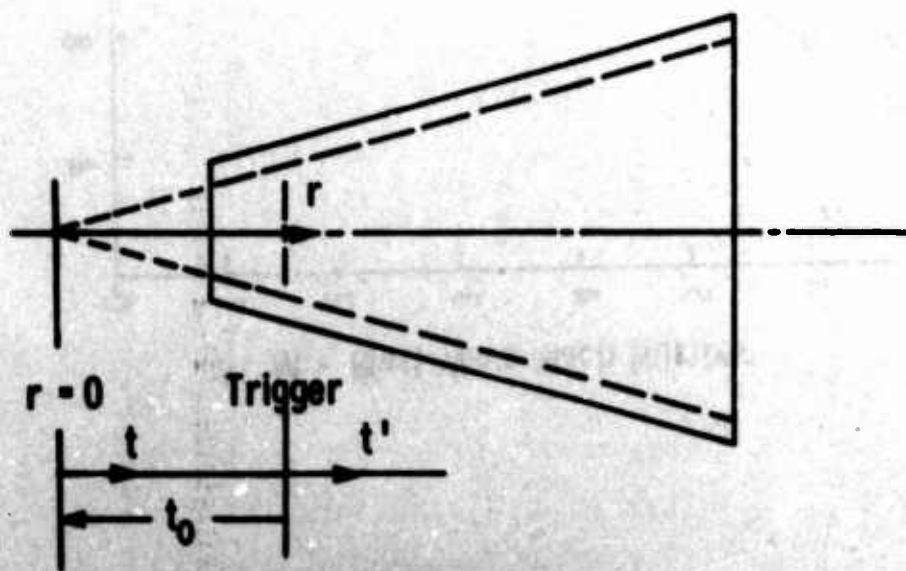


Figure 42. Origin of FAE Model

Once this geometric origin was established, it was necessary to determine the time it would take a blast wave to travel from the origin to the trigger station. This time is represented by t_0 . As all of the time values had previously been referenced from the trigger, the time value, t , referenced from the origin, is determined by

$$t = t' - t_0 \quad (138)$$

where t_0 was also measured from the trigger (i. e., t_0 was negative). This is also illustrated in Figure 42. Using the experimental data graphs of r versus t' for blast waves, a value of t_0 was determined using a geometrical technique described by T.R. Running⁽³⁶⁾. The value of t_0 arrived at for an initiation energy level produced by 2.5 gm of Detasheet "C" and a blasting cap was $-45 \mu\text{sec}$. This is fairly close to the value of $-40 \mu\text{sec}$ obtained by extrapolating the t' versus r curve to the value of $r = 0$.

With the origin determined, it was desired to establish an equation that would describe the experimental results. The form of this equation was naturally chosen to be that of a strong blast wave, that is:

$$t = t' - t_0 = b r^c \quad (139)$$

where b and c are constants. Taking the logarithm of both sides of this equation,

$$\log (t' - t_0) = \log b + c \log r \quad (140)$$

This is the equation of a straight line in slope-intercept form in which $\log b$ is the intercept on the $\log (t' - t_0)$ axis and c is the reciprocal of the slope when $\log r$ is plotted against $\log (t' - t_0)$. However, upon plotting the experimental results, a straight line was not obtained, although a smooth curve did result. This curvature could be altered and eliminated by employing different values for t_0 . Thus, by using a series of successive approximations, a new value of t_0 was determined which produced a straight line

in the $\log (t' - t_0)$ versus $\log r$ graph. This is illustrated in Figure 43 which shows plots obtained using different values of t_0 . The sensitivity of the resultant curve to the value of t_0 should be noted. The value of t_0 derived for the straight line was $-25 \mu\text{sec}$.

The value of c was then determined as the reciprocal of the slope of the above mentioned graph,

$$c = \frac{\Delta \log (t' - t_0)}{\Delta \log r} \quad (141)$$

The value of c for the energy level discussed was found to be 1.56.

A value of b was ascertained in two ways, first by finding the line-intercept value [on the $\log (t' - t_0)$ axis] of the straight line graph, and second, by picking a point on the graph, using the values of c and t_0 already determined and then using the empirical equation

$$t = t' - t_0 = b r^c \quad (142)$$

The former method yielded a value of $b = 2$ and the latter $b = 2.03$.

Using these values for the constants, the derived equation for the data (2.5 grams) was found to be:

$$t = t' + 25 = 2r^{1.56} \quad (143)$$

where t and t' were measured in microseconds and r in inches. This equation is plotted in Figure 44, along with the experimental data plot in which a value of $t_0 = -45 \mu\text{sec}$ was used (the value originally obtained from the experimental data).

According to strong blast wave theory, the relationship between wave radius and time is:

$$t = (\rho/E)^{1/2} r^2 \quad (144)$$

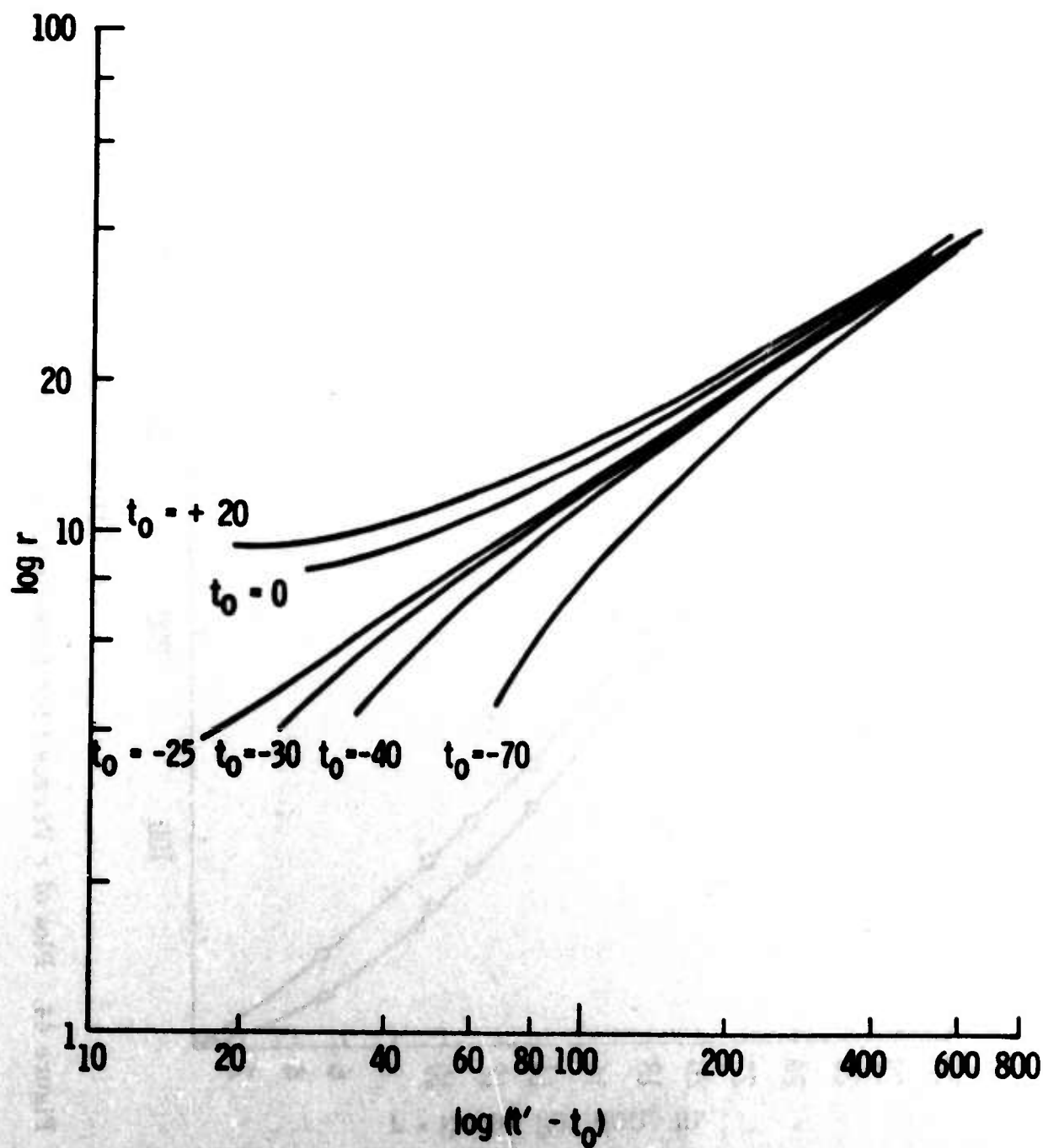


Figure 43. Blast Wave Data Plotted as $\log r$ Versus $\log t$

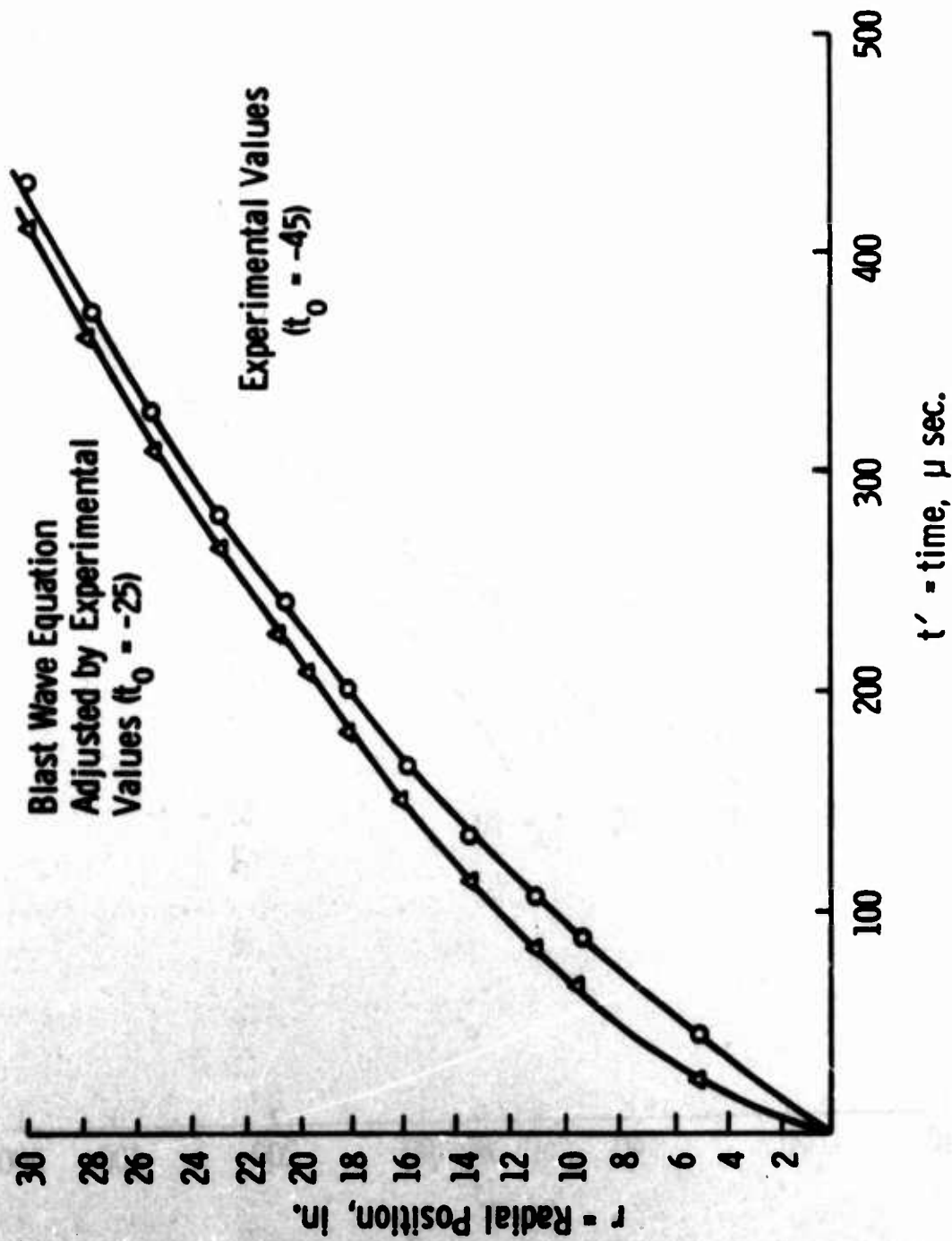


Figure 44. Plot of r Versus t for Experimental Values and Derived Blast Wave Equation

It is to be noted that the experimentally derived value of c is 1.56 as compared to the pure theoretical value of 2.0. Further, assuming no energy losses (such as losses to the chamber walls), a rough value of $(\rho/E)^{1/2}$ was calculated to be 0.338. This value corresponds to the value of $b = 2$ in the experimentally derived equation. Some discrepancy between the strong blast wave theory and the experimental equation could have resulted from the fact that near the end of the chamber a strong blast wave is no longer experienced (i.e., one in which the pressure ratio is much greater than 1.0). Other explanations for the discrepancy include the fact that the charge is not a true line source of energy addition and also that the energy release is not instantaneous. The complete interpretation of the blast wave data is not yet complete, and these points of discrepancy will be considered further.

3. Detonation Test Results

Experimental detonation runs were performed at three different initiation energy levels with kerosene, $C_n H_{2n}$, drops (approximately 360 microns) uniformly distributed throughout the chamber. The overall fuel-air mixture ratio for these tests was essentially stoichiometric, the equivalence ratio, Φ , was 1.04.

The results of these tests are presented as raw data plots of chamber radial distance, r , versus time, t' , for the three energy levels examined. Again a number of runs were made at each energy level, and the curves drawn are the mean of the individual runs. The data is further reduced by taking dr/dt of these curves to derive wave Mach number, M , and plotting this against chamber radius. Figures 45, 46, and 47 are plots of r versus t for initiation energy levels of 8370 (2.5 grams), 5470 (1.5 grams), and 2561 (0.5 grams) ft-lbf, respectively. These energies are computed directly from a known quantity of Detasheet and represent total energy releases of the initiating charge, including the blasting caps.

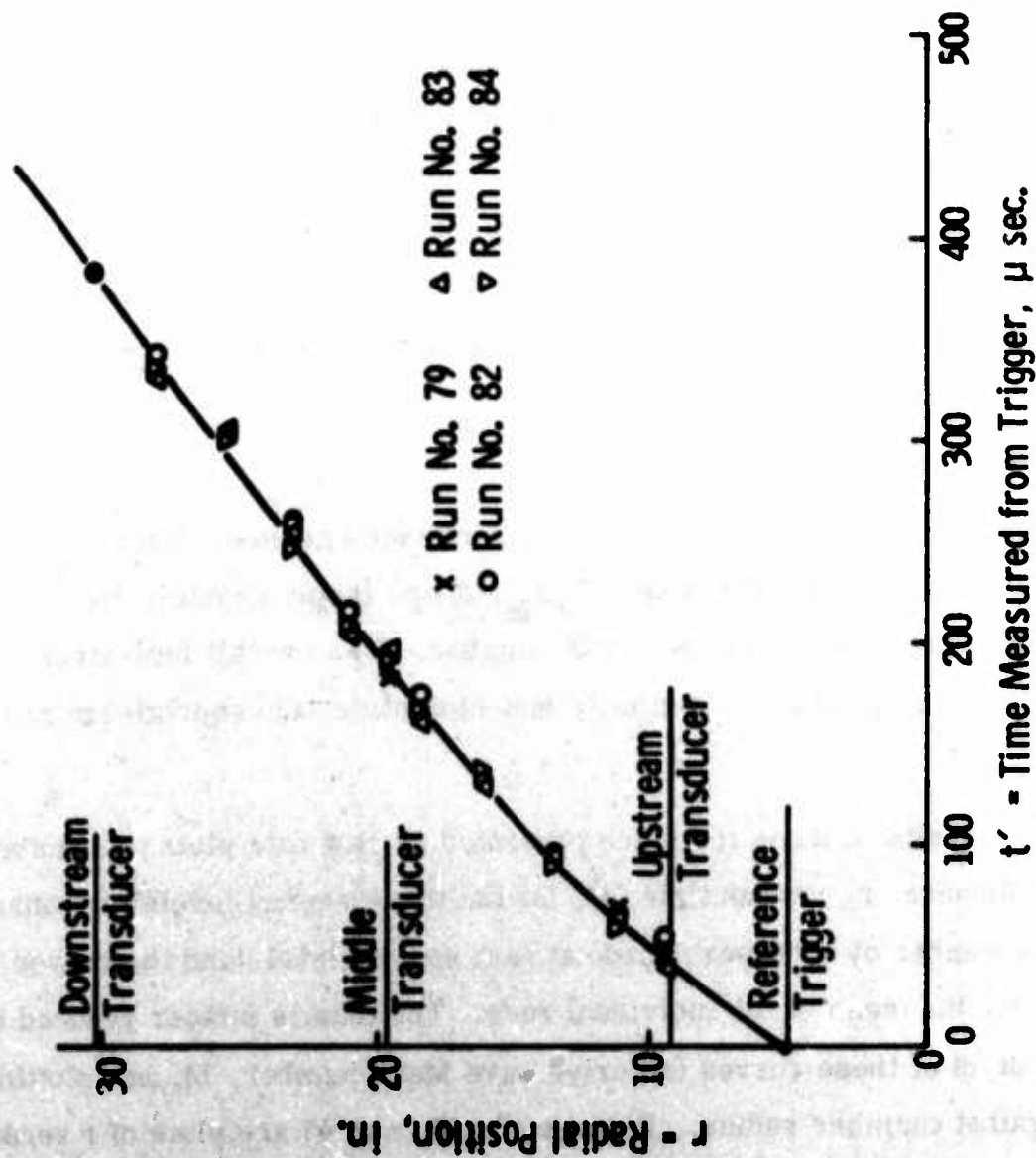


Figure 45. Detonation Data Plotted as r Versus t' for 2.5 gm Detasheet "C"

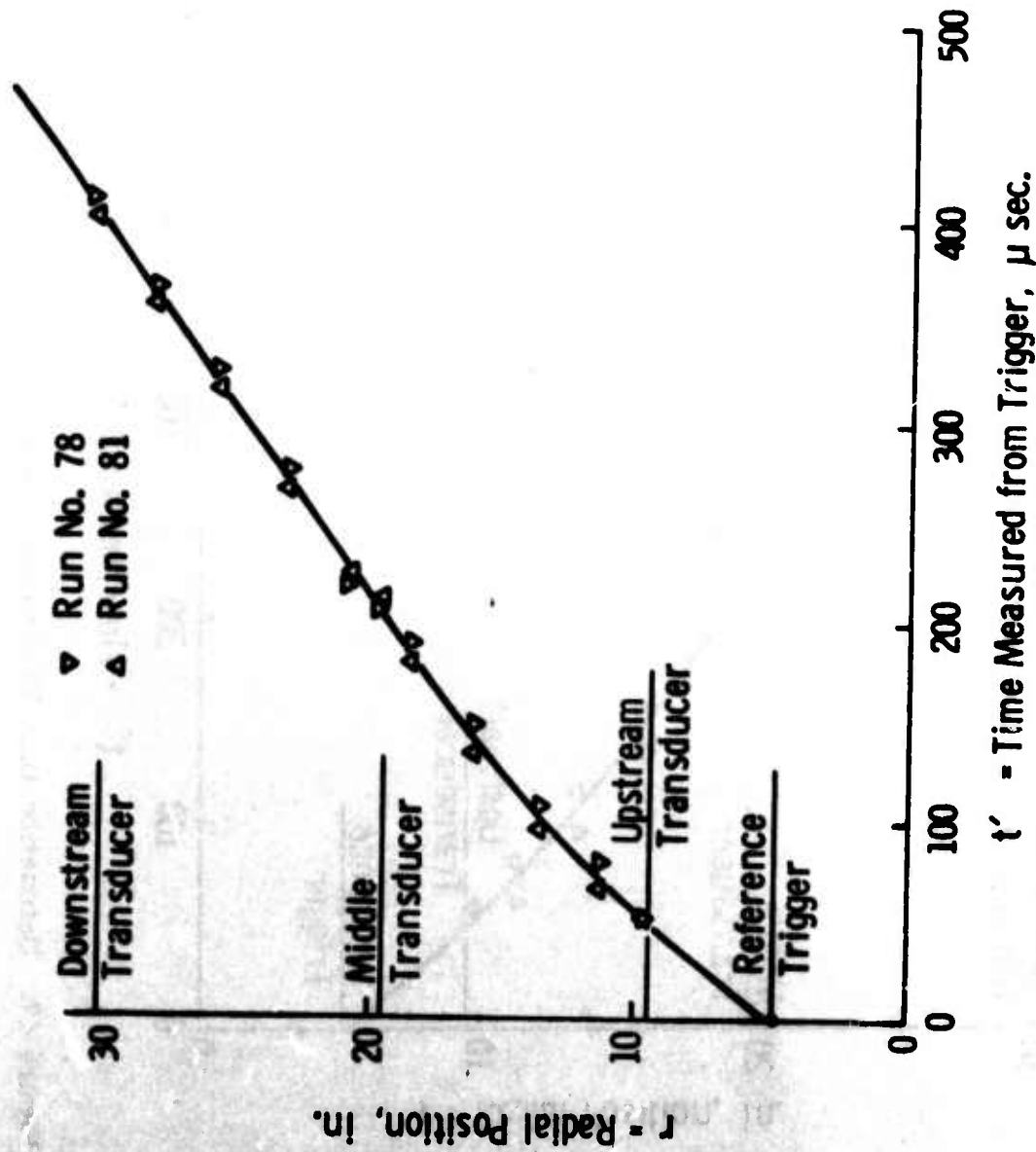


Figure 46. Detonation Data Plotted as r Versus t' for 1.5 gm Detasheet

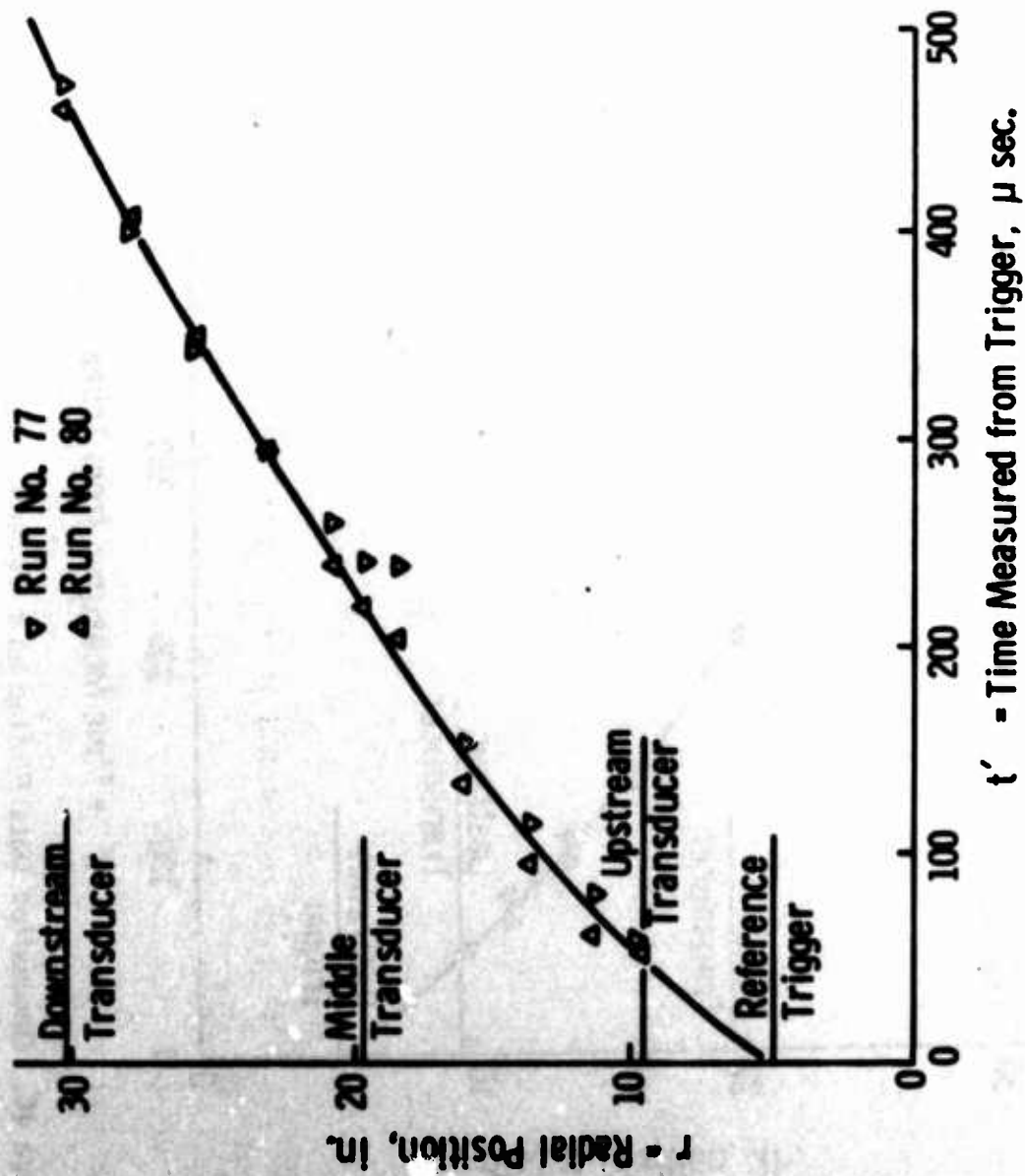


Figure 47. Detonation Data Plotted as r Versus t' for 0.5 gm Detasheet "C"

Figure 45 reveals very strong agreement between four successive high energy experimental runs, a very welcome and rarely achieved experimental result. One can clearly see that downstream of the mid-chamber point the data takes on a linear relationship between r and t' . This result is of extreme interest since it is this precise wave behavior which is commonly associated with propagation of a sustained Chapman-Jouguet detonation. Examination of Figures 45 and 46 reveals the same phenomenon occurring but with slightly varying properties. The curve of Figure 46 also has small data scatter and, significantly, the linear portion of the curve is clearly longer than in Figure 45. This latter fact is of interest when the subject of critical blast wave radius is considered. Figure 47 reveals that, for lower energies than those used in runs for Figures 45 and 46, the data scatter is greater and there is evidence that the wave may be slowing down.

Figure 48 is a plot of Mach number versus chamber radius for the same three initiation energies. The results are quite graphic and descriptive of the process occurring. Before discussing Figure 48 further, calculations were performed using Equation (1) to seek the critical blast wave radius as a function of initiation energy for our particular simplified FAE model. For cylindrical geometry Equation (1) becomes

$$r_* = \left(\frac{E_0}{\pi_1 Q} \right)^{1/2} \quad (144)$$

where all the definitions remain unchanged. The combustion energy release in the detonation wave is needed to make this calculation. Now it is known that use of the constant pressure heat of combustion would lead to considerable inaccuracy. Consequently, it is better to take the experimentally determined Mach number of detonation (or more precisely, the pressure immediately behind the shock) and then calculate Q on the basis of simplified one-dimensional Chapman-Jouguet detonation theory. Within these limitations the conservative equations of energy, mass, and momentum may then be written

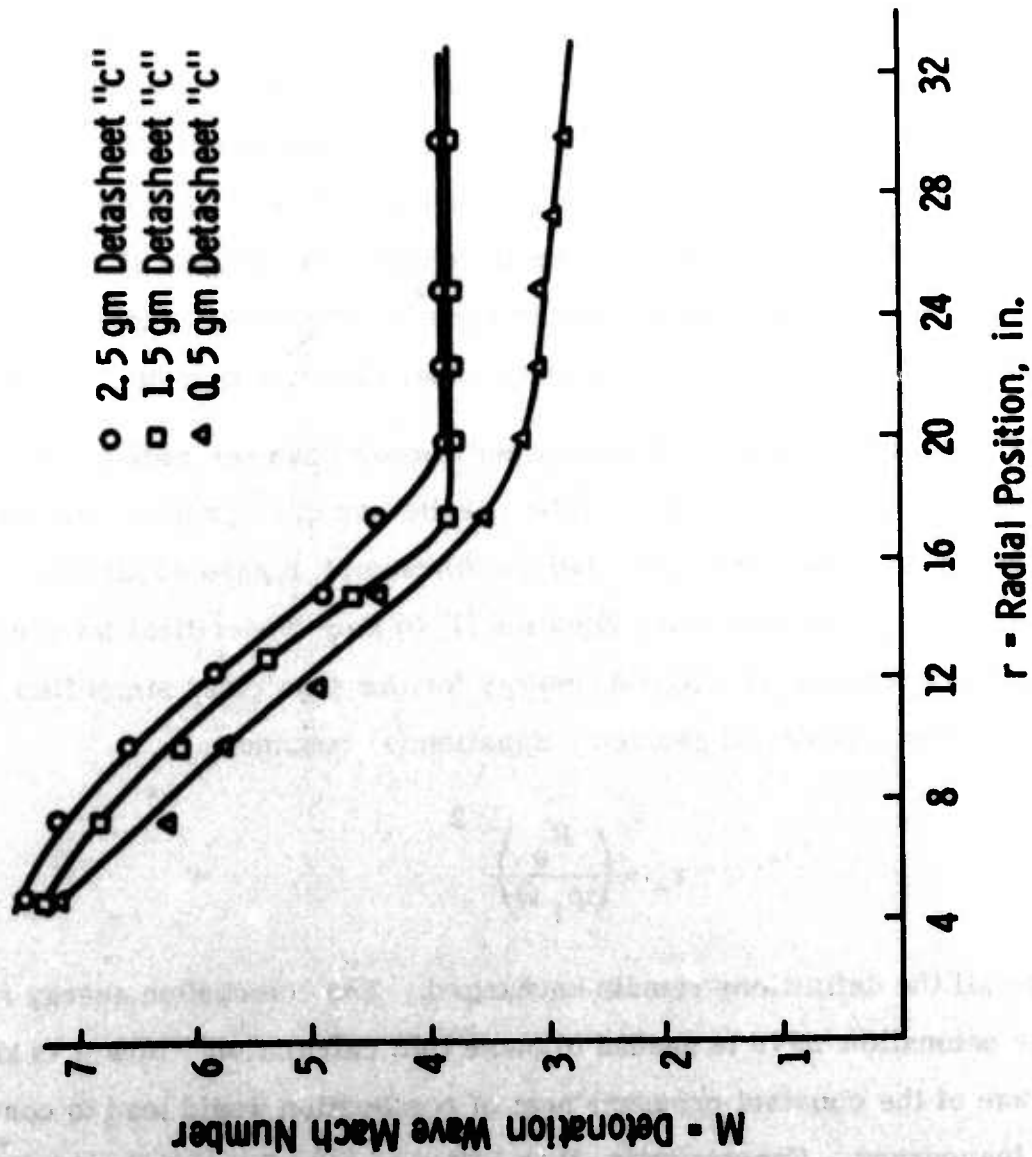


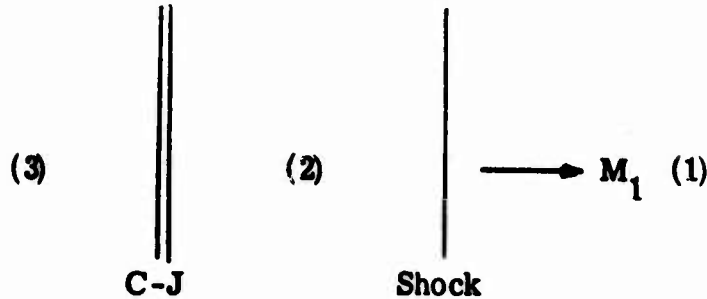
Figure 48. Detonation Plotted as M Versus r

$$h_1 + \frac{v_1^2}{2} = h_2 + \frac{v_3^2}{2} - Q$$

$$\rho_1 v_1 = \rho_3 v_3 \quad (145)$$

$$p_1 + \rho_1 v_1^2 = p_3 + \rho_3 v_3^2$$

where



For a calorically perfect gas,

$$h = \frac{\gamma}{\gamma - 1} \frac{p}{\rho} \quad (146)$$

Equation (145) may be rewritten and solved for Q in terms of ρ_1 , v_1 , γ_1 , and ρ_3 , p_3 , γ_3 ; thus

$$Q = \frac{1}{2} (p_1 - p_3) \left(\frac{1}{\rho_3} + \frac{1}{\rho_1} \right) + \frac{\gamma_3}{\gamma_3 + 1} \frac{p_3}{\rho_3} - \frac{\gamma_1}{\gamma_1 - 1} \frac{p_1}{\rho_1} \quad (147)$$

Knowing that

$$\begin{aligned} p_1 &= 2116.2 \text{ lbf/ft}^2 \\ T_1 &= 537^\circ \text{R} \\ \gamma_1 &= 1.4 \\ \gamma_3 &= 1.2 \end{aligned} \quad (148)$$

the remainder of the parameters must be known in order to solve for a numerical value for Q . It is known that for nearly all detonations

$$\frac{\rho_3}{\rho_1} \approx 1.80$$

and

(149)

$$\frac{p_3}{p_2} \approx 0.55$$

To find (p_3/p_1) we have

$$\frac{p_3}{p_1} = \frac{p_3}{p_2} \frac{p_2}{p_1} \approx 0.55 \frac{p_2}{p_1} \quad (150)$$

At the pressure transducer position (M), the experimental shock pressure ratio p_2/p_1 has been recorded as

$$\frac{p_2}{p_1} \approx 23.0 \quad (151)$$

for both the 2.5-gram and 1.5-gram energy runs. The value of Equation (151) for (p_2/p_1) was assumed for calculations and is justified as it is the ratio in the region nearest the point the wave begins to propagate as a C-J detonation. Thus, on this basis

$$\frac{p_3}{p_1} \approx 12.55 \quad (152)$$

The ambient density, ρ_1 , was computed from the perfect gas law.

The combustion energy release of Equation (147) was found, upon a substitution of the above values, to be

$$Q = 8.975 \times 10^5 \text{ ft-lbf/lbm} \quad (153)$$

A value of critical energy release may then be computed by substitution of the values of Q , ρ , and the desired energy level into Equation (144). The

desired energy level in ft-lbf/ft is arrived at by taking a figure for total initiation energy release, computed by the technique of Section B. 3, and correcting it by a factor established by the geometry of the selected FAE model.

The calculated energy release must be related to the model geometry by considering that it was released within a 20° segment and over a length of 2.05 inches of the modeled cylinder. Therefore, the effective energy release, E_o , required to compute r_{*th} with the calculated energy release and the model geometry can be related by

$$E_{calc} = E_o \left(\frac{2.05}{12.0} \text{ ft} \right) \left(\frac{20^\circ}{360^\circ} \right)$$

or

(154)

$$E_o = 105.3 E_{calc}$$

Figure 49 displays the results of plotting critical blast wave radius as a function of initiation energy for the chosen FAE model.

It is now of interest to return to Figures 45 and 48 and pick-off experimental values of r_{*ex} for comparison with the computed values. The results are given in Table III where the total initiation energy (ft-lbf) has been multiplied by the geometric correction factor to yield E_o in ft-lbf/ft.

TABLE III. COMPARISON OF r_{*th} AND r_{*ex}

Explosive Charge	$E_o \frac{\text{ft-lbf}}{\text{ft}}$	r_{*th}	r_{*ex}	Per cent Difference
2.5 gm	8.82×10^5	25.6	20.0	21.8
1.5 gm	5.77×10^5	20.7	18.0	13.0
0.5 gm	2.70×10^5	14.2	22.0	54.8

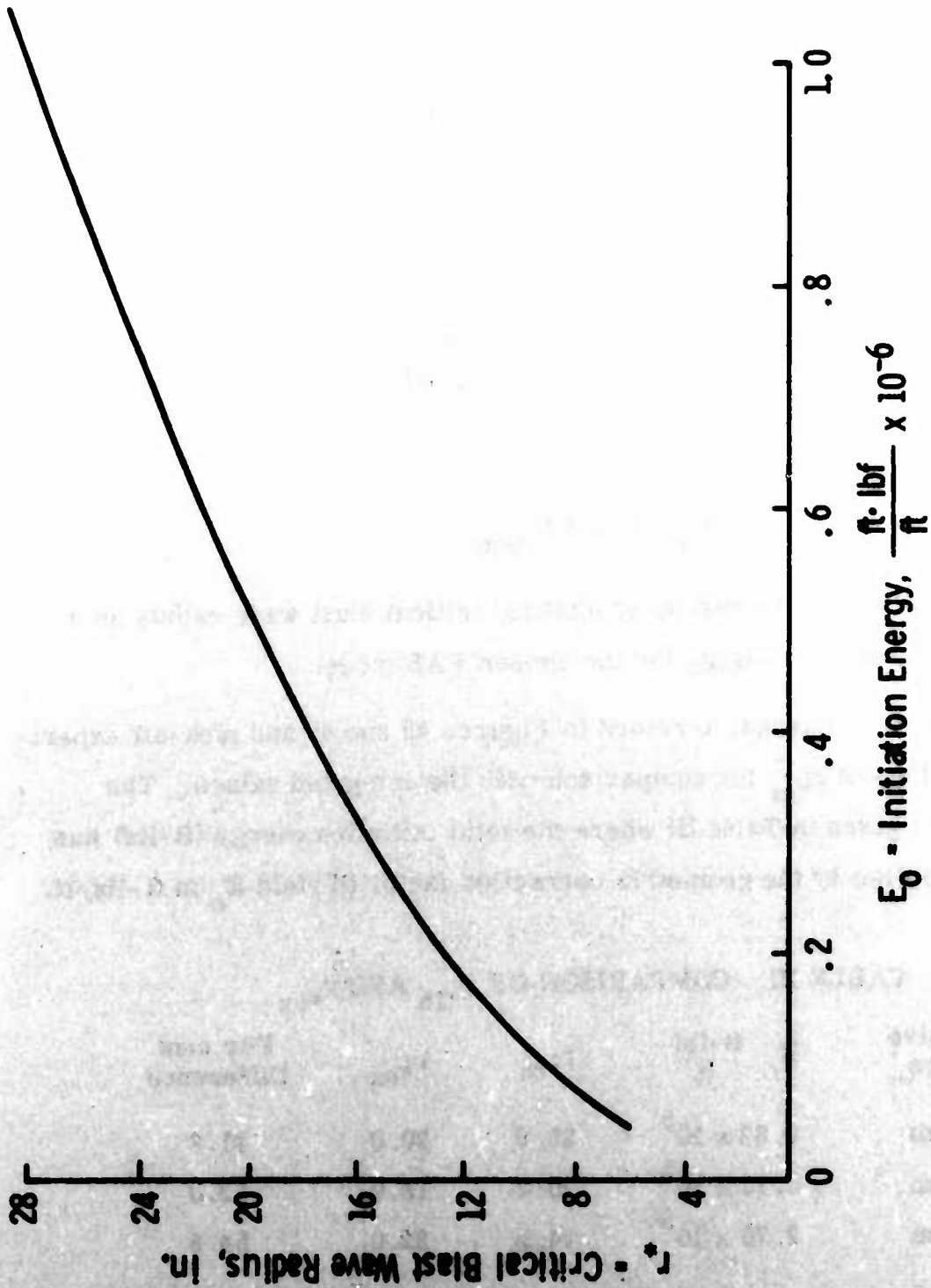


Figure 49. Critical Blast Wave Radius, r_* , Plotted Versus Initiation Energy

The results appear very favorable, yielding an average difference of only 17 per cent, if the lowest energy level could be disregarded.

A comparison of experimental blast wave and detonation results is provided by Figures 50 and 51. The differences on an r - t plot are quite subtle. However, it is the slope of the r - t curve which is of interest, and it can be noted that the slope of the blast wave curve continues to decrease, indicating a decreasing wave velocity. This is not the case on the detonation curve beyond a certain point. On an M - r plot the differences are much more graphic. Both the blast wave and the blast wave initiated detonation begin at closely similar Mach numbers, as they should. As the waves propagate with increasing radius, the blast wave decays markedly.

It is clearly evident from the foregoing that a wave structure was propagated with characteristics normally associated with those of a Chapman-Jouguet detonation. While the results appear most promising, further study is required to establish greater experimental documentation of the propagation of cylindrical detonation waves. The experimental results must also be further compared with theoretical predictions.

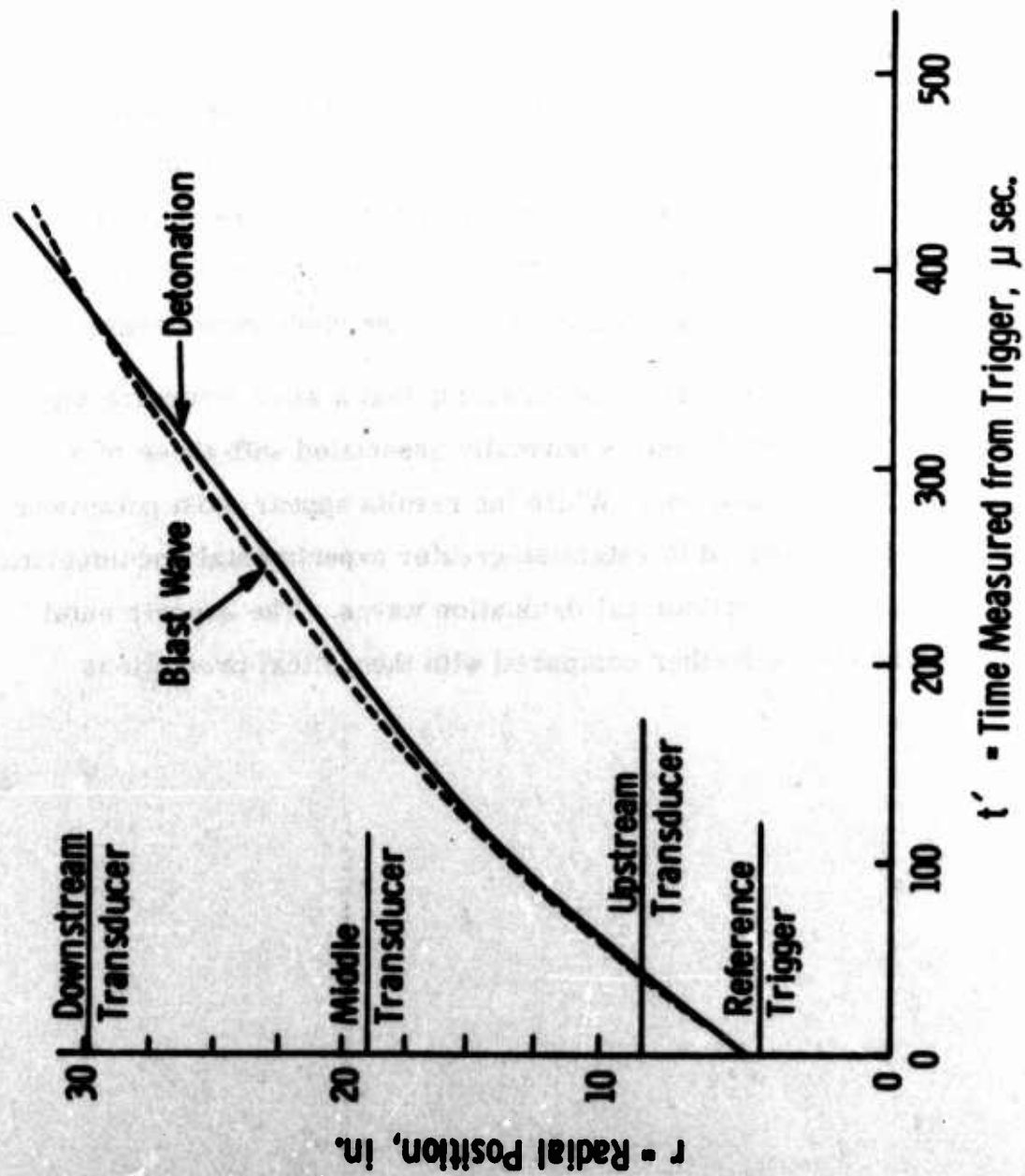


Figure 50. Comparison of Experimental Detonation and Blast Wave Data on an M Versus r Plot

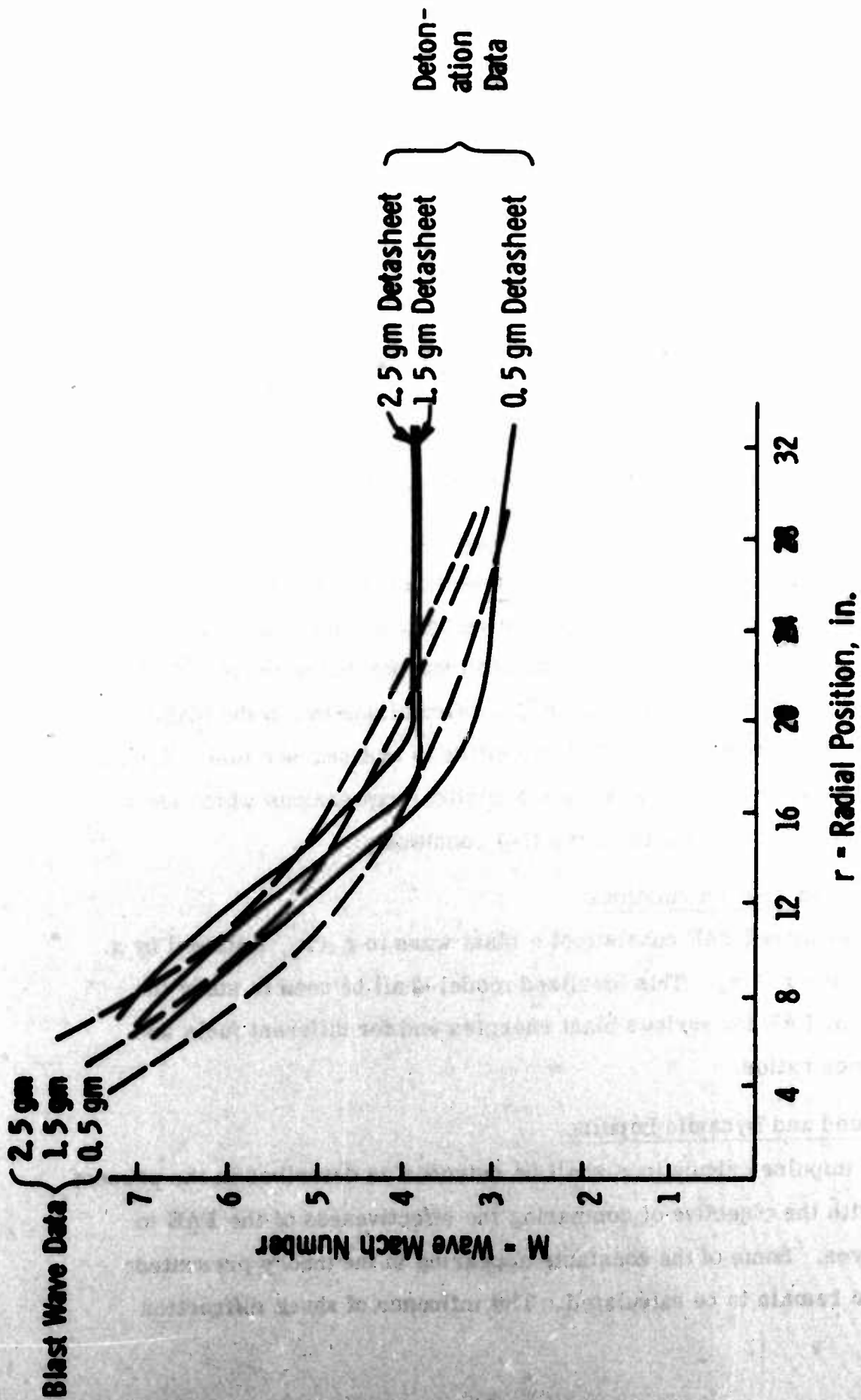


Figure 51. Comparison of Experimental and Blast Wave Data on an M Versus r Plot

SECTION IV

FUTURE PLANS

A. THEORETICAL CONSIDERATIONS

During the coming year it is planned to continue our theoretical analysis of FAE as outlined below.

1. C-J Waves with Cylindrical and Spherical Symmetry

Plans include the completion of the computer program for computing the propagation of cylindrical and spherical self-annular C-J waves. This program will be used in conjunction with the analysis described below.

2. The Influence of Droplets on Propagation

As indicated in this report, the presence of the fuel in the form of liquid drops influences the propagation velocity and the change in properties across a C-J wave. It is planned to incorporate the revised C-J conditions, both in the self similar C-J calculations and in the NASA program, for computation of C-J velocities in hydrocarbon fuel. Efforts will also be made to develop simple analytical expressions which show the influence of the droplets on the C-J conditions.

3. Idealized FAE Calculations

The idealized FAE consists of a blast wave to $r = r_*$, followed by a C-J wave for $r > r_*$. This idealized model shall be used to study the behavior of FAE for various blast energies and for different fuels and equivalence ratios.

4. Ground and Dynamic Impulse

The impulse calculations shall be extended as described in the present report with the objective of comparing the effectiveness of the FAE to blast waves. Some of the constants appearing in the theory presented here also remain to be calculated. The influence of shock diffraction

upon dynamic impulse will also be examined. A number of investigators have studied the interaction of shock waves with various objects, and it is planned to apply these results to the FAE.

5. The Effect of Side Relief

Side relief due to the finite size of the fuel cloud will have an important effect on the pressure and velocity distribution within a FAE. An attempt was made to develop simple models which will indicate the major effects of finite cloud size.

6. Initiation

The problem of blast initiation of FAE will be studied further. In particular, an attempt will be made to compare the expression for $(E_o)_{crit}$ presented in this report with experimental measurements. The effect of cloud geometry upon the initiation process will also be investigated.

7. Non Uniform Droplet Distribution

A similarity solution for self similar C-J waves with a non-uniform distribution of fuel-oxidizer ratio has already been presented. This and other similarity solutions will be examined to assess the main effects of the non-uniform distribution of droplets within the fuel cloud.

B. EXPERIMENTAL RESEARCH

The experimental facility and instrumentation appear to be working very satisfactorily. A fair amount of blast wave data (no fuel) has been obtained, and the results are quite reproducible with relatively small data scatter. Interpretation of the data in terms of theoretical cylindrical blast wave behavior presents some difficulty. Accordingly, it is planned to further reduce and analyze the present data. If the results indicate the need, some further runs would be made.

The experiments conducted in kerosene-air have been extremely encouraging. With sufficiently high initiation energies, the blast wave decays in strength until the critical radius where the detonation Mach number is realized. Evidently, beyond this point a steady state Chapman-Jouguet detonation is established. At lower energy levels there is evidence that the wave is not self-supporting and hence would gradually quench. This facet is of considerable importance to the initiation requirements, and it is planned on pursuing this point in some detail in order to establish a criterion for initiation. It is planned that more experimental data and analysis of the data will be obtained in the immediate future.

Upon achieving satisfactory results on the above, detonation experiments would then be conducted for a few different kerosene-air mixture ratios. The influence of equivalence ratio on initiation energy would be noted. After this, another fuel, with properties substantially different from those of kerosene, would be tested. Other work, such as various drop sizes, non-uniform fuel distribution, and high speed photography, would be incorporated upon achieving the desirable level of understanding of the foregoing. It is also planned to add a receiver section to the outlet of the test chamber in order to reduce the severe noise which accompanies the detonation tests.

REFERENCES

1. Nicholls, J. A. , Fry, R. S. , Glass, D. R. , Sichel, M. , Vander Schaaf, J. , Weener, E. F. , "Fundamental Aspects of Unconfined Explosions, " Six-Month Progress Report, Contract F08635-71-C-0083, Department of Air Force, Air Force Armament Laboratory (AFSC), Eglin AFB, Florida, 1971.
2. Chernyi, G. G. , Korobeinikov, V. P. , Levin, V. A. , and Medvedev, S. A. , "One-Dimensional Unsteady Motion of Combustible Gas Mixtures Associated with Detonation Waves, " *Astronautica Acta*, 15, 1970, p. 259.
3. Korobeinikov, V. P. , "The Problem of Point Explosion in a Detonating Gas, " *Astronautica Acta*, 14, 1969, p. 411.
4. Bishimov, E. , Korobeinikov, V. P. , and Levin, V. A. , "Strong Explosion in Combustible Gaseous Mixture, " *Astronautica Acta*, 15, 1970, p. 267.
5. Lee, J. H. , Knystautas, R. , and Bach, G. G. , "Theory of Explosions, " AFOSR Scientific Report 69-3090 TR, and McGill University, Department of Mechanical Engineering, Report MERL 69-10, 1969.
6. Sedov, L. I. , *Similarity and Dimensional Methods in Mechanics*, 4th ed. , Academic Press, New York, 1959.
7. Bach, G. G. , Knystautas, R. , Lee, J. H. , "Initiation Criteria for Diverging Gaseous Detonations, " Thirteenth Symposium (International) on Combustion, The Combustion Institute, 1971, p. 1097.
8. Collins, P. , *Proceedings of First FAE Conference*, Eglin AFB, Florida, 1971.
9. Oppenheim, A. K. , Lundstrom, E. A. , Kuhl, A. L. , Kamel, M. M. , "A Systematic Exposition of the Conservation Equations for Blast Waves, " *Transactions of the ASME*, presented as paper No. 71-WA/APM-1, Winter Annual Meeting, ASME, Nov. 28-Dec. 2, 1971.
10. Eisen, C. L. , Gross, R. A. , and Rivlin, T. J. , "Theoretical Calculations in Gaseous Detonation, " Air Force Office of Scientific Research, TN 58-326, 1968.
11. Taylor, G. I. , "Gas Dynamics of Combustion and Detonation, " Sec. G in *Fundamentals of Gas Dynamics*, Vol. III, Princeton Ser. in High Speed Aerodynamics and Jet Propulsion (H. Emmons, ed.), Princeton University Press, 1958.

12. Lewis, B. and Von Elbe, G., **Combustion, Flames and Explosions of Gases**, Academic Press, New York, 1961.
13. Williams, F. A., "Progress in Spray-Combustion Analysis," Eighth (International) Symposium on Combustion, The Williams and Wilkins Co., Baltimore, 1962.
14. Nicholls, J. A., Dabora, E. K., and Ragland, K. W., "A Study of Two-Phase Detonation as it Relates to Rocket Motor Combustion Instability," NASA CR 272, 1965.
15. Strehlow, R. A., "Gas Phase Detonations: Recent Developments," *Combustion and Flame*, 12, 1968.
16. Kauffman, C. W., "Shock Wave Ignition of Liquid Fuel Drops," Ph.D. Thesis, The University of Michigan, Ann Arbor, Michigan, 1971.
17. Kauffman, C. W., Nicholls, J. A., Olzmann, K. A., "The Interaction of an Incident Shock Wave with Liquid Fuel Drops," *Combustion Sci. and Tech.*, 3, 1971, p. 165.
18. Kauffman, C. W. and Nicholls, J. A., "Shock Wave Ignition of Liquid Fuel Drops," AIAA 8th Aerospace Sciences Meeting, New York, and AIAA J., 9, May 1971, p. 5.
19. Ragland, K. W., "The Propagation and Structure of Two-Phase Detonations," Ph.D. Thesis, The University of Michigan, Ann Arbor, Michigan, 1967.
20. Ragland, K. W., Dabora, E. K., and Nicholls, J. A., "Observed Structure of Spray Detonation," *The Physics of Fluids*, 11, 1968, p. 2377.
21. Dabora, E. K., Ragland, K. W., and Nicholls, J. A., "Drop Size Effects in Spray Detonations," Twelfth Symposium (International) on Combustion, The Combustion Institute, Pittsburgh, Pa., 1969, p. 19.
22. Bishimov, E., Korobeinikov, V. P., Levin, V. A., and Chernyi, G. G., "One-Dimensional Unsteady Motion of a Combustible Mixture with the Finite Rate of Chemical Reaction taken into Account," *Mekhan. Zhuk. Gasa*, 6, 1968, p. 7.
23. Sichel, M., "A Hydrodynamic Theory for the Propagation of Gaseous Detonations through Charges of Finite Width," AIAA J., 4, 1966, p. 264.
24. Dabora, E. K., Nicholls, J. A., and Morrison, R. B., "The Influence of the Compressible Boundary on the Propagation of Gaseous Detonations," Tenth Symposium (International) on Combustion, The Combustion Institute, 1965, p. 817.

25. Tsuge, S., Furukawa, H., Matsukawa, M., Nagakawa, T., "On the Dual Property and the Limit of Hydrogen-Oxygen Free Detonation Waves," *Astronautica Acta*, 15, 1970, p. 377.
26. Kiwan, A.R., "Gas Flow During and After the Deflagration of a Spherical Cloud of Fuel-Air Mixture," ERL Report No. 1511, (U. S. Army), 1970.
27. Pierce, T., "An Experimental and Theoretical Study of the Structure of Two-Phase Detonation in Sprays," Ph. D. Thesis, The University of Michigan, 1972.
28. Gordon, S. and McBride, B., "Computer Program for Calculation of Complex Chemical Equilibrium Compositions, Rocket Performance, Incident and Reflected Shocks, and Chapman-Jouguet Detonations," NASA SP 273, 1971.
29. Rayleigh, J.W.S., *Proceedings of London (1878) Mathematical Society*, 10, p. 4-18.
30. Nicholls, J.A., "Two-Phase Detonation Studies Related to Rocket Instability - 1969," NASA CR 72668, 1969, p. 5.
31. Dabora, E.K., Ragland, K.W., and Nicholls, J.A., "A Study of Heterogeneous Detonations," *Astronautica Acta*, 12, 1, 1966, p. 9-16.
32. Dabora, E.K., "Production of Monodisperse Sprays," *The Review of Scientific Instruments*, 28, 4, 1967, p. 502-506.
33. Pierce, T.H., "Production of Polydisperse Sprays," *The Review of Scientific Instruments*, 42, 11, 1971, p. 1648-49.
34. **Military Explosives**, Department of the Air Force Technical Order, TO 11A-1-34, 1967.
35. Rao, C.S.R., "Theoretical and Experimental Study of Film Detonations," Ph. D. Thesis, The University of Michigan, Ann Arbor, 1971.
36. Running, T.R., *Empirical Formulas*, John Wiley and Sons, Inc., 1917.

INITIAL DISTRIBUTION

SANDIA LAB ATTN R.P.STROMBERG	1
UNIV OF CONN ATTN PROF E.K. DABORA	1
USA BALLISTIC RSCH LAB ATTN DR FISHBURN	1
UNIV OF MICH ATTN PROF NICHOLLS	10
UNIV OF CINCINNATI ATTN PROF KAUFFMAN	1
BALLISTIC RSCH LAB ATTN DR KIWAN	1
UNIV OF CALIF ATTN PROF OPPENHEIM	1
IIT RESEARCH INST	1
PICATINNY ARS ATTN DR SLAGG	1
USA BALLISTICS RSCH LAB ATTN DR FREEDMAN	1
BALLISTICS RSCH LAB ATTN MR KINGERY	1
NAV WPNS CTR CODE 4563	1
AFSC (DLW)	2
AFSC (SDMM)	1
AFSC (IGFG)	1
AFSC (DPSL/TECH LIB)	1
HQ USAF (SAMI)	1
HQ USAF (XOONB)	1
HQ USAF (XOON)	2
HQ USAF (RDPA)	1
ASD (ENYS)	1
AUL (AUL-LSE-70-239)	1
DDC	2
HQ PACAF (IGY)	1
DL	1
DLOSL	2
DLIF	5

UNCLASSIFIED

Security Classification

DOCUMENT CONTROL DATA - R & D

(Security classification of title, body of abstract and indexing annotation must be entered when the overall report is classified)

1. ORIGINATING ACTIVITY (Corporate author)

Department of Aerospace Engineering
The University of Michigan
Ann Arbor, Michigan

2a. REPORT SECURITY CLASSIFICATION

UNCLASSIFIED

2b. GROUP

3. REPORT TITLE

FUNDAMENTAL ASPECTS OF UNCONFINED EXPLOSIONS.

4. DESCRIPTIVE NOTES (Type of report and inclusive dates)

Final Report, 28 Jan 1971 - 19 Jan 1972

5. AUTHOR (Last name, first initial, last name)

J. A. Nicholls, M. Sichel
R. S. Fry, J. Vander Schaaf
D. R. Glass

6. REPORT DATE

Mar 1972

7a. TOTAL NO. OF PAGES

7b. NO. OF REFS

154

36

8. CONTRACT OR GRANT NO.

F08635-71-C-0083 New

9. ORIGINATOR'S REPORT NUMBER(S)

AFATL-TR-72-49

10. PROJECT NO.

Task No. 07

11. OTHER REPORT NO(S) (Any other numbers which may be assigned to this report)

AFATL-TR-72-49

12. DISTRIBUTION STATEMENT

Distribution limited to U. S. Government agencies only. This report documents test and evaluation; distribution limitation applied March 1972. Other requests for this document must be referred to the Air Force Armament Laboratory (DLIF), Eglin Air Force Base, Florida 32542.

13. SUPPLEMENTARY NOTES

Available in DDC

14. SPONSORING MILITARY ACTIVITY

Air Force Armament Laboratory
Air Force Systems Command
Eglin Air Force Base, Florida 32542

15. ABSTRACT

The theoretical aspects of cylindrical strong blast waves and Chapman-Jouguet (C-J) detonations are treated in detail. A critical radius is discussed which divides the cloud into an inner blast wave zone and an outer detonation zone. Expressions for the evaluation of ground and dynamic impulse are presented, and the propagation of a C-J detonation through a cloud of fuel drops, the initiation problem, and deviations from the ideal cylindrical blast model are considered. A modified computer program for calculating detonation velocity of complex hydrocarbon fuels is discussed. The design and operation of an experimental facility to study the propagation of two-phase detonations in a cylindrical segment of a cloud is described. Experiments conducted with kerosene drops in air showed that at small radius the cylindrical wave decayed as a shock wave, but beyond a critical radius the wave becomes a constant velocity two-phase Chapman-Jouguet detonation. The experimentally determined critical radius agreed quite well with the theoretical predictions. The results lend encouragement to the prediction of threshold energy levels required for detonation initiation in various geometries.

DD FORM 1473

UNCLASSIFIED

Security Classification

402605 ✓

Pom

